Single-Molecule Spectroscopic Tools for Measuring Microsecond to Millisecond Dynamics of Calmodulin

by

E. Shane Price
B.A., William Jewell College,
Liberty, MO, 2002

Submitted to the Department of Chemistry and the Faculty of the Graduate School of the University of Kansas in partial fulfillment of the requirements for the degree of Doctor of Philosophy

_____
Carey K. Johnson (Committee Chair)

_____
Robert C. Dunn

_____
Heather Desaire

_____
Cindy L. Berrie

_____
Jennifer S. Laurence

Date defended: _____

The Dissertation Committee for E. Shane Price certifies
that this is the approved version of the following dissertation:

Single-Molecule Spectroscopic Tools for Measuring Microsecond to Millisecond Dynamics of Calmodulin

_____
Carey K. Johnson (Committee Chair)

_____

_____

_____

_____
(Committee Members)

Date approved: _____

Abstract

E. Shane Price, Ph.D.
Department of Chemistry, August 25, 2009
University of Kansas

Single-molecule spectroscopy has developed into a powerful tool for the study of biological systems. The ability to observe single protein changes has revealed a great deal of information about the heterogeneity of these systems. In this dissertation, single-molecule techniques have been used to investigate the effect of Ca^{2+} on millisecond and microsecond fluctuations of the protein calmodulin (CaM).

The first part of this dissertation discusses the development and testing of a home-built, two-channel, confocal microscope system used for fluorescence correlation spectroscopy (FCS) and scanning single-molecule measurements.

Secondly, the newly built system was tested by performing two-channel FCS measurements using a FRET-pair labeled synthetic polyproline peptide. Polyproline has been shown to approximate a "rigid-rod" and therefore was not expected to show any FRET fluctuations on the FCS timescale. The results from the polyproline correlations led to an investigation to develop expressions to describe the differences in the initial amplitudes of the correlations. These expressions were dependent on the presence of multiple FRET states in the solution and fits were demonstrated using both simulations and real data.

Next, the dynamics of several FRET-pair labeled mutants of CaM were measured using FCS techniques. The resulting correlations were globally fit to reveal inter-lobe dynamics on the 100 microsecond timescale that were diminished upon the

removal of Ca^{2+}. Intra-lobe dynamics of the N-terminus were also investigated demonstrating an increase in the dynamics in the apo state when compared to the Ca^{2+} bound state.

Finally, CaM was immobilized in unilamellar vesicles to probe millisecond dynamics of the CaM 34-110 mutant in the presence and absence of Ca^{2+}. Rates of interchange between conformational substates of CaM were measured demonstrating an increase in the rates of interchange between conformations in the presence of Ca^{2+}. This supports the view that when bound to Ca^{2+}, CaM is in a more dynamic state leading to its ability to bind a wide variety of targets.

Dedication

I praise you because I am fearfully and wonderfully made; your works are wonderful, I know that full well.

Psalm 139:14

Acknowledgments

I would first like to acknowledge my advisor, Dr. Carey Johnson. Your patience and guidance throughout this journey has meant the world to me. You have been a great example of how science and faith can co-exist without the need to compromise either.

I would like to thank my research colleagues that I have had the privilege of interacting with during my time at KU. Brian, you were my first teacher of all things single-molecule and I still applaud your optimism for all things. Thank you for the opportunity to work with you for a summer at the Stowers Institute. Mike, thanks for giving me the opportunity to jump right into research with you. Jay, I'm thankful for the chance to see you at work. Your absolute love of research is contagious and I hope you never lose that gift. Roshan, your ability to balance family and research is inspiring and I really enjoyed the exposure to Sri Lanka culture. Matt, well what can I say? A summer of programming (well maybe two months of programming and a month of figuring out why it wasn't working) that without you I might have never attempted. Thanks for the laughs, the movies that our wives wouldn't go to, introducing me to Stargate, and just the friendship.

For financial support, I would like to thank the National Institutes of Health biotechnology training grant as well as the National Science Foundation for grant support.

On a more personal side I would like to thank my families (both parental and spiritual) for their support. To my father, Roger I thank you for not only the early

memories of science in my childhood that started me on this journey but also for the spiritual support and guidance throughout my life. To my mother, Violet I thank you for always being there to listen and picking me up when I fall. To my mother and father-in-law, Paul and Jan, thank you for your constant encouragement and example and of course for raising such a caring and intelligent daughter.

To my other family members, including Aaron, Nathan, Shannon, Matt, Sarah, Drew: you have all played a special role in this process and I thank you for your prayers and support.

To my church family at Christ Community Church, and in particular, the worship team and my journey group: I am so thankful for the time I got to spend laughing, eating, worshiping, and praying with you. While I have been busy growing intellectually at KU you have greatly assisted me in the growing of my faith.

Finally, to my wife Kristin and daughter Kate: it is hard to know what to say. Kate, there is no better motivation to finish than to be able to spend time with you as you grow up. And Kristin, as I finish this dissertation on the 7th anniversary of our marriage I couldn't feel more blessed. Thank you for your encouragement and patience when the eternal pessimist in me came out. I look forward to what the future holds and to growing old with you by my side.

Table of Contents

List of Figures

List of Tables

1. Background and Relevance

1.1. Calmodulin

1.1.1. General Information

Calmodulin (CaM) is a small (16.7 kDa) protein found in all eukaryotic cells. CaM is a Ca^{2+} binding protein involved in the regulation of a wide variety of enzymes in the cell.[1-3] The signaling mechanism for CaM target binding and activation is a change in the endogenous Ca^{2+} concentration. CaM is composed of 148 amino acids and within vertebrates is highly conserved.[4] A fascinating aspect of CaM is its ability to bind over 100 known targets, such as phosphatases/kinases, receptors, channels, and pumps, which are involved with biological processes from muscle contraction to apoptosis.[5]

In this work chicken (*Gallus gallus*) CaM was used as the wild type protein for all mutations. The sequence of chicken CaM [6,7] is identical to that of bovine brain CaM [8,9] and that of human CaM [10], as determined through the use of the UniProtKB protein knowledgebase, demonstrating how well the sequence is conserved among vertebrates. CaM contains a high number of acidic residues leading to a theoretical pI of 4.09. CaM is composed of two globular domains connected by a seven-turn central helix linker.[11] Within each of the globular domains there are two helix-loop-helix domains, known as EF-hands. Each EF-hand is capable of binding a single Ca^{2+}. The two C-terminal EF-hands have been shown to bind Ca^{2+} with a three to five fold higher affinity than the N-terminal sites.[12] The range of

affinities of the binding sites for Ca^{2+} range from a K_d of 500 nM to 5 μM which is a concentration range similar to that found in most cells (10^{-7} M to 10^{-6} M).[12]

1.1.2. Conformations of CaM

Several structures for calmodulin have been published using both NMR and X-ray crystallographic methods for Ca^{2+}-free (also called apo) [13-16] and Ca^{2+}-saturated (four Ca^{2+} bound) forms.[11,17-21] One of the structures solved for apo-CaM is shown in Figure 1.1. In this structure the central linker helix is somewhat disordered producing a more globular form of CaM.[13] This is generally the inactive form of CaM with most of the hydrophobic residues protected from binding to targets. However, there are some hydrophobic patches slightly accessible allowing CaM to interact with some targets even at low levels of Ca^{2+}.[22] Research has shown that helix A (the first helix on the N-terminus) is relatively free in the apo state and is stabilized upon the binding of Ca^{2+}.[23,24]

The X-ray and NMR structures of CaM in the presence of Ca^{2+} vary in the final solved structure. The first structures indicated that CaM takes on a dumbbell configuration with the central helix in a rigid extended form as shown in Figure 1.2A.[11,19,25] Other work has shown evidence of a less extended central helix using NMR [26] and X-ray scattering.[27] More recently a structure of Ca^{2+} saturated CaM in a more compact structure was reported as shown in Figure 1.2B.[21] The diversity found in the crystal structures for CaM is a good indication that CaM is able to adopt several conformational substates.

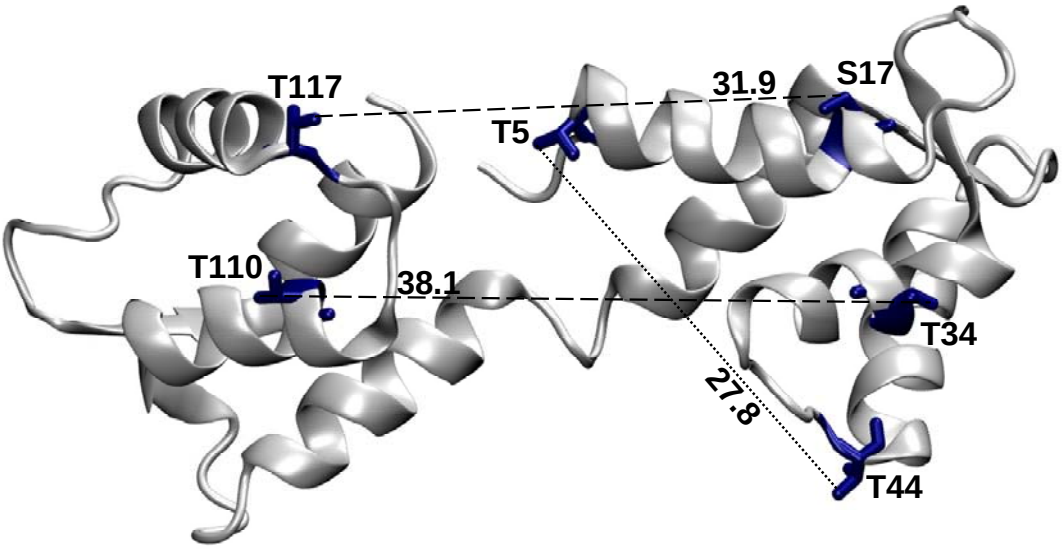

Figure 1.1: Average NMR structure for apo-CaM (pdb 1CFD). Residues of mutants used in this work and corresponding distances (in Å) between them are given.

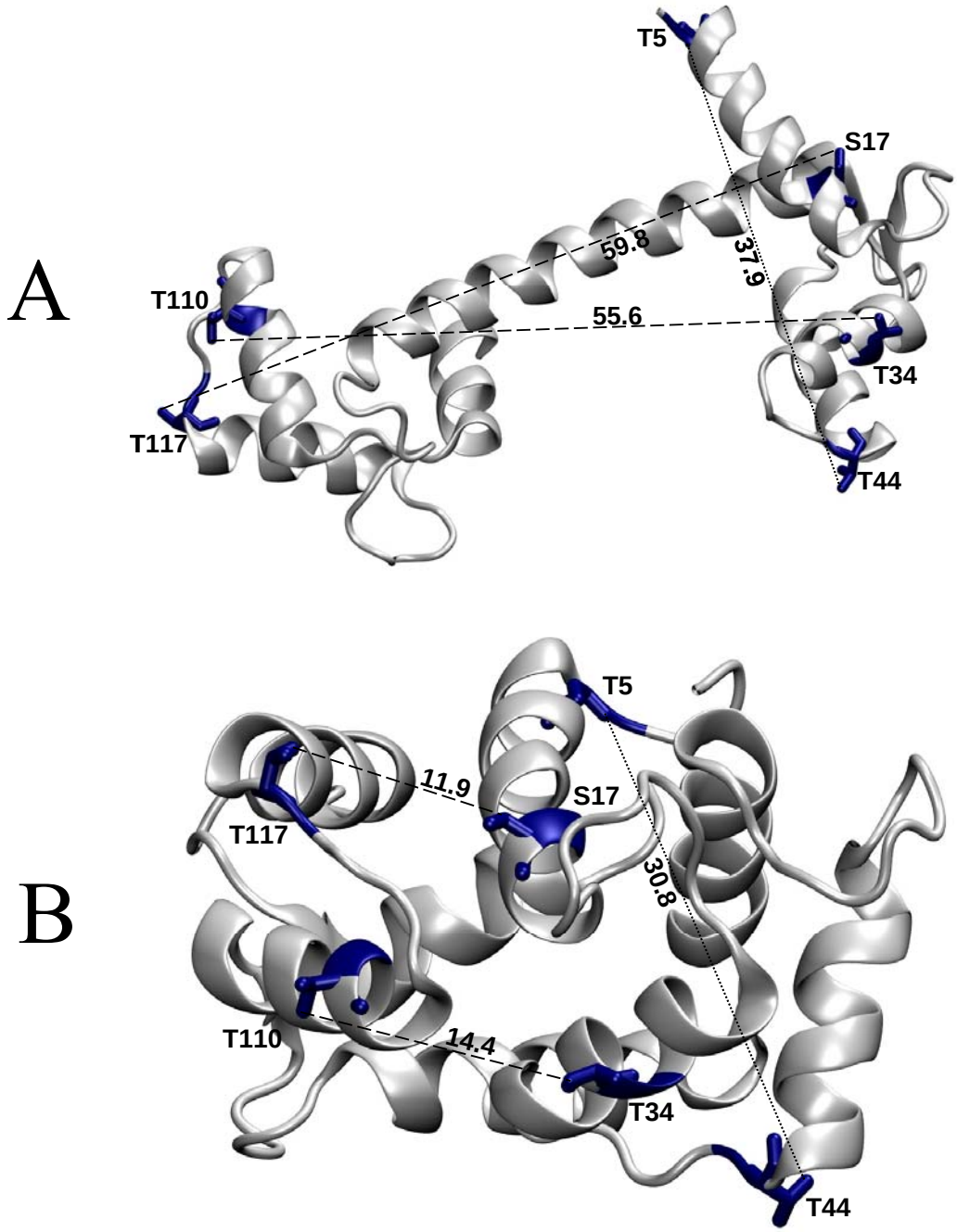

Figure 1.2: Average structures for Ca^{2+} CaM. Residues of mutants used in this work and corresponding distances (in Å) between them are given. (A) pdb 1CLL extended high Ca^{2+} structure. (B) pdb 1PRW compact high Ca^{2+} structure.

1.1.3. Conformational Fluctuations of CaM

As evidenced by the multiple conformations of CaM shown in the solved structures there must be one or more timescales under which the conformations change. Microsecond and millisecond fluctuations in the structure have been observed in CaM mutants that are composed of only the C-terminal domain.[28-32] It has been reported by Malmendal *et al*. that each domain of CaM, upon binding of Ca^{2+} changes from a compact to an open structure on the microsecond timescale.[28] The authors reported that the conformations exchange with a lifetime of 40 μs in the apo state. Other reports have measured a timescale of ~300 μs for apo-CaM.[33] A recent report using a microfluidic mixer to measure conformational changes of CaM upon Ca^{2+} binding identified two time constants of ~500 μs and ~20 ms, thought to be associated with conformational transitions of the C- and N-terminal domains.[34] These fluctuations in the structure of CaM upon Ca^{2+} binding are believed to be the primary switch for triggering the binding of CaM to its target proteins.[17,24,35]

1.2. Single Molecule Spectroscopy

Since its beginnings [36] single-molecule spectroscopy (SMS) has been viewed as a powerful resource for the investigation of biomolecules. SMS has seen a dramatic increase in penetration among many disciplines in recent years and has been the subject of multiple reviews.[37-42] The biological sciences have benefited greatly from the advances provided by SMS allowing researchers to address many previously unanswered questions. Single-molecule research affords the ability to

study one molecule at a time and avoid the ensemble averaging that conventional methods provide.

In general, single-molecule fluorescence experiments monitor a change in the fluorescence of a reporter dye molecule to measure some change in the dye's local environment. The fluorophores report the nano-environment around each dye that traditional bulk studies would average out over millions of molecules. In biomolecules a change in conformation from unfolding,[43] target binding,[44,45] or simply dynamics of the biomolecule [46] all have been monitored through SMS methods. While much of the SMS work has used synthetic dyes attached to the molecule of interest *in vitro,* there is great interest in performing single-molecule measurements *in vivo* where the biomolecule is in its natural environment. A major problem of the *in vivo* measurements is the introduction of the dye-labeled biomolecule into the cell without cell death or rejection of the biomolecule.

Besides the advantage of SMS reporting the distribution of the molecules rather than the average, it also provides a distinct advantage for kinetics measurements. In traditional bulk studies of kinetics all of the molecular processes need to be synchronized through some perturbation. Temperature jump [47] and microfluidic mixing [34] are a couple of examples of methods used to synchronize the molecules. In SMS there is no need for synchronization as each molecule is studied one at a time. This allows for studies ranging from measuring the triplet lifetime of a fluorophore [48,49] to monitoring single enzyme turnover events, revealing the true distribution of turnover rates.[50-52]

In the following sections two techniques that are applied to single-molecule measurements in this dissertation are introduced. Further details on the use of the techniques will be provided in the appropriate chapter(s).

1.3. Single-Molecule FRET

A very popular single-molecule method employs two fluorophores undergoing a transfer of energy. Förster (or fluorescence) resonance energy transfer (FRET) uses the non-radiative transfer of energy from a donor dye to an acceptor dye.[53,54] In order for the energy transfer to take place the emission spectrum from the donor dye must overlap with the absorption spectrum of the acceptor dye. The real power of FRET comes from the strong dependence of the transfer efficiency on the distance between the two dyes. Because of this strong dependence on distance with Ångstrom resolution FRET has been termed a "spectroscopic ruler".[55,56]

The rate of the energy transfer is given by equation 1.1 [57]:

$$k_{FRET} = \frac{1}{\tau_D}\left(\frac{R_0}{r}\right)^6 \tag{1.1}$$

where τ_D is the fluorescence lifetime of the donor in the absence of the acceptor and r is the distance between the two dyes. The R_0 term is unique for each donor-acceptor pair and is the distance at which the transfer efficiency is 50%. The value for R_0 can be calculated for each dye pair using equation 1.2:

$$R_0 = \left(\left[\frac{9000(\ln 10)\kappa^2 Q_D}{128\pi^5 N n^4}\right]J\right)^{1/6} \tag{1.2}$$

where Q_D is the quantum yield of the donor fluorophore in the absence of the acceptor, N is Avogadro's number, n is the refractive index of the medium (usually 1.4), κ^2 is the orientation of the donor and acceptor dipoles (to be discussed more below), and J is the overlap integral calculated using equation 1.3:

$$J = \int_0^\infty F_D(\lambda)\varepsilon_A(\lambda)\lambda^4 d\lambda \tag{1.3}$$

where $F_D(\lambda)$ is the emission of the donor dye normalized so that the integral of the emission spectra is equal to one and ε_A is the extinction coefficient of the acceptor fluorophore with units of $M^{-1}cm^{-1}$. Figure 1.3 shows an example of the overlap of a donor and acceptor dye pair.

The κ^2 value has been the focus of much debate and has been reviewed previously.[58,59] The value can be calculated from equation 1.4:

$$\kappa^2 = (\cos\alpha - 3\cos\beta\cos\gamma)^2 \tag{1.4}$$

where α is the angle between the donor emission dipole and the acceptor absorption dipole, β is the angle between the donor-acceptor connection line and the donor emission dipole, and γ is the angle between the donor-acceptor connection line and the acceptor absorption dipole. Figure 1.4 illustrates schematically how those angles are calculated. Using equation 1.4, κ^2 can range in value from zero to four depending on the orientation of the donor and acceptor dipoles. If the dyes are rotationally free on the timescale of the fluorescence lifetime then κ^2 averages to a value of 2/3, which is the value typically used in the calculation of R_0. The mobility of the dyes can be determined through time-resolved anisotropy measurements of the dyes, which

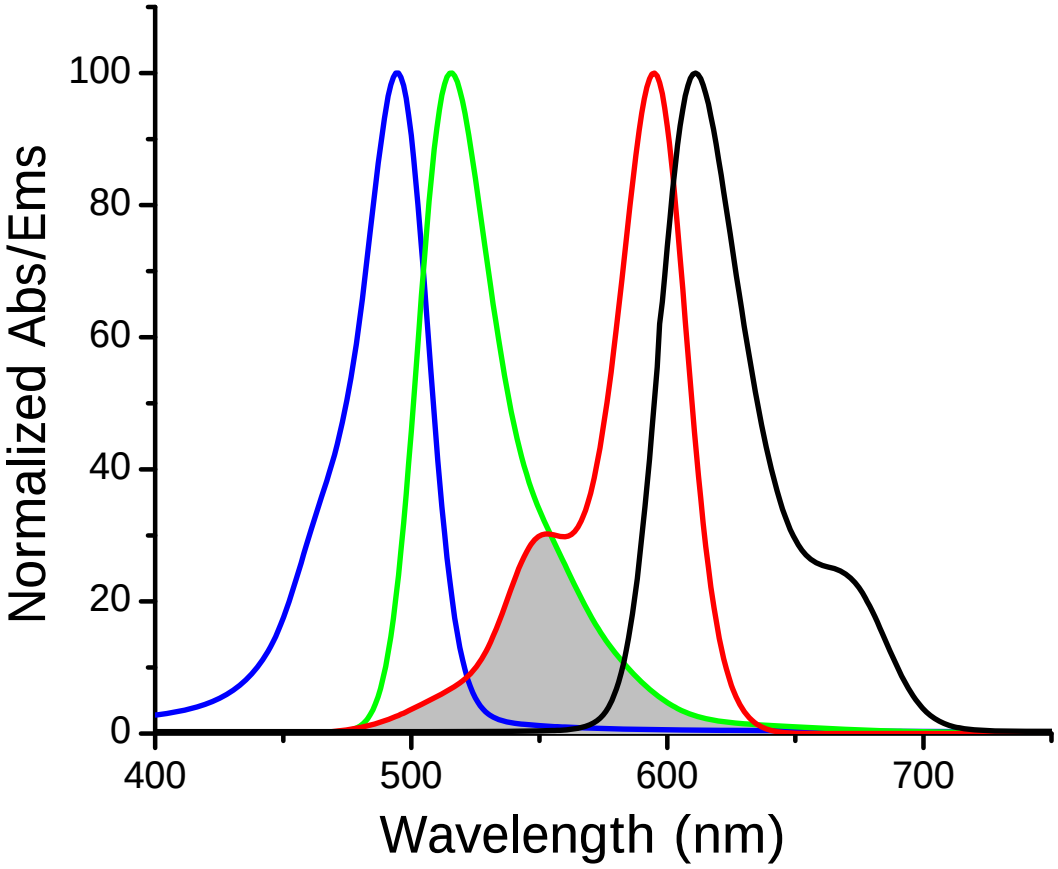

Figure 1.3: Example for the overlap of donor (Alexa Fluor 488) and acceptor (Texas Red) dyes. Absorbance for the donor and acceptor shown in blue and red, respectively. Emission for the donor and acceptor shown in green and black respectively. The overlap integral is calculated from the overlap of the donor emission with the acceptor absorbance (gray shading).

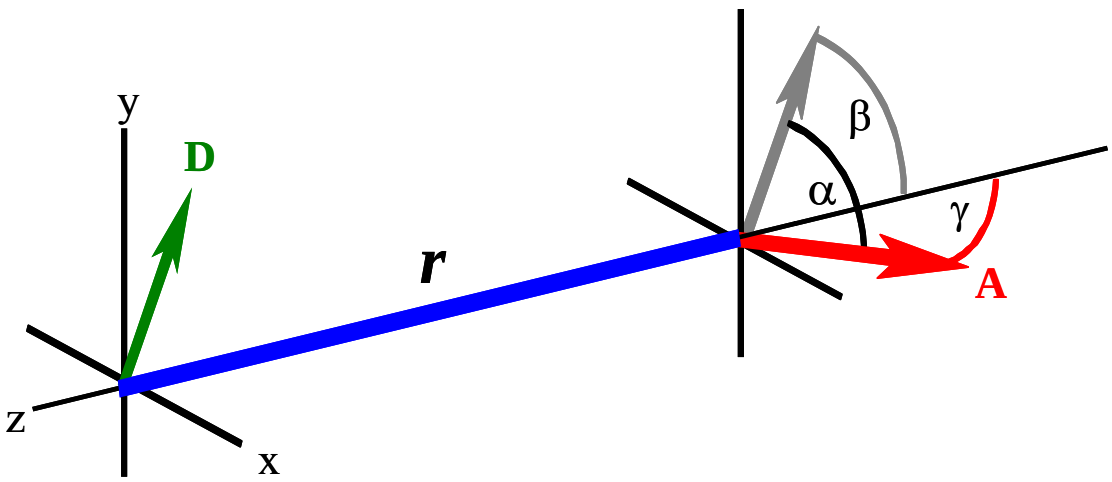

Figure 1.4: Representation of the angles used for calculating κ^2. The donor emission dipole is shown in green and the acceptor absorption dipole is shown in red. The gray arrow is the donor emission dipole moved to clarify the angles.

provides the rotational correlation times for the two fluorophores. In order to facilitate the calculation of the value for R_0 for various dye pairs a VBA script was written in an Excel workbook that contains absorbance and emission data for many of the currently used fluorescence dyes. The script allows any combination of donor and acceptor to be chosen from the dyes in the workbook to have the R_0 calculated.

In most experiments the efficiency of the transfer rather than the rate of transfer is the property that is measured. There are two commonly used techniques to measure the efficiency. The first uses fluorescence lifetimes to calculate the efficiency as given by equation 1.5:

$$E = 1 - \frac{\tau_{DA}}{\tau_D} \tag{1.5}$$

where τ_{DA} is the fluorescence lifetime of the donor in the presence of the acceptor molecule.

The other method employed for measuring the FRET efficiency is through sensitized emission of the donor and acceptor. It is calculated using equation 1.6:

$$E = \frac{I_A}{I_A + I_D} \tag{1.6}$$

where I_D and I_A are the fluorescence intensities of the donor and acceptor molecules, respectively. In actual lab situations it is highly unlikely that the two emissions can be used without some form of correction for differences in detection efficiency and cross-talk of the donor emission into the acceptor channel. To account for these equation 1.7 can be used in place of equation 1.6:

$$E = \frac{c(I_A - bI_D)}{c(I_A - bI_D) + I_D} \tag{1.7}$$

where the c term is a correction for difference in detection efficiency and the b term is to correct for cross-talk of the donor channel into the acceptor channel. These terms are system specific and can be determined using methods described previously in Allen.[60]

1.4. Fluorescence Correlation Spectroscopy

While many single-molecule measurements are performed on immobilized molecules with a high signal and low background, these experimental conditions are not always achievable in systems such as the high background found in live cells or when immobilization is difficult to achieve for the system under study. When confronted with this scenario, fluorescence correlation spectroscopy (FCS) can be utilized to overcome the molecular motion and poorer signals. FCS was first conceptually introduced in the 1970's [61-63] but it was not until FCS was paired with a confocal arrangement by Rigler *et al*. that the power of the technique was demonstrated.[64,65]

In FCS the correlation of the fluctuations of fluorescence due to various processes is used to study the processes of interest such as molecular diffusion, photophysical processes, or environmental changes leading to fluctuations in the fluorescence. Correlating the signal from the fluorescence for FCS works best if the fluctuations are large. This concept can be related by an analogy for diffusion in and

out of the observation volume. If a person is in a small room filled with of a hundred people, it is difficult for that individual to monitor when someone goes in or out of the room. However, if the person were in that same room with only five people it would be very easy to detect when someone enter or exits the room. Likewise, FCS works best when the observation volume is small and there are few molecules in the observation volume at a given time. This is best achieved through the use of a confocal microscope arrangement where the incoming light from a laser is strongly focused by a high numerical aperture objective (ideally >1) to form a diffraction-limited spot. To limit the detection volume, a pinhole is placed at the image plane in a confocal arrangement, which blocks out-of-focus light from reaching the detector.

The autocorrelation function is given in equation 1.8 [66]:

$$G(\tau) = \frac{\langle \delta I(t) \delta I(t+\tau) \rangle}{\langle I(t) \rangle^2} \tag{1.8}$$

where $\delta I(t) = I(t) - \langle I(t) \rangle$ with the brackets representing the average over all time and I(t) is the intensity of fluorescence at time t. The form that the function G(τ) takes depends on the spatial profile of the excitation source as well as the diffusive properties of the sample. When performing traditional one-photon excitation in a confocal arrangement the typical beam profile is considered a three-dimensional Gaussian defined by a radial beam waist of ω_0 and an axial waist (direction of beam propagation) of z_0. The axial waist is always larger than the radial waist resulting in a shape somewhat like a football.

Using a three-dimensional Gaussian for the beam profile, the G(τ) function can be solved analytically for molecules undergoing three dimensional diffusion to give equation 1.9 [67]:

$$G_{Diff}(\tau) = \left(\frac{1}{\langle N \rangle}\right) \cdot \left(\frac{1}{1+\left(\frac{\tau}{\tau_d}\right)}\right) \cdot \left(\frac{1}{1+\left(\frac{\tau}{p^2 \cdot \tau_d}\right)}\right)^{\frac{1}{2}} \tag{1.9}$$

where ⟨N⟩ is the average number of molecules in the focal volume, τ_d is the average transit time of the molecule through the observation volume, and $p = z_0/\omega_0$ also referred to as the axial-radial ratio. In some instances, the value of p is not well defined in the fit of the data and is measured independently then fixed in the analysis of the data.[68] The value of τ_d can be related to the diffusion coefficient (D) for the molecule through equation 1.10:

$$\tau_d = \frac{\omega_0^{\ 2}}{4D} \tag{1.10}$$

This relationship of τ_d to D can be used either to determine the size of the observation volume, if D is known, or the value for D if ω_0 has previously been measured.

The diffusion of molecules through the observation volume is not the only process that can lead to decay in the autocorrelation. One common process is intersystem crossing into the triplet state. While in the triplet state a molecule no longer undergoes the excitation/fluorescence emission pathway and is in a dark state. Because the triplet state is quantum mechanically forbidden it is a relatively long-lived state and shows up easily on the timescale of the autocorrelation. The

expression for the triplet decay can be written as a single exponential decay as given by equation 1.11 [48,49]:

$$G_{\text{Triplet}}(\tau) = \frac{(1-f) + \left(f \cdot e^{-\frac{\tau}{\tau_t}}\right)}{(1-f)} \tag{1.11}$$

where f is the fraction of molecules in the triplet state and τ_t is the triplet decay time. Because the triplet decay can occur on timescales of other fluorescence dynamics it is important to properly identify and fit the triplet contribution. The fraction of molecules in the triplet state is dependent on the incident laser power as evidenced in Figure 1.5. If the diffusion coefficient is unaltered by the triplet state then the following expression can be used to fit the diffusional and triplet component of an autocorrelation decay (Figure 1.6):

$$G(\tau) = \left(\frac{(1-f) + \left(f \cdot e^{-\frac{\tau}{\tau_t}}\right)}{(1-f)}\right) \cdot \left(\frac{1}{N_{xx}}\right) \cdot \left(\frac{1}{1+\left(\frac{\tau}{\tau_d}\right)}\right) \cdot \left(\frac{1}{1+\left(\frac{\tau}{p^2 \cdot \tau_d}\right)}\right)^{\frac{1}{2}} \tag{1.12}$$

Variations to the basic autocorrelation function will be presented as needed throughout this work.

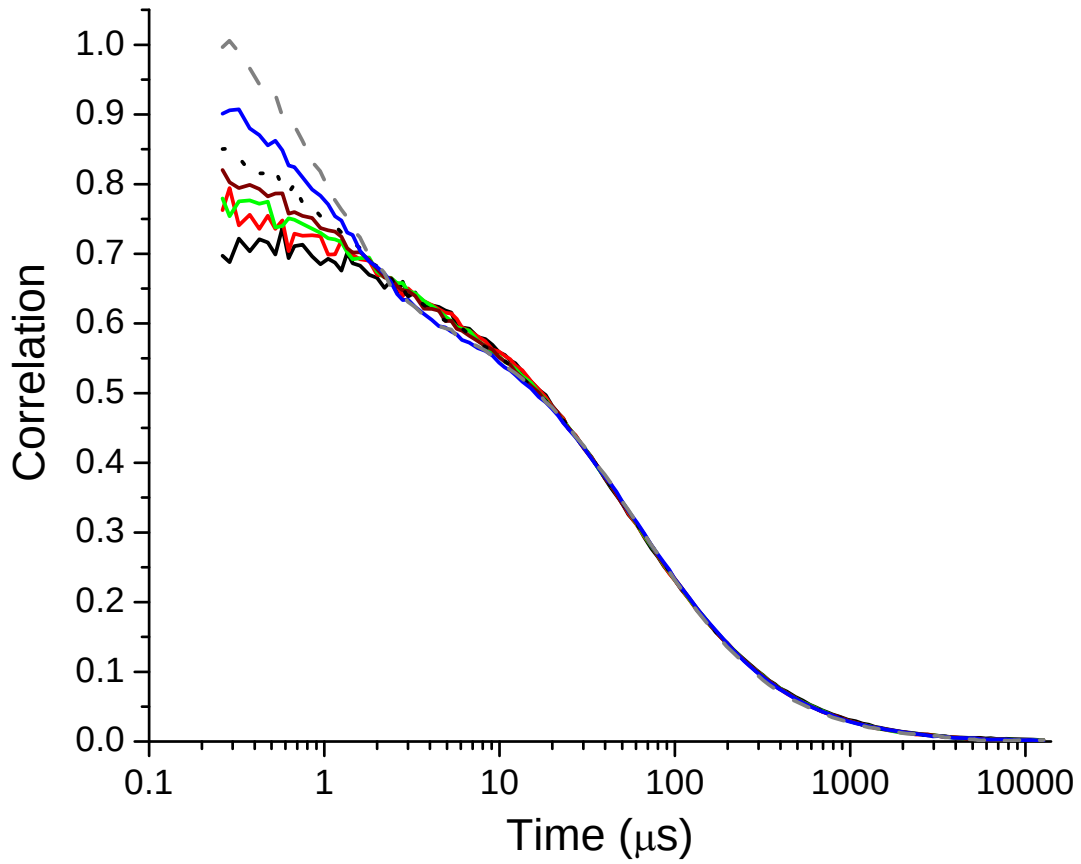

Figure 1.5: Effect of incident laser power on the fraction of the triplet state for 2.5 nM fluorescein. The correlation curves from lowest initial amplitude to highest were recorded at 5, 10, 15, 20 , 30, 50, and 75 μW of laser power, respectively.

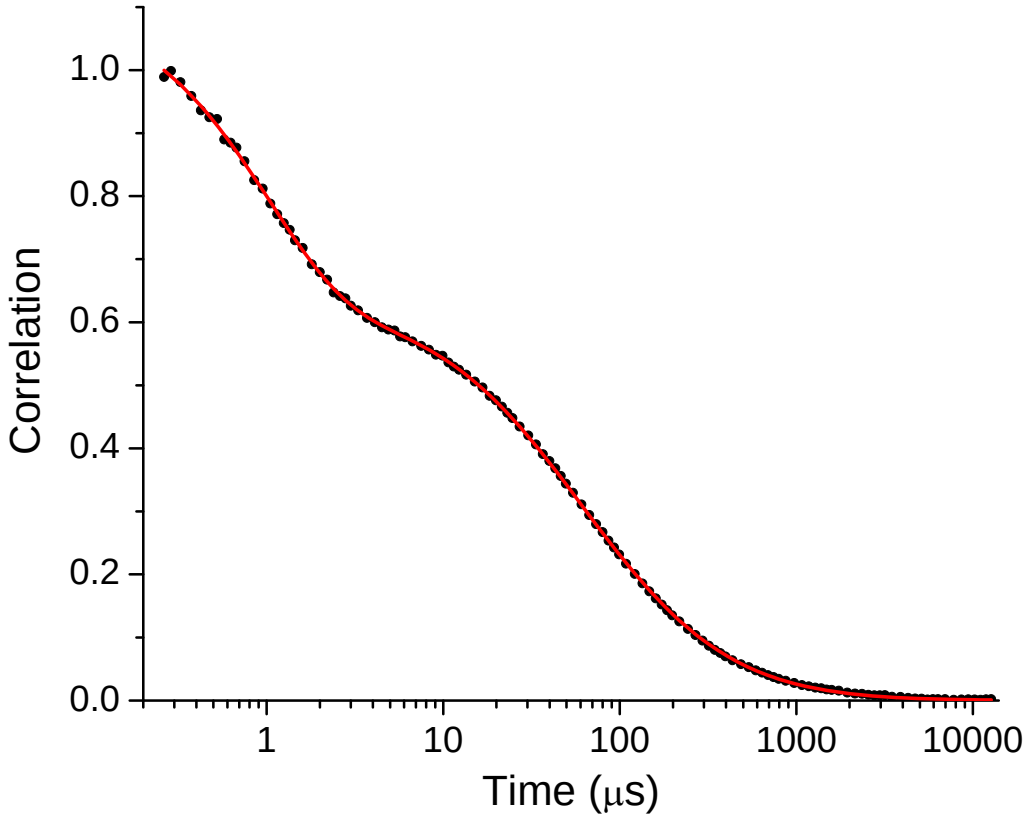

Figure 1.6: Example fit (red line) using equation 1.12 of 2.5 nM fluorescein data (black circles) taken at 75 μW of laser power. Triplet fraction = 0.429 ± 0.004, τ_t = 1.03 ± 0.03 μs, ⟨N⟩ = 1.579 ± 0.008, and τ_d = 62 ± 1 μs. Uncertainties calculated using the method of support plane analysis.

1.5. References

1. Klee, C. B., Crouch, T. H., and Richman, P. G., *Calmodulin*. Annu. Rev. Biochem., **1980**. 49: p. 489-515.

2. Means, A. R., and Dedman, J. R., *Calmodulin - an Intracellular Calcium Receptor*. Nature, **1980**. 285(5760): p. 73-77.

3. Means, A. R., Tash, J. S., and Chafouleas, J. G., *Physiological Implications of the Presence, Distribution, and Regulation of Calmodulin in Eukaryotic Cells*. Physiol. Rev., **1982**. 62(1): p. 1-39.

4. Wylie, D. C., and Vanaman, T. C., *Structure and Evolution of the Calmodulin Family of Calcium Regulatory Proteins*. in *Calmodulin*. Cohen, P., and Klee, C. B., editors. **1988**. Elsevier: New York. p. 1-15.

5. Best, R. B., and Hummer, G., *Biochemistry Unfolding the Secrets of Calmodulin*. Science, **2009**. 323(5914): p. 593-594.

6. Putkey, J. A., Kuei, F. T., Tanaka, T., Lagace, L., Stein, J. P., Lai, E. C., and Means, A. R., *Chicken Calmodulin Genes - a Species Comparison of cDNA Sequences and Isolation of a Genomic Clone*. J. Biol. Chem., **1983**. 258(19): p. 1864-1870.

7. Simmen, R. C. M., Tanaka, T., Tsui, K. F., Putkey, J. A., Scott, M. J., Lai, E. C., and Means, A. R., *The Structural Organization of the Chicken Calmodulin Gene*. J. Biol. Chem., **1985**. 260(2): p. 907-912.

8. Watterson, D. M., Iverson, D. B., and Vaneldik, L. J., *Spinach Calmodulin - Isolation, Characterization, and Comparison with Vertebrate Calmodulins*. Biochemistry, **1980**. 19(25): p. 5762-5768.

9. Watterson, D. M., Sharief, F., and Vanaman, T. C., *Complete Amino-Acid-Sequence of the Ca^{2+}-Dependent Modulator Protein (Calmodulin) of Bovine Brain*. J. Biol. Chem., **1980**. 255(3): p. 962-975.

10. Wawrzynczak, E. J., and Perham, R. N., *Isolation and Nucleotide-Sequence of a cDNA-Encoding Human Calmodulin*. Biochem. Int., **1984**. 9(2): p. 177-185.

11. Chattopadhyaya, R., Meador, W. E., Means, A. R., and Quiocho, F. A., *Calmodulin Structure Refined at 1.7 Å Resolution*. J. Mol. Biol., **1992**. 228(4): p. 1177-1192.

12. Chin, D., and Means, A. R., *Calmodulin: A Prototypical Calcium Sensor*. Trends Cell Biol., **2000**. 10(8): p. 322-328.

13. Kuboniwa, H., Tjandra, N., Grzesiek, S., Ren, H., Klee, C. B., and Bax, A., *Solution Structure of Calcium-Free Calmodulin*. Nat. Struct. Biol., **1995**. 2(9): p. 768-776.

14. Zhang, M., Tanaka, T., and Ikura, M., *Calcium-Induced Conformational Transition Revealed by the Solution Structure of Apo Calmodulin*. Nat. Struct. Biol., **1995**. 2(9): p. 758-767.

15. Schumacher, M. A., Crum, M., and Miller, M. C., *Crystal Structures of Apocalmodulin and an Apocalmodulin/Sk Potassium Channel Gating Domain Complex*. Structure, **2004**. 12(5): p. 849-860.

16. Chou, J. J., Li, S. P., and Bax, A., *Study of Conformational Rearrangement and Refinement of Structural Homology Models by the Use of Heteronuclear Dipolar Couplings*. J. Biomol. NMR, **2000**. 18(3): p. 217-227.

17. Wilson, M. A., and Brunger, A. T., *The 1.0 Å Crystal Structure of Calcium-Bound Calmodulin: An Analysis of Disorder and Implications for Functionally Relevant Plasticity*. J. Mol. Biol., **2000**. 301(5): p. 1237-1256.

18. Grabarek, Z., *Structure of a Trapped Intermediate of Calmodulin: Calcium Regulation of EF-hand Proteins from a New Perspective*. J. Mol. Biol., **2005**. 346(5): p. 1351-1366.

19. Babu, Y. S., Bugg, C. E., and Cook, W. J., *Structure of Calmodulin Refined at 2.2 Å Resolution*. J. Mol. Biol., **1988**. 204: p. 191-204.

20. Chou, J. J., Li, S., Klee, C. B., and Bax, A., *Solution Structure of Ca^{2+}-Calmodulin Reveals Flexible Hand-Like Properties of Its Domains*. Nat. Struct. Biol., **2001**. 8(11): p. 990-997.

21. Fallon, J. L., and Quiocho, F. A., *A Closed Compact Structure of Native Calcium-Calmodulin*. Structure, **2003**. 11(10): p. 1303-1307.

22. Swindells, M. B., and Ikura, M., *Pre-Formation of the Semi-Open Conformation by the Apo-Calmodulin C-Terminal Domain and Implications for Binding IQ-motifs*. Nat. Struct. Biol., **1996**. 3(6): p. 501-504.

23. Chen, B. W., Lowry, D. F., Mayer, M. U., and Squier, T. C., *Helix A Stabilization Precedes Amino-Terminal Lobe Activation Upon Calcium Binding to Calmodulin*. Biochemistry, **2008**. 47(35): p. 9220-9226.

24. Chen, B. W., Mayer, M. U., Markillie, L. M., Stenoien, D. L., and Squier, T. C., *Dynamic Motion of Helix A in the Amino-Terminal Domain of Calmodulin Is Stabilized Upon Calcium Activation*. Biochemistry, **2005**. 44(3): p. 905-914.

25. Babu, Y. S., Sack, J. S., Greenhough, T. J., Bugg, C. E., Means, A. R., and Cook, W. J., *Three-Dimensional Structure of Calmodulin*. Nature, **1985**. 315(6014): p. 37-40.

26. Barbato, G., Ikura, M., Kay, L. E., Pastor, R. W., and Bax, A., *Backbone Dynamics of Calmodulin Studied by 15N Relaxation Using Inverse Detected Two-Dimensional NMR Spectroscopy: The Central Helix Is Flexible*. Biochemistry, **1992**. 31(23): p. 5269-5278.

27. Wall, M. E., Clarage, J. B., and Phillips, G. N., *Motions of Calmodulin Characterized Using Both Bragg and Diffuse X-Ray Scattering*. Structure, **1997**. 5(12): p. 1599-1612.

28. Malmendal, A., Evenas, J., Forsen, S., and Akke, M., *Structural Dynamics in the C-Terminal Domain of Calmodulin at Low Calcium Levels*. J. Mol. Biol., **1999**. 293(4): p. 883-899.

29. Evenäs, J., Forsen, S., Malmendal, A., and Akke, M., *Backbone Dynamics and Energetics of a Calmodulin Domain Mutant Exchanging between Closed and Open Conformations*. J. Mol. Biol., **1999**. 289(3): p. 603-617.

30. Evenäs, J., Malmendal, A., Thulin, E., Carlstrom, G., and Forsen, S., *Ca^{2+} Binding and Conformational Changes in a Calmodulin Domain*. Biochemistry, **1998**. 37(39): p. 13744-13754.

31. Evenäs, J., Thulin, E., Malmendal, A., Forsen, S., and Carlstrom, G., *NMR Studies of the E140Q Mutant of the Carboxy-Terminal Domain of Calmodulin Reveal Global Conformational Exchange in the Ca^{2+}-Saturated State*. Biochemistry, **1997**. 36(12): p. 3448-3457.

32. Lundstroem, P., and Akke, M., *Quantitative Analysis of Conformational Exchange Contributions to 1H-15N Multiple-Quantum Relaxation Using Field-Dependent Measurements. Time Scale and Structural Characterization of Exchange in a Calmodulin C-Terminal Domain Mutant*. J. Am. Chem. Soc., **2004**. 126(3): p. 928-935.

33. Tjandra, N., Kuboniwa, H., Ren, H., and Bax, A., *Rotational Dynamics of Calcium-Free Calmodulin Studied by 15N-NMR Relaxation Measurements*. Eur. J. Biochem., **1995**. 230(3): p. 1014-1024.

34. Park, H. Y., Kim, S. A., Korlach, J., Rhoades, E., Kwok, L. W., Zipfel, W. R., Waxham, M. N., Webb, W. W., and Pollack, L., *Conformational Changes of Calmodulin Upon Ca^{2+} Binding Studied with a Microfluidic Mixer*. Proc. Natl. Acad. Sci. U.S.A., **2008**. 105(2): p. 542-547.

35. Yap, K. L., Ames, J. B., Swindells, M. B., and Ikura, M., *Diversity of Conformational States and Changes within the EF-hand Protein Superfamily*. Proteins, **1999**. 37(3): p. 499-507.

36. Moerner, W. E., and Kador, L., *Optical-Detection and Spectroscopy of Single Molecules in a Solid*. Phys. Rev. Lett., **1989**. 62(21): p. 2535-2538.

37. Nie, S. M., and Zare, R. N., *Optical Detection of Single Molecules*. Annu. Rev. Biophys. Biomol. Struct., **1997**. 26: p. 567-596.

38. Moerner, W. E., and Orrit, M., *Illuminating Single Molecules in Condensed Matter*. Science, **1999**. 283: p. 1670-1676.

39. Johnson, C. K., Osborn, K. D., Allen, M. W., and Slaughter, B. D., *Single-Molecule Fluorescence Spectroscopy: New Probes of Protein Function and Dynamics*. Physiology, **2005**. 20: p. 10-14.

40. Barkai, E., Jung, Y. J., and Silbey, R., *Theory of Single-Molecule Spectroscopy: Beyond the Ensemble Average*. Annu. Rev. Phys. Chem., **2004**. 55: p. 457-507.

41. Tinnefeld, P., and Sauer, M., *Branching out of Single-Molecule Fluorescence Spectroscopy: Challenges for Chemistry and Influence on Biology*. Angew. Chem. Int. Ed., **2005**. 44(18): p. 2642-2671.

42. Moerner, W. E., and Fromm, D. P., *Methods of Single-Molecule Fluorescence Spectroscopy and Microscopy*. Rev. Sci. Instrum., **2003**. 74(8): p. 3597-3619.

43. Rhoades, E., Gussakovsky, E., and Haran, G., *Watching Proteins Fold One Molecule at a Time*. Proc. Natl. Acad. Sci. U.S.A., **2003**. 100(6): p. 3197-3202.

44. Luo, G., Wang, M., Konigsberg, W. H., and Xie, X. S., *Single-Molecule and Ensemble Fluorescence Assays for a Functionally Important Conformational Change in T7 DNA Polymerase*. Proc. Natl. Acad. Sci. U.S.A., **2007**. 104(31): p. 12610-12615.

45. Slaughter, B. D., Urbauer, R. J. B., Urbauer, J. L., and Johnson, C. K., *Mechanism of Calmodulin Recognition of the Binding Domain of Isoform 1b*

of the Plasma Membrane Ca^{2+}-ATPase: Kinetic Pathway and Effects of Methionine Oxidation. Biochemistry, **2007**. 46(13): p. 4045-4054.

46. Chattopadhyay, K., Saffarian, S., Elson, E. L., and Frieden, C., *Measurement of Microsecond Dynamic Motion in the Intestinal Fatty Acid Binding Protein by Using Fluorescence Correlation Spectroscopy*. Proc. Natl. Acad. Sci. U.S.A., **2002**. 99(22): p. 14171-14176.

47. Rabl, C.-R., Martin, S. R., Neumann, E., and Bayley, P. M., *Temperature Jump Kinetic Study of the Stability of Apo-Calmodulin*. Biophys. Chem., **2002**. 101-102: p. 553-564.

48. Widengren, J., Mets, U., and Rigler, R., *Fluorescence Correlation Spectroscopy of Triplet States in Solution: A Theoretical and Experimental Study*. J. Phys. Chem., **1995**. 99(36): p. 13368-13379.

49. Widengren, J., Rigler, R., and Mets, U., *Triplet-State Monitoring by Fluorescence Correlation Spectroscopy*. J. Fluoresc., **1994**. 4(3): p. 255-258.

50. English, B. P., Min, W., van Oijen, A. M., Lee, K. T., Luo, G. B., Sun, H. Y., Cherayil, B. J., Kou, S. C., and Xie, X. S., *Ever-Fluctuating Single Enzyme Molecules: Michaelis-Menten Equation Revisited*. Nat. Chem. Biol., **2006**. 2(2): p. 87-94.

51. Lu, H. P., Xun, L., and Xie, X. S., *Probing Dynamics of Single Enzyme Molecules*. Biophys. J., **1997**. 74: p. A10.

52. Tan, W., and Yeung, E. S., *Monitoring the Reactions of Single Enzyme Molecules and Single Metal Ions*. Anal. Chem., **1997**. 69: p. 4242-4248.

53. Cheung, H. C., *Resonance Energy Transfer*. in *Topics in Fluorescence Spectroscopy*. Lakowicz, J. R., editor. **1991**. Plenum Press: New York. p. 128-176.

54. van der Meer, B. W., Coker, G., and Chen, S.-Y., *Resonance Energy Transfer: Theory and Data*. ed. **1994**. VCH: New York.

55. Stryer, L., and Haugland, R. P., *Energy Transfer: A Spectroscopic Ruler*. Proc. Natl. Acad. Sci. U.S.A., **1967**. 58(2): p. 719-726.

56. Stryer, L., *Fluorescence Energy-Transfer as a Spectroscopic Ruler*. Annu. Rev. Biochem., **1978**. 47: p. 819-846.

57. Lakowicz, J. R., *Principles of Fluorescence Spectroscopy*. 2nd ed. **1999**. Kluwer Academic/Plenum: New York.

58. van der Meer, B. W., *Kappa-Squared: From Nuisance to New Sense*. Rev. Mol. Biotechnol., **2002**. 82(3): p. 181-196.

59. VanBeek, D. B., Zwier, M. C., Shorb, J. M., and Krueger, B. P., *Fretting About FRET: Correlation between Kappa and R*. Biophys. J., **2007**. 92(12): p. 4168-4178.

60. Allen, M. W., *Analytical Chemistry at the Extremes: Ultrafast and Single Molecule Fluorescence Spectroscopic Investigations of Biological Systems* **2004** Department of Chemistry, University of Kansas, Lawrence. 230 pp.

61. Elson, E. L., and Magde, D., *Fluorescence Correlation Spectroscopy. I. Conceptual Basis and Theory*. Biopolymers, **1974**. 13(1): p. 1-27.

62. Magde, D., Elson, E., and Webb, W. W., *Thermodynamic Fluctuations in a Reacting System--Measurement by Fluorescence Correlation Spectroscopy*. Phys. Rev. Lett., **1972**. 29: p. 705-708.

63. Magde, D., Elson, E. L., and Webb, W. W., *Fluorescence Correlation Spectroscopy. II. Experimental Realization*. Biopolymers, **1974**. 13(1): p. 29-61.

64. Rigler, R., Mets, U., Widengren, J., and Kask, P., *Fluorescence Correlation Spectroscopy with High Count Rate and Low Background: Analysis of Translational Diffusion*. Eur. Biophys. J., **1993**. 22(3): p. 169-175.

65. Rigler, R., and Widengren, J., *Ultrasensitive Detection of Single Molecules by Fluorescence Correlation Spectroscopy*. Biosceince, **1990**. 3: p. 180-183.

66. Webb, W. W., *Applications of Fluorescence Correlation Spectroscopy*. Q Rev Biophys, **1976**. 9(1): p. 49-68.

67. Rigler, R., and Mets, U., *Diffusion of Single Molecules through a Gaussian Laser Beam*. Proc. SPIE, **1992**. 1921: p. 239-248.

68. Hess, S. T., and Webb, W. W., *Focal Volume Optics and Experimental Artifacts in Confocal Fluorescence Correlation Spectroscopy*. Biophys. J., **2002**. 83(4): p. 2300-2317.

2. Instrumentation and Sample Preparation

2.1. Single-Molecule Microscope System

The backbone for any single-molecule system is the microscope. The system used in this work was a Nikon TE2000 body, which is an inverted arrangement whereby the sample is placed on top of the objective and the beam is directed up into the sample. The microscope serves multiple purposes: it directs the excitation beam into the sample, holds the sample, collects the resulting emission and directs it to the detectors. The main components of a single-molecule microscope are the body, objective stage, sample stage, collection optics, and detector(s).

The body of the microscope needs to be rigid enough to hold all of the components in place to allow for consistent alignment of the system throughout the experiment. The objective stage has two main purposes: the first is to hold the objective in a fixed position during the experiment and the second is to move the objective in the z-dimension (along the light path) with a high level of precision. This maintains the same xy alignment to the detectors, regardless of the z position of the stage. The sample stage holds the sample in place above the objective and can be designed to move the sample over the objective for scanning applications.

The collection optics start with arguably the most crucial piece, the microscope objective. The objective is an infinity-focused, high magnification, high numerical aperture optic highly corrected for both spherical and chromatic aberrations. The high magnification and high numerical aperture produce a diffraction-limited spot with a focal volume of ~1 fL. The correction for spherical aberration improves

the shape and definition of the focal volume, while the chromatic aberration correction improves the position of the focus for different wavelengths to better overlap a wide range of wavelengths for multi-color experiments. The emission is collected by the same objective and exits through the back aperture of the objective where it is focused by the tube lens to the image plane.

Detectors for single-molecule systems need to be capable of detecting single photons with high quantum efficiency while maintaining a low background. For measurements performed in this work, the detectors required a low dead time (less than 100 ns) to avoid missing photons from molecules as the fluorescence emission is collected. The option that met all of the criteria was an avalanche photodiode (APD). The APD used in this work was the SPCM-AQR-14 module from Perkin Elmer (Quebec, Canada) that was capable of detecting single photons with a peak quantum efficiency of ~65% at 650 nm and a dead time of 50 ns.

2.1.1. Excitation

In order to achieve the diffraction limited spot needed for single-molecule detection, the excitation source must be a laser beam. This collimated beam of light provides the needed light properties to achieve optimal focusing by the objective.

The other property of the laser beam to be considered is the polarization of the beam. Most laser sources output linearly polarized light, which has a preferential interaction with fluorescent molecules whose excitation dipole is aligned with the beam polarization (Figure 2.1). To avoid a preferential excitation of molecules that

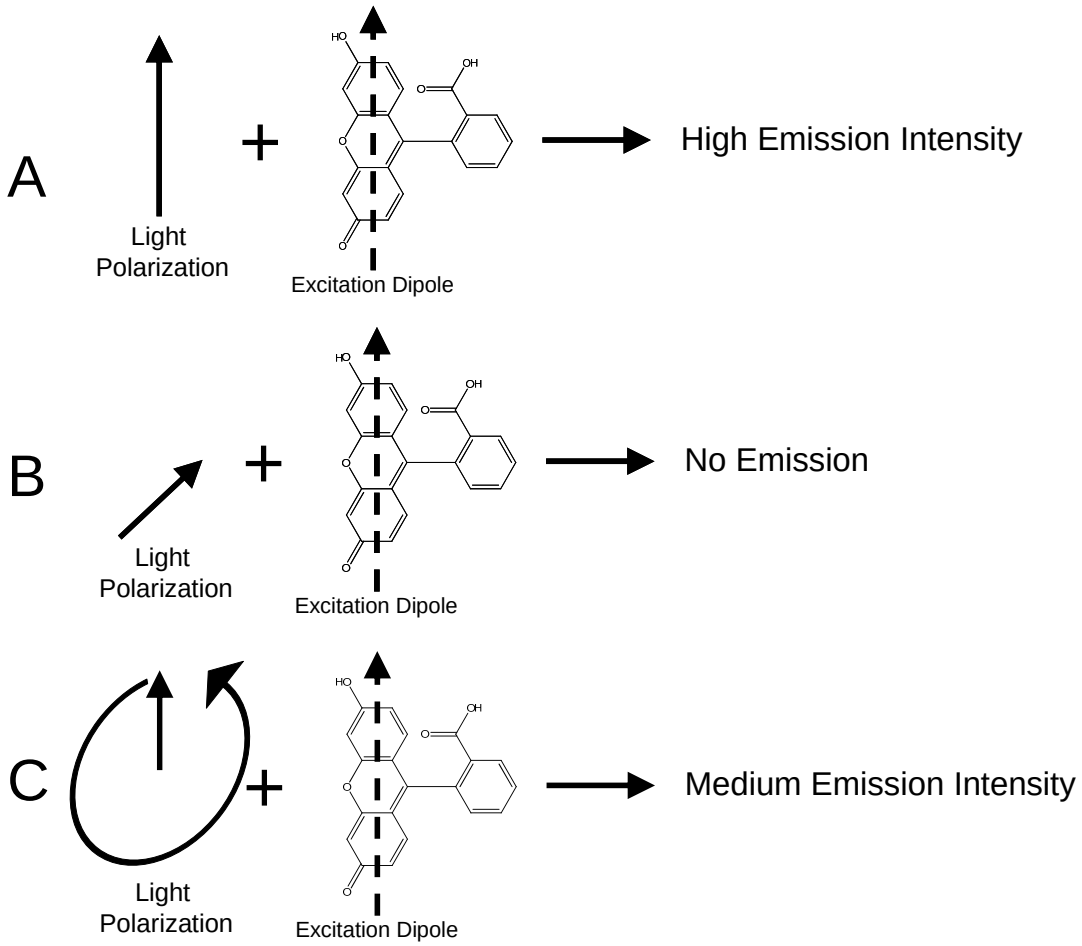

Figure 2.1: (A) Excitation dipole aligned with light polarization resulting in very high excitation efficiency. (B) Excitation dipole orthogonal to light polarization resulting in no excitation. (C) Excitation dipole with circularly polarized excitation resulting in lower excitation efficiency than A but the excitation is independent of the molecule's excitation dipole alignment with the light.

are aligned with the beam polarization, the linear polarization was changed to circular polarization using a quarter waveplate in the optical train. Circularly polarized light removes the preferential excitation of the fluorescent dye to remove orientational effects of the dye.

The excitation wavelength used for single-molecule measurements was the 488 nm line of an air-cooled argon ion laser (JDS Uniphase, Milpitas, CA). The beam was expanded using a Galilean beam expander to backfill the objective and was then circularly polarized.

2.1.2. Microscope Arrangement

The excitation beam entered through the back of the microscope where it was incident on the microscope dichroic (500DCXR Chroma, Rockingham, VT) which directed the beam upward to the back aperture of the objective (UPLSAPO 60XW Olympus, Center Valley, PA). The objective focused the beam to a diffraction limited spot where any fluorophores that were in the beam were excited. The fluorescence emission was then collected by the objective and passed through the microscope dichroic, where it was focused by the tube lens and directed out the side of the microscope body (Figure 2.2). Once outside of the microscope body, the fluorescence signal could be treated and detected in several ways as discussed in section 2.1.3

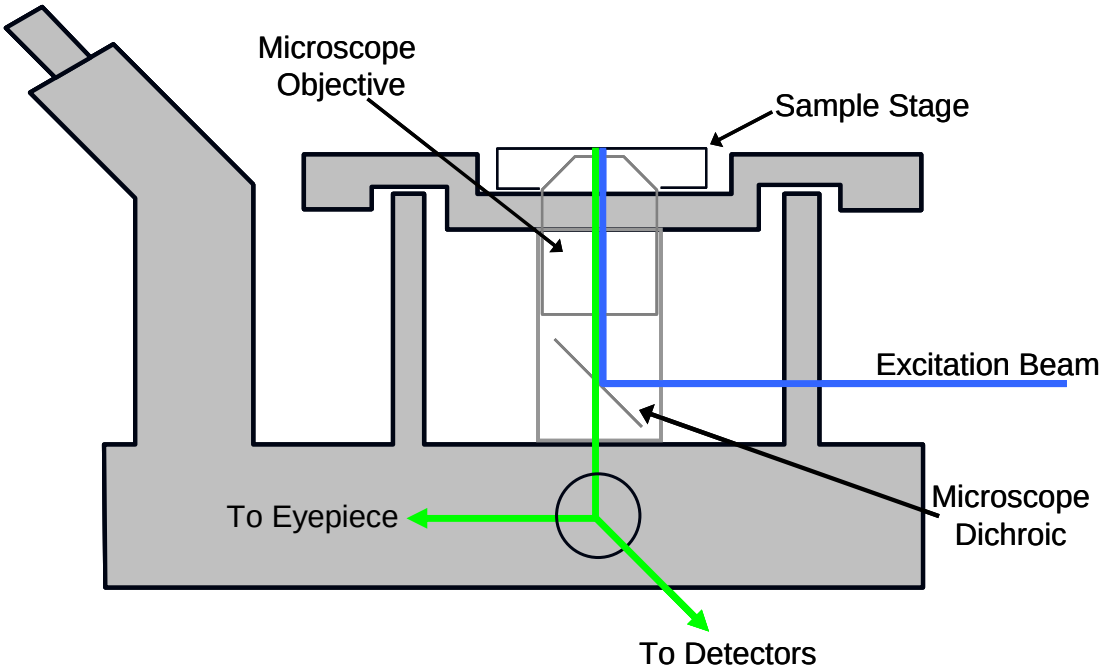

Figure 2.2: Side-view microscope diagram showing the beam paths.

2.1.3. Single-Channel vs. Two Channel Detection

There were two different detector arrangements used in this work. For simple FCS measurements, a single-channel arrangement was used. In this setup, a 75 μm pinhole (Thorlabs, Newton, NJ) was placed at the image plane of the microscope. When aligned, this rejects the out-of-focus light collected by the objective. After the pinhole, a bi-convex lens of focal length f was positioned 2f away from the pinhole with the APD (Perkin Elmer SPCM-AQR-14) positioned 2f away from the focusing lens (Figure 2.3A).

In the two detector arrangement, a beamsplitter (dichroic mirror, polarizer cube, etc.) was placed before the pinhole to split the emission beam. The reflected portion of the beam was directed parallel to the body of the microscope to an optical train identical to the single-channel arrangement (Figure 2.3B). This arrangement allows for independent adjustment of the two pinholes to correct for any aberrations introduced by the microscope that would lead to the two detection volumes not precisely overlapping in space. In this work the two detector arrangement was most often used with a dichroic as the beamsplitter to allow for the use of a green and red dye pair for FRET measurements.

The initial alignment of the two detector system was carried out by first mounting the pinhole for APD #2 on an xyz-translational stage in the approximate final position. The image plane of the microscope was known to be 3 cm from the side of the microscope body and was used for the initial z position. A dry coverslip was then placed on the microscope with the focus at the surface of the coverslip and

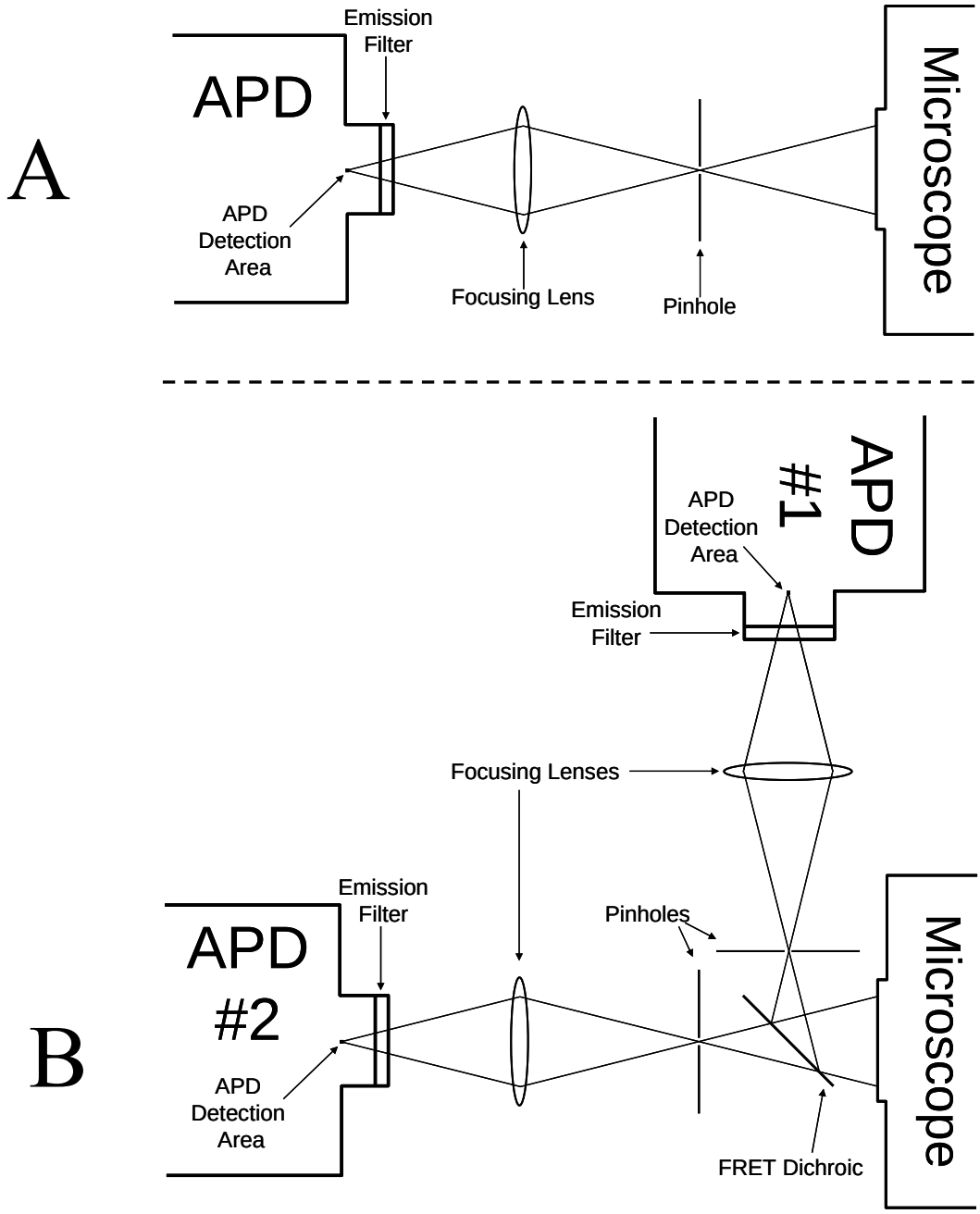

Figure 2.3 (A) Single channel FCS detection arrangement. (B) Two channel FCS detection arrangement.

the laser power was increased to full power (~20 mW). The scatter spot from the coverslip surface was intense enough to observe with the naked eye allowing rough positioning of the pinhole for APD #2 in the x, y, and z dimensions by looking for the position where a bright symmetrical round spot was seen on a white target. Once the correct alignment was found the position of the spot was marked on the white target and the focusing lens placed 2f from the pinhole and aligned until the spot was striking the same position to ensure that the beam was passing through the center of the lens. The dichroic mirror was then placed back into system and the procedure was repeated with the APD #1 pinhole and lens system.

Upon completion of the initial rough alignment, the APDs were positioned with an xyz-translational stage to the approximate focal point after the focusing lenses and the detection system was wrapped to avoid any stray light striking the APDs. To finish the fine alignment of APD #1 an appropriate dye sample was placed on the coverslip (100 nM Alexa Fluor 488 for example) and the laser power adjusted to ~50 μW. The APD was then moved to its maximum z position and the xy optimum position found. The z was then moved closer to the lens until the counts began to decrease and the xy position reoptimized. This was continued until the maximum count rate was achieved. The laser power was decreased when the count rates exceeded one million counts per second to avoid damaging the APD. After determining the optimum position of the APD, the final pinhole and APD positions were found through iteratively adjusting the pinhole position then the APD position. The procedure was repeated for APD #2 using a dye sample appropriate for the long-

pass range of the dichroic and the emission filter for the APD (Texas Red for example). Due to the low extinction coefficient of the red dye when excited by 488 nm, higher dye concentrations and higher laser powers were used to produce adequate emission signal for alignment. The optimum z-position for the pinhole in each channel would ideally be the point of maximum counts for each channel. Due to the focus properties for the image plane, there was not a well defined maximum in counts for the z-position. The final positioning of the z-axis for the pinholes is discussed in section 2.2.3.

The day to day alignment of the system involved the placing of a 20 μL drop of green aligning solution on the microscope with about 1 μW of 488 nm laser power. The green channel was then aligned by first careful adjustment of the pinhole in the xy direction. Then the red channel was aligned similarly using an appropriate red dye solution.

2.1.4. Choosing Filter Sets

When designing an optical experiment, filter choice can greatly affect the quality of the experiment. The best choice of filters depends on the dye(s) and excitation wavelengths used. When carrying out fluorescence measurements the Raman band of water (for a 488 nm laser line occuring from ~570 nm to 596 nm) also needs to be avoided.[1] Accounting for all these factors is crucial for an effective measurement. The dyes most commonly used in this work were Alexa Fluor 488 (Invitrogen, Carlsbad, CA), Texas Red (Invitrogen) and Atto 740 (Atto-Tec, Siegen,

Germany). Figure 2.4A shows the absorption and emission spectra for each of the previously mentioned dyes. The filters used for FRET measurements with Alexa Fluor 488 and Texas Red are shown in Figure 2.4B.

2.2. Data Acquisition Methods

Each registered photon from the APDs was outputted as a TTL pulse (2.2 V to 5 V positive pulse 50 ns long), which can be sent to a computer card for data collection. There are two main data collection methods utilized for single-molecule measurements and both have been implemented in this work. The core component for the data collection was a PCI computer card (PCI-6602, National Instruments, Austin, TX). The 6602 card contains an 80 MHz internal clock and eight software programmable counters. When connecting the detectors to the card, the impedance of the APD and the card must be considered. The APD outputs have 50 Ω impedance while the inputs on the 6602 card are high impedance. To connect the detectors to the 6602 card a National Instruments 68-pin connector/backshell kit was used, allowing connections to be made at the card interface with a 47 Ω resistor to aid in impedance matching and to cut down on extra reflections. Figure 2.5 shows the pin-out diagram for the 6602 card and the soldering connections made on the connector kit. The following sections will discuss the use of the counters for data collection and the advantages and disadvantages for each method.

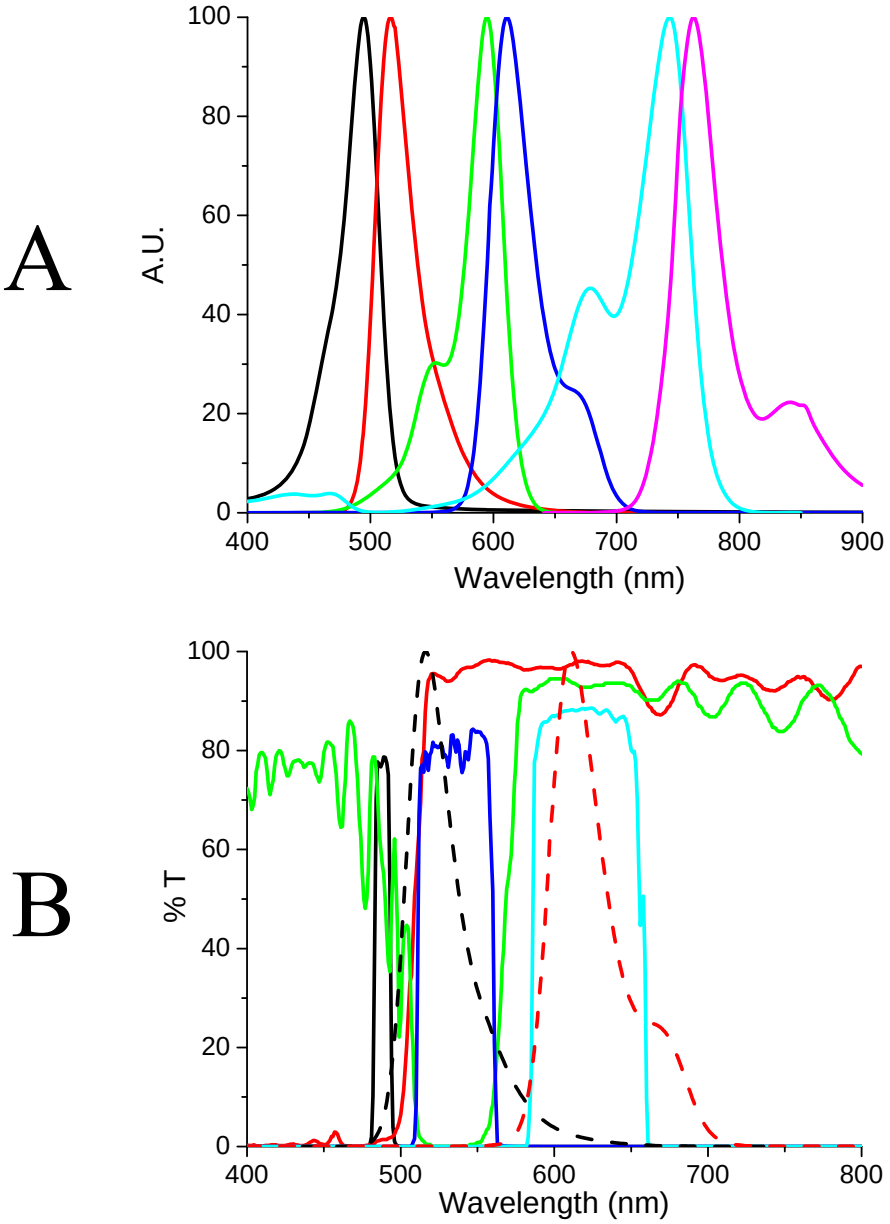

Figure 2.4: (A) Absorption and emission spectra for select dyes used in this work. From left to right Alexa Fluor 488 absorbance and emission, Texas Red absorbance and emission, and Atto 740 absorbance and emission. The curves have all been normalized to 100 for display purposes. (B) Example filter set used for FRET measurements, black line Z488/10x exciter, red line 500DCXR microscope dichroic, green line, 565DCLP FRET dichroic, blue line HQ535/50M green emission, and cyan line HQ620/75M red emission filter. The black and red dashed lines are respectively Alexa Fluor 488 and Texas Red emission spectra.

A

GND	PFI30/GATE2	PFI29/UP_DOWN2	GND	PFI26/GATE3	PFI25/UP_DOWN3	GND	PFI22/GATE4	PFI21/UP_DOWN4	GND	PFI18/GATE5	PFI17UP_DOWN5	Reserved	GND	PFI13/UP_DOWN6	PFI12/OUT6	PFI11/SOURCE7	PFI10/GATE7	GND	GND	PFI6/DIO6	PFI5/DIO5	GND	PFI2/DIO2	PFI1/DIO1	Reserved	GND	GND	PFI37/UP_DOWN0	GND	Reserved	Reserved	GND	Reserved
68	67	66	65	64	63	62	61	60	59	58	57	56	55	54	53	52	51	50	49	48	47	46	45	44	43	42	41	40	39	38	37	36	35
34	33	32	31	30	29	28	27	26	25	24	23	22	21	20	19	18	17	16	15	14	13	12	11	10	9	8	7	6	5	4	3	2	1
PFI31/SOURCE2	GND	PFI28/OUT2	PFI27/SOURCE3	GND	PFI24/OUT3	PFI23/SOURCE4	GND	PFI20/OUT4	PFI19/SOURCE5	GND	PFI16/OUT5	PFI15/SOURCE6	PFI14/GATE6	GND	Reserved	GND	PFI9/UP_DOWN7	PFI8/OUT7	PFI7/DIO7	GND	PFI4/DIO4	PFI3/DIO3	GND	PFI0/DIO0	PFI32/OUT1	PFI34/GATE1	PFI35/SOURCE1	PFI33/UP_DOWN1	PFI36/OUT0	Reserved	PFI38/GATE0	PFI39/SOURCE0	+5V

B

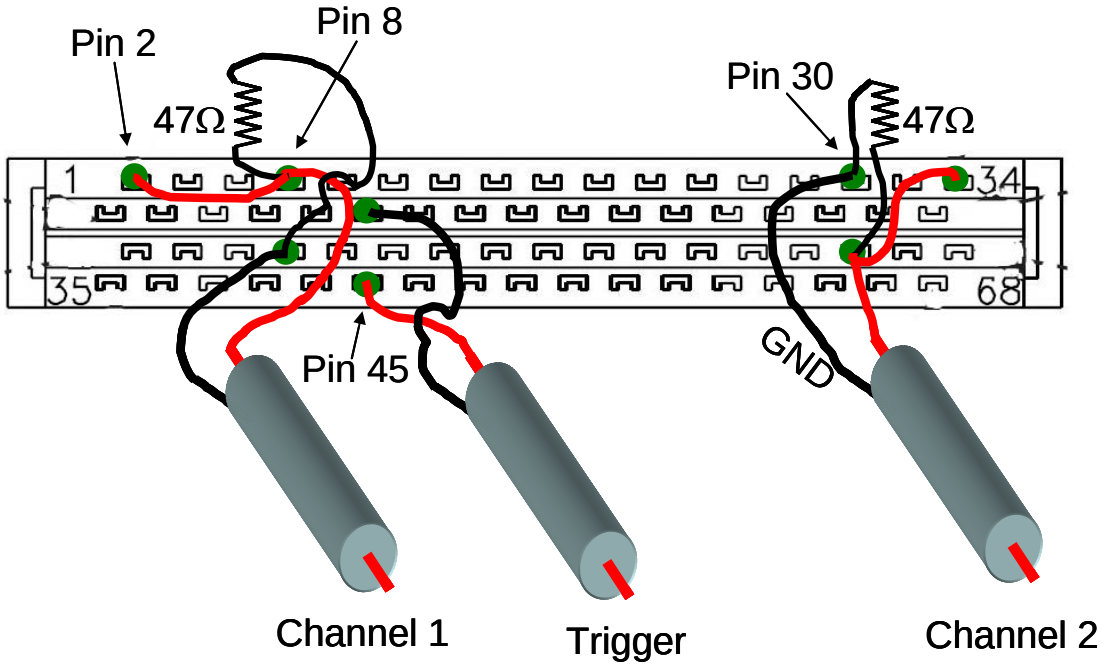

Figure 2.5: (A) Pinout diagram for PCI-6602 card. (B) Soldering diagram for 68 pin connector.

2.2.1. Time Mode

In time mode data collection, the photons are registered into preset time bins of known length. Each bin contains the number of photons that arrived during that time span. Due to the 6602 card's small FIFO (first-in-first-out) buffer of 2 samples for each counter along with a 16 sample DMA transfer buffer, this method is advantageous as the counter only outputs a number as fast as the time bin resolution (10 μs for example). Thus, the data can be easily read into the computer memory without any loss of data. This method however is not as effective when the time bins become very short for a couple of reasons. First, the FIFO buffer is filled much more rapidly and must be emptied to avoid overwriting the data. Secondly, the data files will become prohibitively large and waste computer space as the vast majority of the time bins have no counts in them.

2.2.1.1. Collection

Programming the 6602 card to operate in time mode was relatively straightforward. One of the counters was programmed as a pulse train generator that was able to generate pulses at any desired rate. Those pulses were then directed to the gate pin of another counter with a detector wired to the source pin of that counter. This arrangement allows the counter to be incremented for each TTL pulse from the APD and then read out when there is a gate pulse from the pulse train generator. In multi-channel measurements, everything stays synchronized by using the same pulse train generator connected to the gates for all of the counters.

2.2.1.2. Analysis

The analysis of time mode data was very straightforward for performing studies on immobilized molecules where the calculation of FRET efficiency or other intensity-dependent variable was desired. When FCS measurements were performed, the calculation of the correlation function was simple but time consuming. The correlation function was discussed previously in section 1.2.3. For data in time bins, the correlation function was calculated using equation 2.1:

$$G_{xy}(\tau) = \frac{\langle F_x(t) \cdot F_y(t+\tau) \rangle - \langle F_x(t) \rangle \cdot \langle F_y(t+\tau) \rangle}{\langle F_x(t) \rangle \cdot \langle F_y(t) \rangle} \tag{2.1}$$

Where x and y were the channel number for the correlation (x = y for an autocorrelation), $F_x(t)$ is the counts in bin at time t, and τ is the correlation lag time.

2.2.2. Photon Mode

In photon mode collection numbers are recorded only when a TTL pulse comes from the detector to the data acquisition card. There is an underlying time base that controls how fast the values increment between photons. On the 6602 card, the time base used is the 80 MHz internal clock. This results in a time resolution of 12.5 ns per increment. A major advantage to photon mode is that every number in the file represents a photon whose arrival time is known to within 12.5 ns (unlike time mode where it is only known how many photons arrived in a given time bin). All of

the zeroes that are usually present in time mode files could be reconstructed if required so there is no information loss when comparing photon mode to time mode.

2.2.2.1. Collection

In programming the 6602 card for photon mode collection, the detectors were wired to the gate pins for the counters and the internal clock was directed to the source pins. The counters were programmed to continually increment with each clock pulse and read out the current value when a TTL pulse arrived from the detector. Two important considerations when operating in this mode are first, the counters on the 6602 card are 32 bit counters. The largest integer that they can record is 2^{32}-1 which when operating at 80 MHz is the equivalent of about 53.7 seconds. When the counters have reached their limit they roll over to zero and start counting again. In typical FCS measurements data was often collected for 5 minutes or more, which resulted in the counter(s) rolling over multiple times. When it came time for analysis of the data this was taken into account.

The second major issue faced when setting the program up for two channel measurements was the synchronization of the data streams. If one of the channel counters started incrementing before the other channel then any correlation between the signals (cross-correlation) was lost due to the difference in starting times. In order to eliminate this issue a trigger event was inserted into the collection software that waited for an external signal before proceeding in the program. The trigger event occurred after both of the counters were programmed and armed by the software,

which reproducibly started the counters incrementing simultaneously. The external signal used for the system was a frequency generator set to output a TTL pulse at 10 Hz. It was found that having a trigger pulse every 100 ms was slow enough that the counters always started together but didn't introduce a large delay between pressing start in the software and the actual data collection.

The data collection program for photon mode was written using the Labview (National Instruments, Austin, TX) programming interface. Several issues with data collection had to be considered throughout the programming. The first major issue was the small size of the FIFO buffer on the 6602 cards, which led to the generation of a FIFO buffer overrun error when collecting data. When a burst of photon counts arrived at the card input, the FIFO buffer could not be emptied into the computer memory fast enough and one or more of the numbers was lost. This error would cause the data collection to halt frequently. By simply disabling that particular error the program ran without problem. The next major issue involved the evaluation of buffer over-runs causing errors in the data. This issue will be addressed later in this chapter in section 2.2.3.

2.2.2.2. Analysis

For conducting intensity-based FRET measurements from photon mode data, the data must first be converted to time mode to allow for the FRET efficiency to be calculated. Because the arrival times of all photons are known, it was not difficult to

convert to time mode with any resolution lower than what the photon-mode file was taken.

The calculation of the correlation function with photon mode data is a much faster algorithm and allows for much higher time resolution correlation curves to be calculated.[2-4] The correlation is a histogram of the time delays between photons as demonstrated in Figure 2.6 and explained below. The first step was to create an array of lag times that are the points in the final correlation decay. Because of the wide range of time scales sampled in the correlation, a quasi-logarithmic spacing was used to reduce the number of total points in the correlation. Two parameters were variable in the quasi-logarithmic spacing, the number of cascades and the number of points in each cascade. A cascade is a group of linearly spaced values whose spacing is 2^n, with n equaling the current cascade number. Once the lag time array was created, the correlation was generated by calculating the spacing between photons in the data stream and then incrementing the corresponding bin in the lag time array. When the time between photons fell between two values in the lag time array it was placed in the bin whose value was less than or equal to the time between the photons. This generated a histogram of time between all the photons in the data set whose lag times fell within the range determined by the number of cascades and number of points in each cascade.

The normalization of the histogram to generate the correlation curve involved accounting for the increasing bin width as the lag times became larger in the array

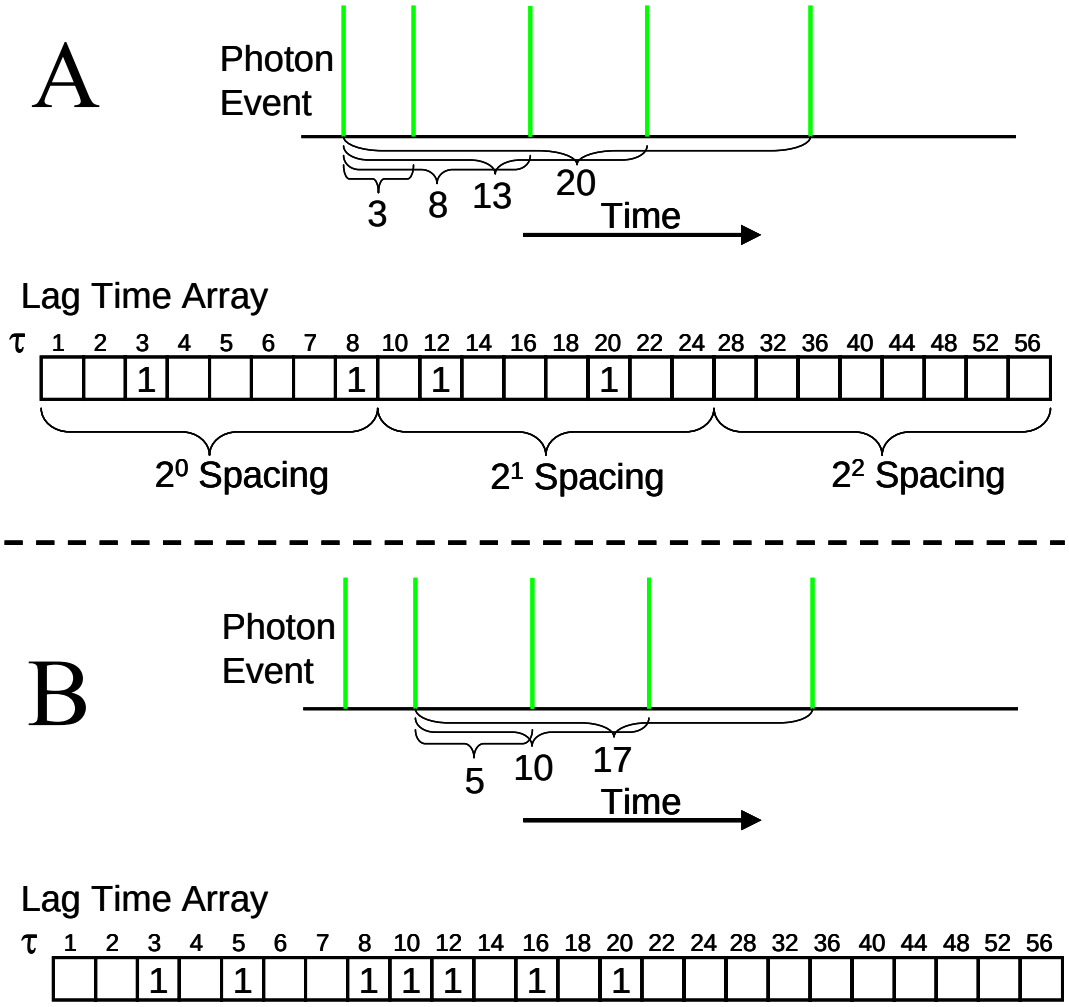

Figure 2.6: Demonstration of filling the lag time array with time between photon occurrences. (A) The times between the first photon and subsequent photons are determined. (B) After finishing with the first photon the times between the second photon and subsequent photons are determined.

and adjusting for the count rate of the measurement. For an autocorrelation the normalization is performed using equation 2.2:

$$G_{xy}(\tau) = \frac{\text{Histogram bin}(\tau)}{\left(\frac{\#\,\text{photons}}{\text{total file time}}\right)^2 (\text{total file time})(\text{lag time bin width})} - 1 \tag{2.2}$$

All photon mode correlation calculations were performed with software written and compiled in C++, which produced the fastest software for the calculations when compared to other programming languages.

2.2.2.3. Afterpulsing Correction

When a detector is hit by a photon and gives off a pulse, there is a probability that at some time later the detector will give off another pulse without the arrival of a photon. This extra pulse is known as afterpulsing. Every detector is different in the peak probability of afterpulsing and the shape of the probability. Typical afterpulse curves are shown in Figure 2.7. In FCS correlations, the afterpulsing from the detector adds extra decay components to the curve, complicating fitting of the data.

Traditionally, the method to remove the effects of afterpulsing is to introduce a 50% beam splitter into the emission path and use two detectors.[5] The afterpulsing between the two detectors is uncorrelated, so when the two signals are cross-correlated, the afterpulsing component is removed. Performing a two color measurement such as FRET would require four total detectors (two per color), which would lead to complicated alignments, and the beam splitter arrangement would generate loss of an already faint signal. Alternatively, it has been demonstrated by

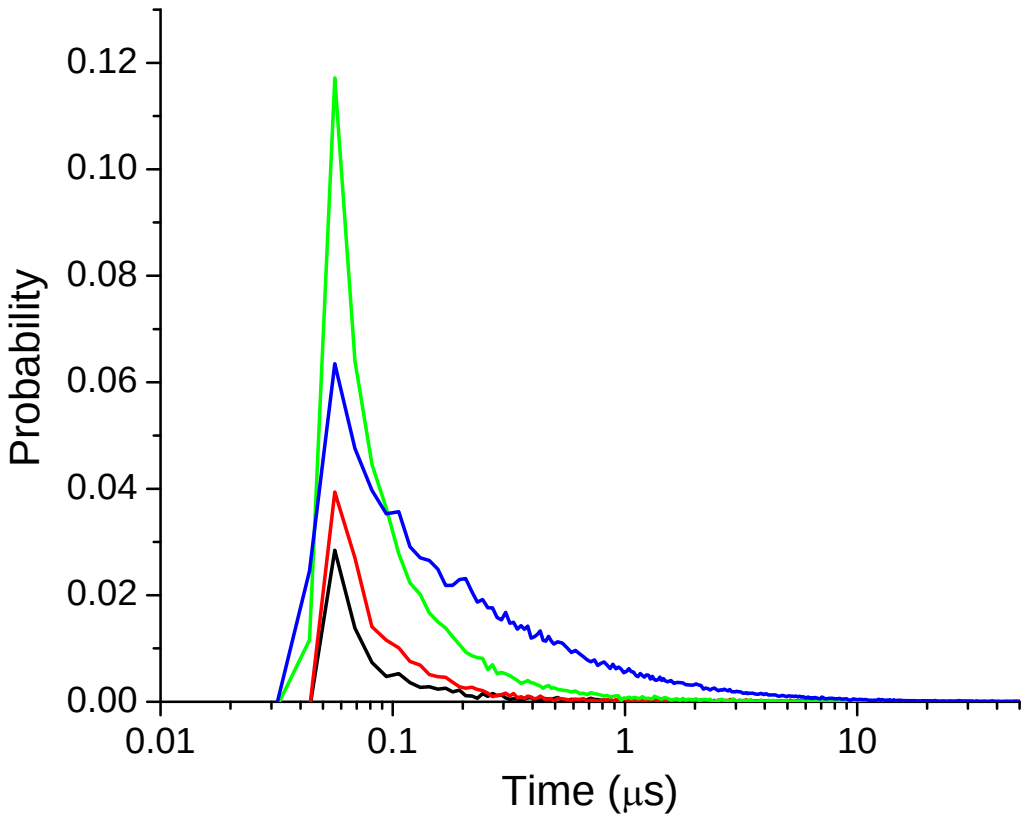

Figure 2.7: Afterpulsing probability curves for select Perkin Elmer SPCM AQR-14 APDs in the lab. Black line serial # 7647, red line serial # 7649, blue line serial # 5745-1, and green line serial # 12515. Note the different shapes and peak probabilities for the different serial numbers.

Zhao *et al*. [6] that afterpulsing for a single channel can be accounted for mathematically without the need for the beam splitter arrangement and two detectors. If the afterpulsing probability curve $\alpha(\tau)$ is assumed to be dependent on material defects, the room environment, and operating conditions (supply voltage and current) then $\alpha(\tau)$ will be largely independent of time. If we assume that the correlation curve decays much slower than $\alpha(\tau)$ then the correction can be applied using equation 2.3:

$$G_{xx}(\tau) = G'_{xx}(\tau) - \frac{\Delta t}{\langle i \rangle}\alpha(\tau) \tag{2.3}$$

where Δt is the dwell time (12.5 ns for our instrument) and $\langle i \rangle$ is the mean counts per dwell time, which can easily be calculated with equation 2.4:

$$\langle i \rangle = \frac{\#\ \text{photons}}{\text{total clock ticks}} \tag{2.4}$$

The shape of the afterpulsing curve $\alpha(\tau)$ was measured before the experiment using an uncorrelated light source. This was accomplished by focusing the laser source into a drop of ultrapure water on a coverslip and adjusting the power to get a count rate of approximately 1 kHz. After about 1 million photons were collected the file was then correlated and converted to a probability distribution by multiplying the correlation by $\langle i \rangle/\Delta t$. The probability distribution was then fit starting at the peak using a multi-exponential decay sufficient to describe the shape of the afterpulsing. The parameters for the multi-exponential fit were then fed into the correlation software and used in the function $\alpha(\tau)$ at the end of the correlation calculation. The fitting and outputting

of parameters was performed using a piece of LabVIEW software written in house. An example corrected curve is shown in Figure 2.8.

2.2.3. System Verification and Daily Checks

To ensure quality data for each measurement, careful steps were taken to check the integrity of the system. The first system check involved comparison of data collection styles (time mode vs. photon mode) to verify that the FIFO errors encountered in photon mode did not generate systematic errors in the calculated correlations. As shown in Figure 2.9, the two methods were very similar with no major differences in the correlation curves. This check also reinforced the advantages of photon mode when comparing the size of the data files, time resolution, and computation time required. For example, a single photon-mode file of 20 nM fluorescein was collected at a count rate of 70 kHz for about 75 seconds (5.2 million photons) at 12.5 ns resolution resulting in a file size of about 23 MB. To achieve similar results using the time-mode program, five data sets were taken at 5 μs resolution (highest time resolution possible) with about three million time bins in each file totaling about 90 MB of hard drive space for all 5 files. The calculation times for the two methods were about 25 minutes for the time-mode correlations and approximately 5 minutes for the photon-mode correlations. Finally, the difference in the time span of the correlations for each method is 5 μs to 25,000 μs for time mode whereas the photon mode correlations span 0.0125 μs to 25395 μs, allowing a much wider timescale to be sampled.

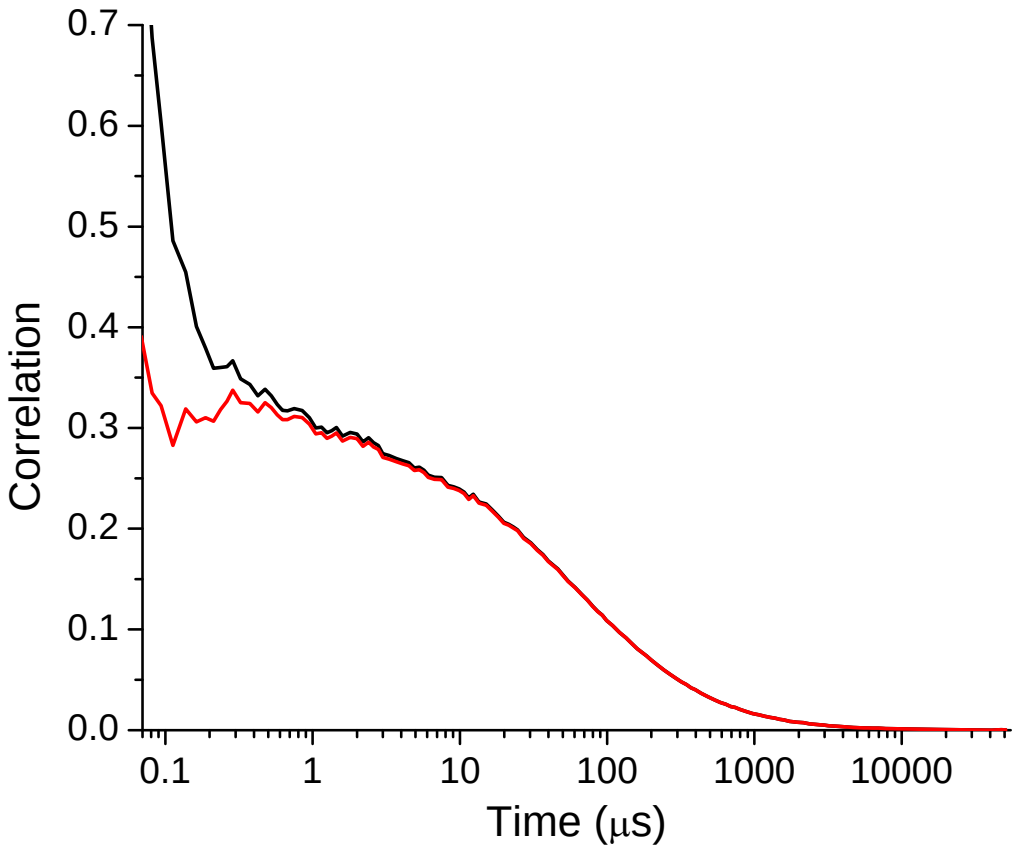

Figure 2.8: Corrected (red line) and uncorrected (black line) autocorrelation curves for fluorescein.

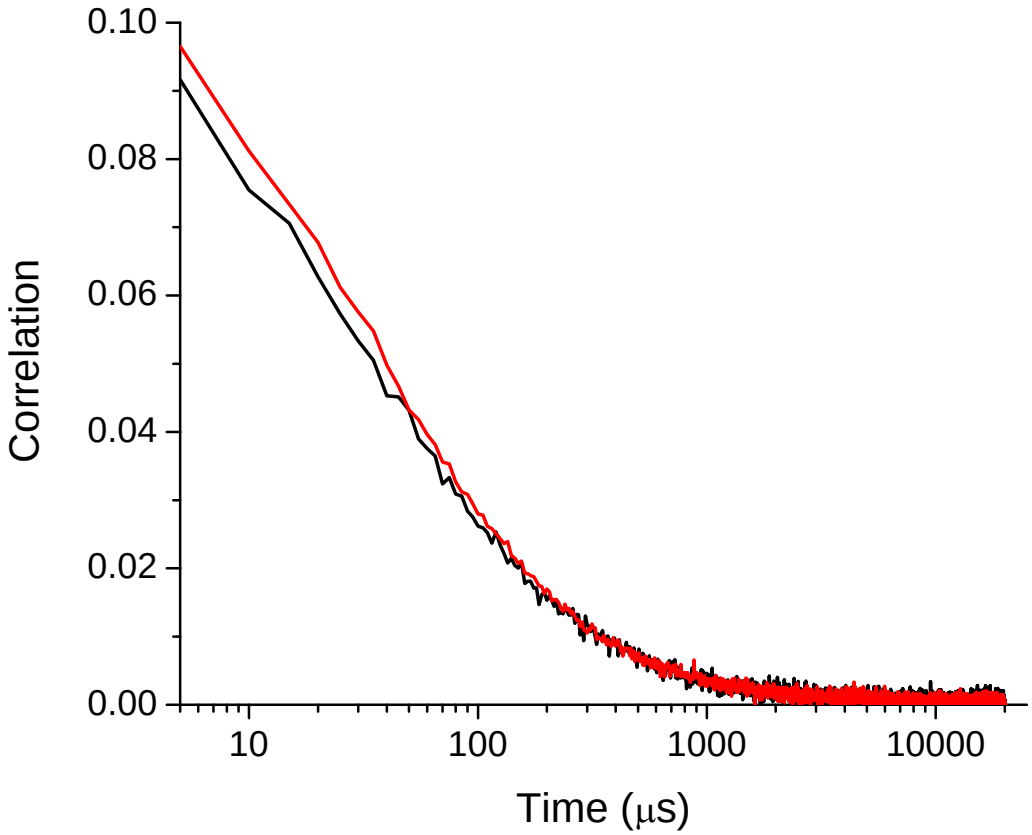

Figure 2.9: Comparison of photon mode (black line) to time mode (red line). The photon mode data was converted to time mode for a direct comparison of the correlations. The sample used was a 20 nM fluorescein solution with 55 μW laser power.

Another check monitored the system for a linear relationship between concentration and the average number of molecules obtained from the fit of the correlation using equation 1.12. The laser power was held constant at 40 μW throughout the measurements, and the sample was fluorescein with concentrations ranging from 1 nM to 20 nM. An example correlation and its corresponding fit to equation 1.12 is shown in Figure 2.10A with the linear regression fit of concentration vs. average number of molecules in the observation volume shown in Figure 2.10B.

The final check that was performed (and performed at the beginning of each day of data collection) verified that the two channels detected the same spatial probe volume and that the synchronization of the channels was operating properly. This involved the use of a sample of fluorescein and the collection of data in both green and red channels. The signal in the red channel arises from the red tail bleedthrough of the dye emission (about 11%) through the acceptor filter set. If the observation volumes are overlapped then the correlations should overlay (Figure 2.11). If the curves were not overlapping the z-position of the red pinhole was adjusted slightly, the x, y position aligned and then the overlap rechecked. The reason for the overlap of the curves can be easily explained. When there is a single species in the sample detectable in both channels as the species diffuses through the observation volume it is detectable in both channels simultaneously, giving rise to identical correlation curves. If the two detectors were not aligned properly then they would not be monitoring the same observation volume which would lead to differences in the amplitudes of the curves. If the red-channel detector was misaligned and only

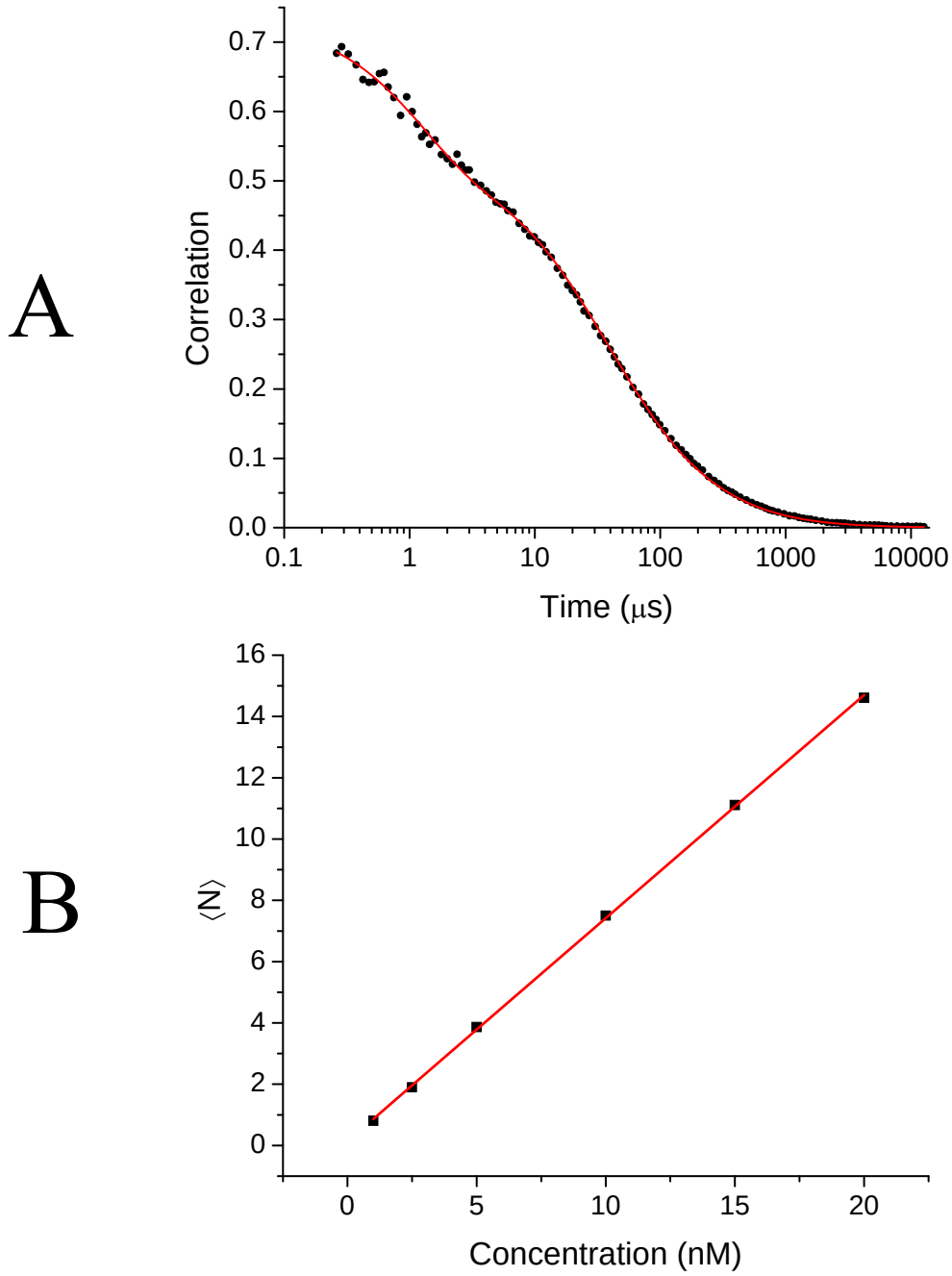

Figure 2.10: (A) Fit (red line) of 2.5 nM fluorescein autocorrelation (black circles) used in the linear response study. $\langle N \rangle = 1.897 \pm 0.009$, $\tau_D = 38.7 \pm 0.6$ μs, triplet fraction = 0.204 ± 0.004, and $\tau_T = 1.14 \pm 0.05$ μs. The axial radial ratio was fixed to a value of 10 (B) Linear fit with R^2=0.9998 (red line) to concentration vs. average number of molecules in the focal volume (black squares) demonstrating no deviation from linearity with high count rates (100 kHz at 20 nM).

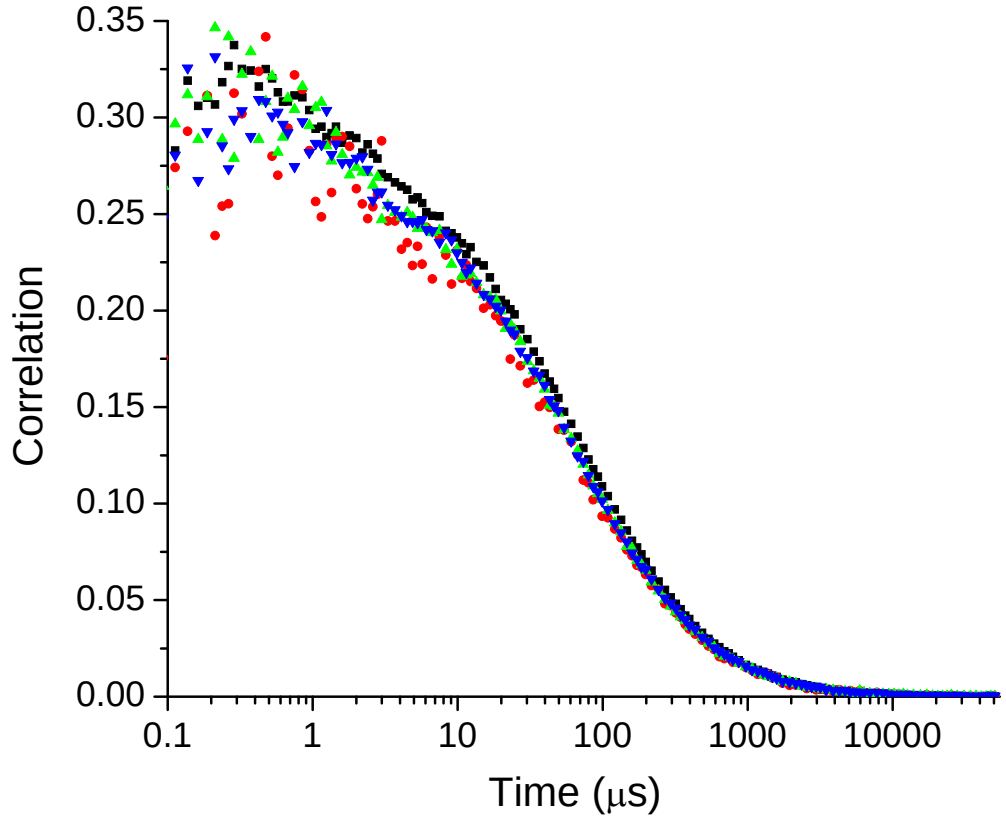

Figure 2.11: $G_{GG}(\tau)$ (black squares), $G_{RR}(\tau)$ (red circles), $G_{GR}(\tau)$ (green triangles), and $G_{RG}(\tau)$ (blue inverted triangles). The high amount of overlap demonstrates good alignment of the two channels.

observed half of the probe volume that the green detector measured then the initial amplitude would be higher for the red detector due to missing half of the molecules. When the system is aligned the autocorrelations for each channel will be the same due to the probe volumes being identical. The cross-correlations between the channels will overlap the autocorrelations because the probe volumes of each channel are overlapped. The synchronization is easily checked by noting the presence of cross-correlation between the green and red channels. If the channels were not synchronized there would be no cross-correlation present in the data.

2.3. Single-Molecule Imaging

To perform measurements on immobilized single molecules, the system was equipped with a piezoelectric scanning stage (Nano H100, Mad City Labs, Madison, WI) controlled by a National Instruments PCI-6052E card. The voltage output of the card was software driven using custom produced scanning software (Scan 2000, Eric Sanchez, Portland, OR), which allowed for the positioning of the molecule of interest over the probe volume. Details of the setup are discussed in Allen.[7]

2.4. FCS Simulations

The program SimFCS (Enrico Gratton, LFD, UC Irvine) was used to generate simulated photon streams that were then correlated and fit to the appropriate model. The program was capable of simple diffusion simulations, simulating molecules with multiple static FRET states, or a single dynamic FRET state along with static FRET

states. For every simulation performed the total number of molecules used in the simulation box was 300 with a probe volume profile radial waist of 0.500 microns and an axial waist of 2.5 microns. The diffusion coefficient for the molecules was set to 1.3×10^{-6} cm^2/sec. Using the above parameters a preliminary simulation was performed using a 200 kHz timebase with sixteen million steps and a particle brightness of 160,000 counts-per-second-per-molecule (cpsm) to provide a baseline for the transit time and average number of molecules that result from the fit of the autocorrelation. Figure 2.12 shows the results from the simulation and the fit to the correlation.

2.5. Time Correlated Single Photon Counting (TCSPC)

2.5.1. Instrumentation

The TCSPC instrument was comprised of a pulsed laser source, a detection train to collect and select the emission wavelengths, high time resolution detectors, and a counter-timer card for data acquisition. The system used in this work has been described in great detail previously.[8] Figure 2.13 shows the block diagram for the system used in this work. The MIRA 900 Titanium-Sapphire laser has a tuning range of 740-980 nm and was cavity dumped at the desired repetition rate. The output of the laser was then frequency doubled (second harmonic generation (SHG)) or tripled (third harmonic generation (THG)). The detection train was in a T-format allowing for the simultaneous detection of the parallel and perpendicular emission for use in time-resolved fluorescence anisotropy measurements. While this system has many

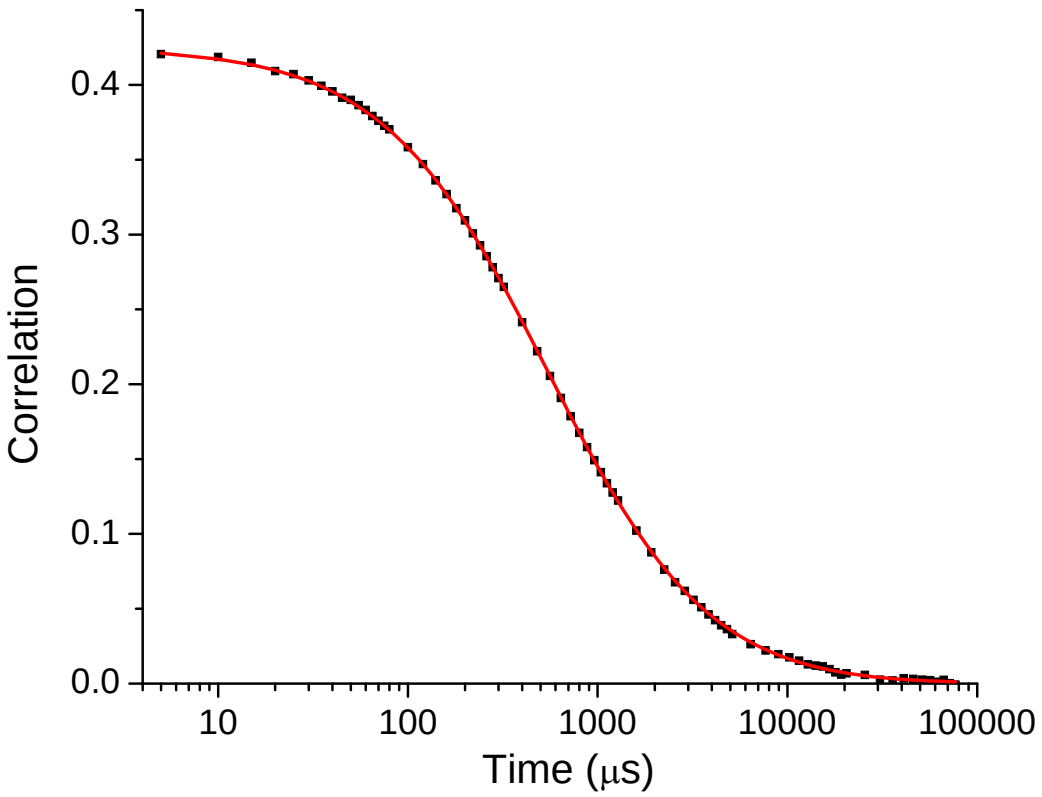

Figure 2.12: Correlation (black squares) and fit (red line) to equation 1.9 with $\langle N \rangle = 2.348 \pm 0.004$ and $\tau_D = 544 \pm 3$ μs for FCS simulation of simple diffusion to provide a baseline for further simulations with more complex data.

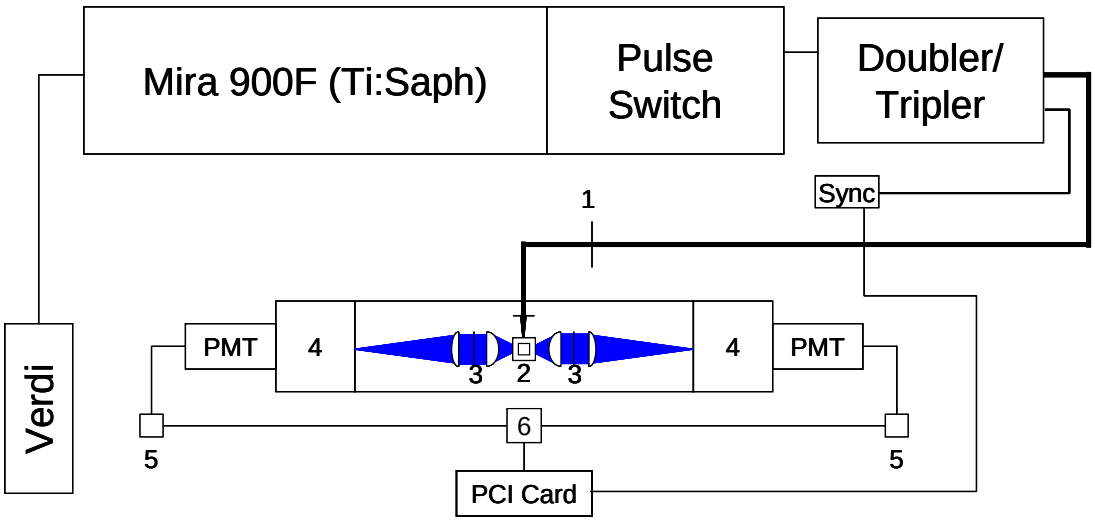

1 – Variable Neutral Density Filter
2 – Sample Holder
3 – Emission Linear Polarizers
4 – Monochromators
5 – Pre-amps with Overload Protection
6 – Router

Figure 2.13: Block diagram of the TCSPC system.

advantages over the previously used dye-laser system, one major disadvantage was the tuning range for the laser as demonstrated in Figure 2.14. It was not possible to excite a dye like Texas Red with the current system, and many other visible dyes fall into that dead range of the system.

In order to gain access to wavelengths in the 500-600 nm range a photonic crystal fiber (PCF) was purchased (0.5 m NL-PM-750 ThorLabs, Newton, NJ). The output from the MIRA was coupled into the fiber and through non-linear processes visible wavelengths were generated in the fiber. If enough pulse energy of the appropriate wavelength is coupled into the fiber, it is possible to generate a supercontinuum. Figure 2.15 contains the output of the fiber using different pumping wavelengths. To perform a measurement, an excitation filter (Chroma, Rockingham, VT) was placed after the fiber output to pass only a band of the desired wavelength. The excitation filters measured were 514, 543, 594, and 647 nm, with all of them designed with a 10 nm bandpass. When pumping at 800 nm the powers measured after each excitation filter were 215, 155, 50, and 30 μW respectively. To perform a measurement, however, the output polarization needed to be cleaned up using a linear polarizer and a small portion of the beam used for the sync pulse. After the addition of these components in the optical train the power measured for 594 nm was cut to 20 μW which was sufficient for TCSPC measurements. While a supercontinuum was never achieved using the PCF, the powers measured after the fiber were sufficient for performing TCSPC measurements.

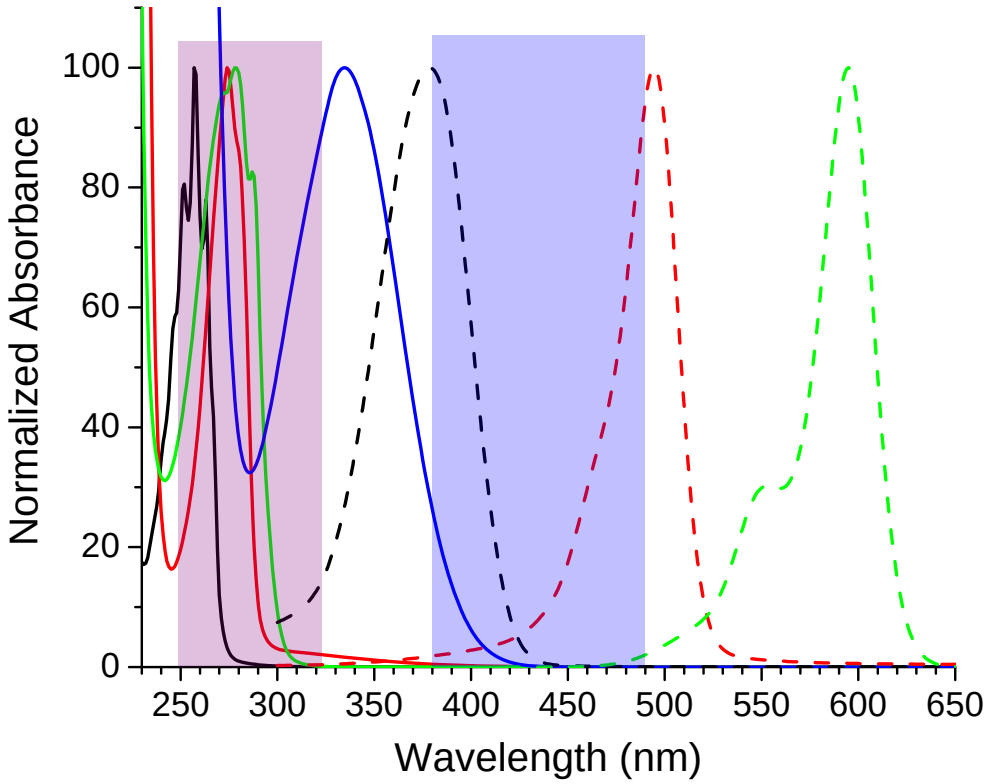

Figure 2.14: TCSPC system tuning range for THG (purple shade) and SHG (blue shade) overlaid with absorbance spectra of common fluorophores, phenylalanine (black line), tyrosine (red line), tryptophan (green line), dansyl (blue line), coumarin (black dashed line), Alexa Fluor 488 (red dashed line), and Texas Red (green dashed line). All spectra were normalized to a peak absorbance of 100.

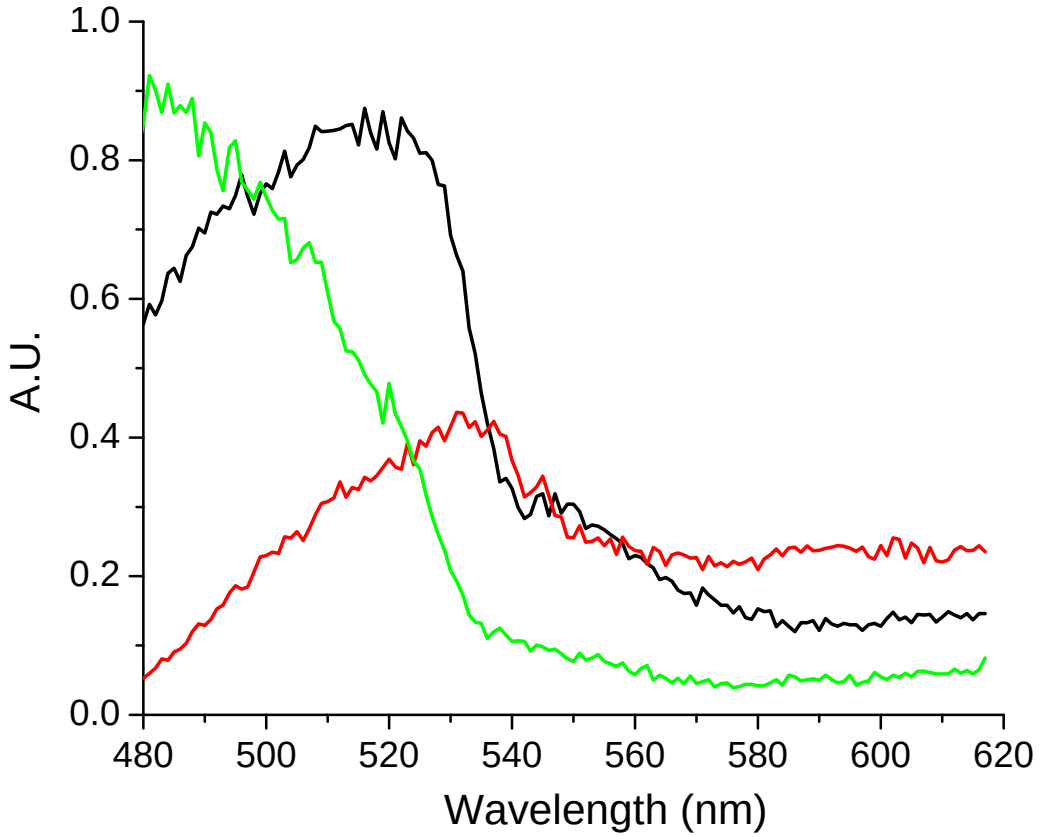

Figure 2.15: Wavelength output of PCF with different pump wavelengths. 770 nm (red line), 800 nm (black line), and 900 nm (green line). All measurements were performed using a repetition rate of 2.28 MHz.

Lifetime measurements were performed by setting the emission polarizer to the magic angle (54.7°) and collecting the fluorescence decay. Anisotropy was measured by setting one emission polarizer to vertical (0°) and the emission polarizer on the opposite side of the detection system to horizontal (90°). The vertical and horizontal fluorescence decays were measured for two separate samples. The first was a sample of free dye to allow for the measurement of the g-factor and the second sample was measured directly following the g-factor measurement using the sample of interest.

2.5.2. Data Analysis

Analysis of TCSPC data was performed using two methods. The first involved the use of a solver routine written in Excel that performed an iterative reconvolution of the model with the measured instrument response function, which was then compared with the data. The model was then adjusted and the convolution was performed again. The model used was a single or multi-exponential decay, depending on the system under measurement. In the case of distributed lifetimes, the maximum entropy algorithm was employed using software from Maximum Entropy Data Consultants Ltd. (Suffollk, UK).

The ME method fits the data by optimizing the amplitudes of fixed, logarithmically spaced lifetimes subject to a maximum entropy constraint, which minimizes sharp modulations in the amplitudes as a function of lifetime. Hence, the

method identifies the decay components without an *a priori* assumption of what the number of decay components should be.[9]

Anisotropy data was fit using a similar iterative reconvolution procedure by simultaneously fitting the vertical and horizontal decays to equations 2.5 and 2.6:

$$I_V(t) = \frac{1}{3} I(t)\left[1 + 2r(t)\right] \tag{2.5}$$

$$I_H(t) = \frac{1}{3} I(t)\left[1 - r(t)\right] \tag{2.6}$$

The function r(t) is the rotational dynamics of the molecule or the anisotropy decay and I(t) is the fluorescence lifetime decay. The anisotropy decay r(t) can be written as shown in equation 2.7:

$$r(t) = (r_0)e^{(-t/\phi)} \tag{2.7}$$

Where r_0 is the initial anisotropy and ϕ is the rotational correlation time. For one-photon excitation the maximum value for r_0 is 0.4 with most visible fluorophores having an r_0 close to the limit. The anisotropy r(t) can be calculated directly from the data using equation 2.8:

$$r(t) = \frac{g * I_V(t) - I_H(t)}{g * I_V(t) + 2I_H(t)} \tag{2.8}$$

Where g is the g-factor measured as described previously.

To test the photonic crystal fiber arrangement, it was necessary to measure both a lifetime decay and an anisotropy for a fluorophore in that region of the spectra. The tests were necessary, as the fiber had not been used previously for lifetime and anisotropy measurements so the decay characteristics were not known. The dye

Texas Red was chosen for testing as it is a commonly used dye in this work and represented a dye that was not possible to excite without the PCF. The MIRA laser was tuned to 800 nm and coupled into the fiber. A 1-inch, 594/10x excitation filter (Chroma, Rockingham, VT) was placed after the fiber and aligned onto the sync diode and into the detection system. Figure 2.16 shows the block diagram for the final system arrangement using the PCF. The monochromators were set to monitor emission at 615 nm and the lifetime collected with the emission polarizers set to the magic angle. Figure 2.17 contains the data and resulting fit for the lifetime of Texas Red. Using the same sample, one emission polarizer was rotated to vertical and the other set to horizontal. Figure 2.18 contains the results from the anisotropy measurement of Texas Red free dye fit to a single rotational correlation time.

2.6. Sample Preparation

2.6.1. Preparation of CaM Mutants

In order to conduct single-molecule fluorescent studies of CaM, it needed to be tagged with a highly fluorescent dye. Several different chemistries can be used for this purpose but one of the most common and selective is through the use of the thiol group on a cysteine residue reacting with a maleimide functional group on the dye.

The sequence of wild-type CaM conveniently contains no cysteine residues allowing for minimal perturbation of the protein through single point mutations of select residues. The mutants used in this work included T34C-T110C-CaM, T34C-CaM, S17C-T117C-CaM, and T5C-T44C-CaM. The mutant sequences for CaM

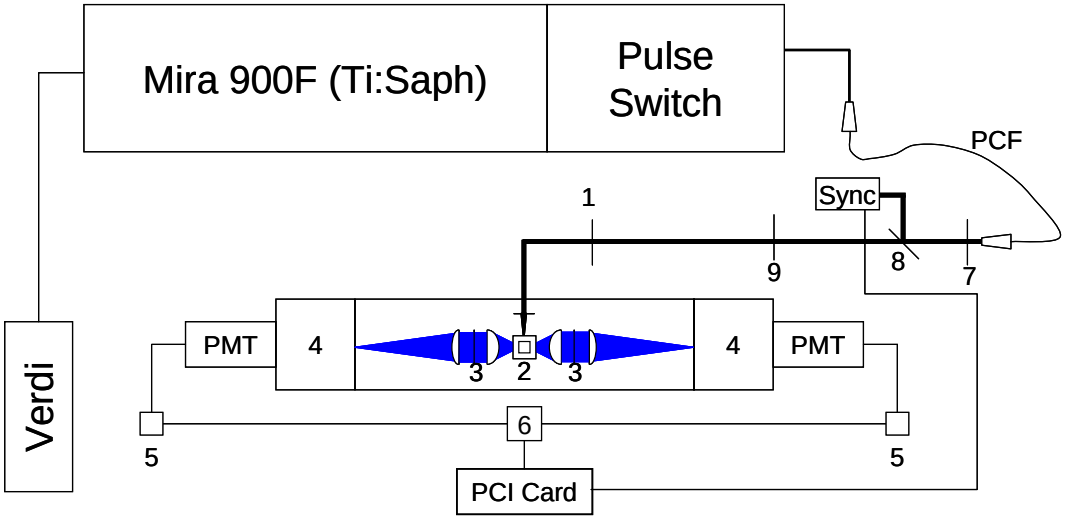

1 – Variable Neutral Density Filter
2 – Sample Holder
3 – Emission Linear Polarizers
4 – Monochromators
5 – Pre-amps with Overload Protection
6 – Router
7 – Excitation Filter
8 – Glass coverslip
9 – Linear Polarizer

Figure 2.16: Block diagram of TCSPC system configured for use with the photonic crystal fiber.

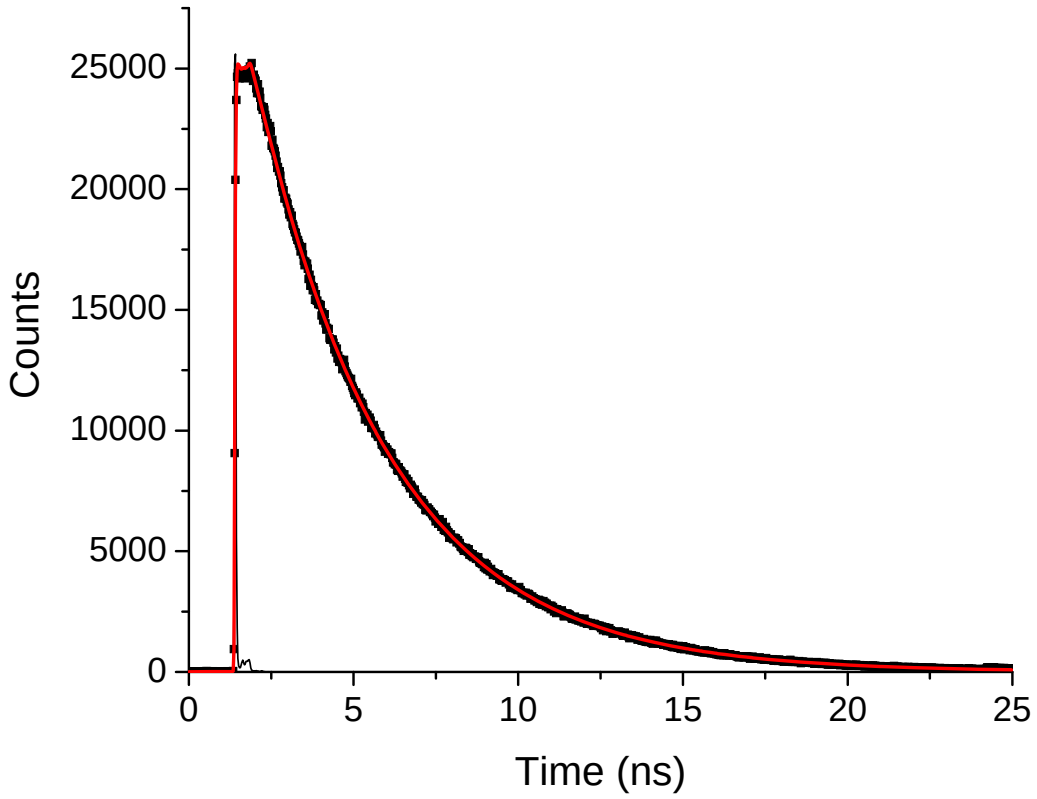

Figure 2.17: Instrument response function (black line), fluorescence lifetime data (black squares), and single exponential fit of 4.03 ± 0.01 ns (red line) to Texas Red free dye in standard storage buffer. The data was collected using ~6 μW of laser power resulting in a count rate of ~18,000 cps.

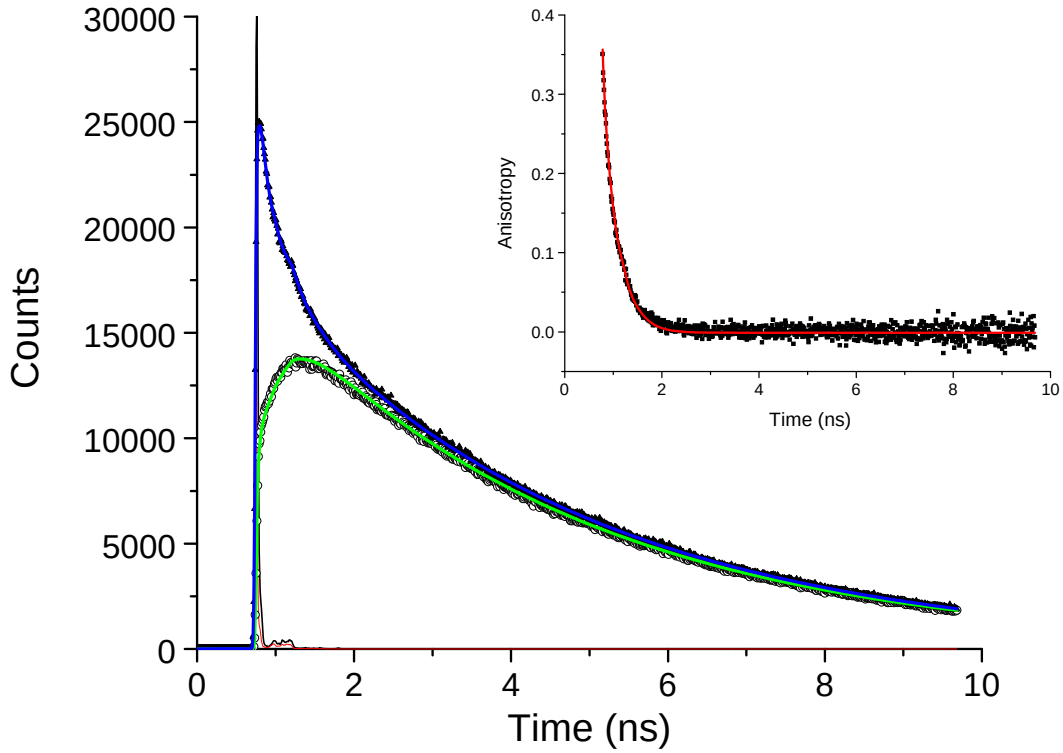

Figure 2.18: Time-resolved fluorescence anisotropy measurement of Texas Red dye in the storage buffer. The IRF_H (black line), IRF_V (red line), I_H (open circles), I_V (black triangles) were simultaneously fit to I_H fit (green line) and I_V fit (blue line). The inset shows the calculated anisotropy decay (black squares) with the corresponding fit (red line) to $r_0 = 0.37 \pm 0.01$ and $\phi = 270 \pm 10$ ps.

were transformed into *E. coli*, which were then ready for overexpression. Purification of the expressed CaM protein was carried out using the routine purification procedure for wild-type CaM using affinity chromatography on a phenyl sepharose column.[7,10] The protocol for preparation of the grown cells for purification is given by Allen.[7] The setup used in this work was a BioRad econo-column equipped with a flow adaptor to eliminate the dead volume above the column packing material. A peristaltic pump was placed before the column so that solvent was pushed rather than pulled through the column. This avoided the introduction of bubbles into the 5 μL flow cell of the fixed wavelength detector (DFW-20, D-Star Instruments, Manassas, VA) operating at 280 nm. The integrator output of the detector was directed into a Vernier LabPro module using the voltage probe. The voltage was monitored on a PC computer using the supplied software, allowing for monitoring of the absorbance as a function of time. Table 2.1 shows the solutions used for the affinity chromatography separation. The column was pre-equilibrated with buffer A. The prepared soluble fraction of the cell contents (about 50 mL volume) was loaded onto the phenyl sepharose column at a flow rate of 1 mL/min. After loading of the sample the column was washed with buffer A for one hour. The washing solution was then changed to buffer B for one hour to remove any non-specifically bound molecules. The solution was then changed back to A for one hour to remove the high salt from buffer B. Buffer C was then used to elute the CaM protein. The peak was collected from the column and dialyzed in 4 L of buffer A

Table 2.1: CaM Affinity Chromatography Solutions.

Buffer Name	Buffer Make-up
A	50 mM TRIS HCl 1 mM $CaCl_2$ pH 7.5
B	50mM TRIS HCl 1 mM $CaCl_2$ 0.5 M NaCl pH 7.5
C	10 mM TRIS HCl 10 mM EDTA pH 7.5

twice to get the CaM in the sample back to a Ca^{2+} bound state so that it would bind to the column during the second purification round.

The column was washed with 250 mL of 8 M urea and then equilibrated with buffer A for the next day. The same protocol was followed for the second purification round except for the last step where the dialysis buffer for the collected CaM sample was the storage buffer of 10 mM HEPES, 100 mM KCl, 1 mM $MgCl_2$, and 0.1 mM $CaCl_2$ adjusted to pH 7.4 with HCl and KOH. Figure 2.19 contains example chromatograms from day one and day two of the affinity purification.

After dialysis was completed, the UV absorbance of the sample was recorded. Using an extinction coefficient of 2810 $M^{-1}cm^{-1}$ at 274 nm, the concentration of the sample was then calculated. The CaM sample was then aliquoted so that each vial contained 2.1 mg of CaM (equivalent to 125 nanomoles) and was placed in a -80 °C freezer. Mass spectrometry was also performed on each sample to verify the correct molecular mass which for T34C-T110C-CaM and T5C-T44C-CaM was 16710 Da and for S17C-T117C-CaM was 16724 Da.

2.6.2. Labeling of CaM mutants

Throughout this work the various cysteine mutants of CaM were labeled with one or more fluorophores using a protocol similar to that developed by Allen *et al*.[11] For single cysteine mutants the labeling procedure was as follows, a 2.1 mg aliquot of the appropriate CaM mutant was mixed with 100 μL of 5 mM *tris*(2-carboxyethyl)phosphine (TCEP) freshly prepared in the storage buffer and allowed

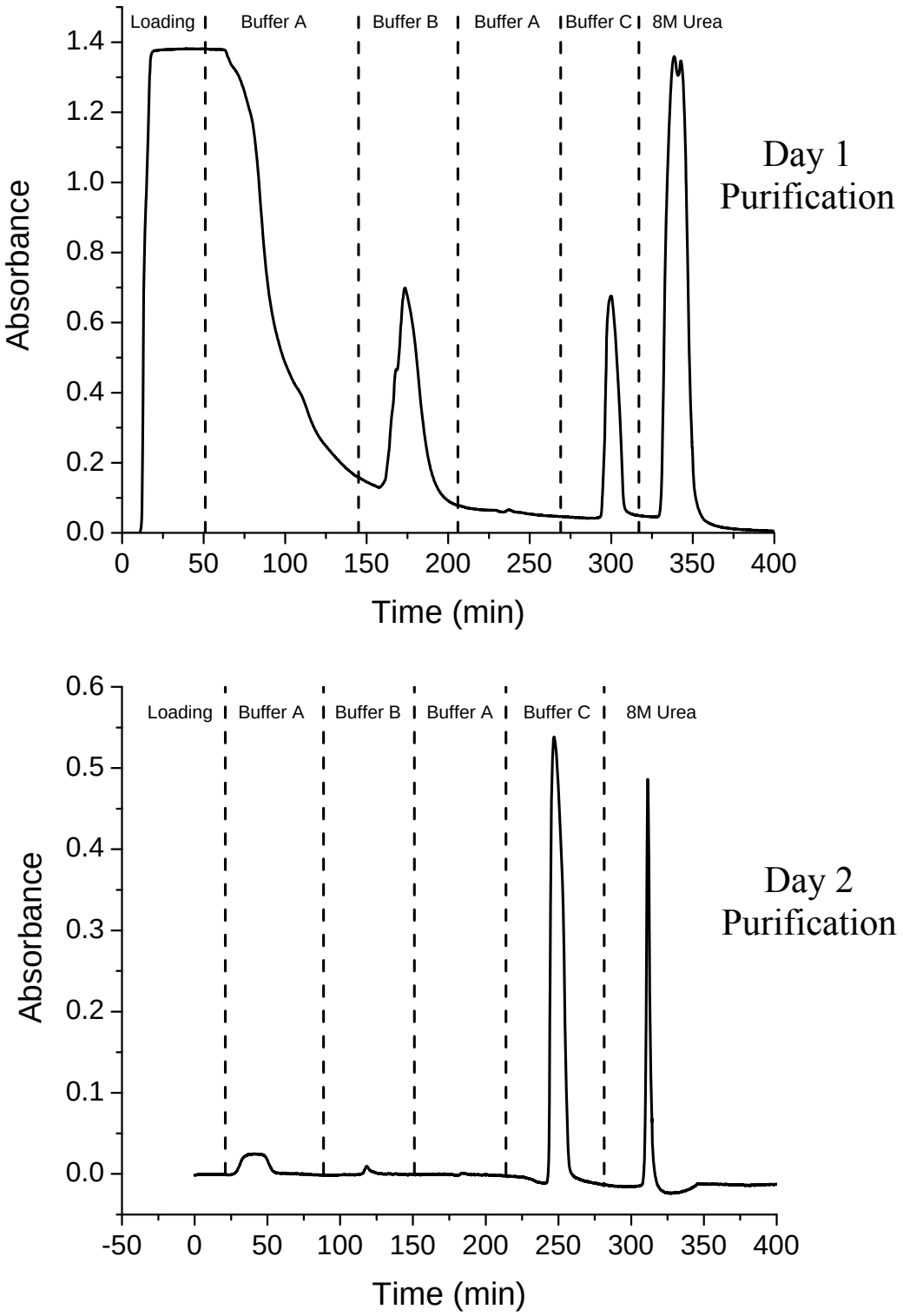

Figure 2.19: Example chromatograms from the purification of T5C,T44C-CaM. Absorbance was measured at 280 nm.

to stir for 5 minutes. While stirring the protein, 1 mg of the fluorescent dye was dissolved in 500 μL of the storage buffer. If the dye was not very soluble in water, it was first dissolved in 250 μL of DMSO and then diluted with 250 μL of the storage buffer. To the protein/TCEP mixture, 1 mL of 2 M NaCl in the storage buffer was added and the solution was stirred for 5 minutes. The dye solution was added dropwise to the protein with continual stirring. The mixture was allowed to react for 1-1.5 hours in the dark. To separate the unreacted dye from labeled protein, the mixture was loaded on the head of a gravity flow 40 cm x 1 cm Sephadex G-25 column equilibrated with the storage buffer. The separation was followed visually and the first colored band containing the labeled protein was collected.

Labeling a single protein with both the donor and acceptor of a FRET pair required the ability to either label each site sequentially or to label the sites simultaneously and separate the mixture of possible dye combinations to obtain the single donor, single acceptor labeled protein. Previous work demonstrated the ability with CaM to label the sites simultaneously and then separate the mixture without losing protein function.[11]

The previous protocol involved the simultaneous labeling of T34C,T110C-CaM with Alexa Fluor 488 (donor) and Texas Red (acceptor) (Invitrogen, Carlsbad, CA) and successfully separating the mixture using HPLC.[11-13] The following sections discuss the labeling of the new mutants of CaM and the protocols used for each.

2.6.2.1. Protocol for Labeling and Purification of S17C,T117C-CaM with Alexa Fluor 488 and Texas Red

This protocol was employed for the simultaneous labeling and subsequent separation of the donor-acceptor labeled protein.

1. A 2.1 mg vial of CaM was mixed with a 6-fold molar excess of TCEP. A stock solution of TCEP was prepared by making a 15 mM solution of TCEP in the storage buffer. Pipetting 50 μL of this solution into the protein resulted in the appropriate concentration. The mixture was allowed to stir for 5 minutes.
2. While stirring, 0.5 mg of Texas Red maleimide was dissolved in 200 μL of DMSO. A 1 mg vial of Alexa Fluor 488 maleimide was dissolved in 300 μL of storage buffer. The two dye solutions were then mixed well to prepare to react with the CaM.
3. A solution of 4 M NaCl in the storage buffer was prepared and 500 μL was pipetted into the TCEP/CaM solution and stirred for 5 minutes.
4. The dye mixture was added dropwise to the protein solution and allowed to react in the dark at room temperature for 90 minutes.
5. After 90 minutes the unreacted dye was separated from the labeled protein on a 40 cm X 1 cm Sephadex G25 size exclusion column equilibrated with the storage buffer.

Upon collection of the labeled protein, the donor-acceptor species required separation from the donor-donor and acceptor-acceptor labeled protein. This was accomplished using a Waters HPLC-UV system consisting of a Waters model 600 pump, a model 2487 dual-wavelength absorbance detector, a DG-2 solvent degassing system, and a low pressure quaternary solvent mixing system. A C_{18} 4.6 mm x 250 mm 5 μm particle size column (Vydac 218TP4) was used for the separation.

In order to sufficiently separate the slightly different protein species in the sample a gradient separation was required. The largest improvement in separation efficiency was achieved through adjustment of the flow rate and gradient program used. Table 2.2 contains the gradient settings used for the separation of S17C,T117C-CaM labeled with Alexa Fluor 488 and Texas Red. Mobile phase A consisted of 95% water, 5% acetonitrile, and 0.1% trifluoroacetic acid. Mobile phase B consisted of 95% acetonitrile, 5% water, and 0.1% trifluoroacetic acid. All solvents were of HPLC grade so filtering of the mobile phase was not required. During the separation the absorbance was monitored at 493 nm (Alexa Fluor 488 maximum) and 593 nm (Texas Red maximum). Fractions were collected for each of the suspected labeling possibilities (Figure 2.20) and submitted for mass spectrometry to verify the species in that fraction.

The samples were dialyzed from the HPLC solvents to the storage buffer and the concentration was determined through absorbance measurement of the donor and acceptor dye peaks.

2.6.2.2. Protocol for Labeling and Purification of T5C,T44C-CaM with Alexa Fluor 488 and Atto 740

The protocol for labeling CaM-5-44 with Alexa Fluor 488 and Atto 740 maleimide was very similar to the protocol discussed in the previous section. The only difference in the labeling protocol involved the mixing of 1 mg of Alexa Fluor 488 maleimide dissolved in 250 μL of storage buffer and 1 mg of Atto 740 maleimide

Table 2.2: Gradient settings for separation of S17C,T117C-CaM labeled with Alexa Fluor 488 and Texas Red. All ramps were linear with time.

Segment	Time	Flow	%A	%B
1	0.01	1.50	100.0	0.0
2	7.00	1.50	100.0	0.0
3	14.00	1.50	62.0	38.0
4	50.00	1.50	44.0	56.0
5	54.00	1.50	0.0	100.0
6	61.00	1.50	0.0	100.0
7	66.00	1.50	100.0	0.0
8	75.00	1.50	100.0	0.0
9	75.01	0.00	100.0	0.0

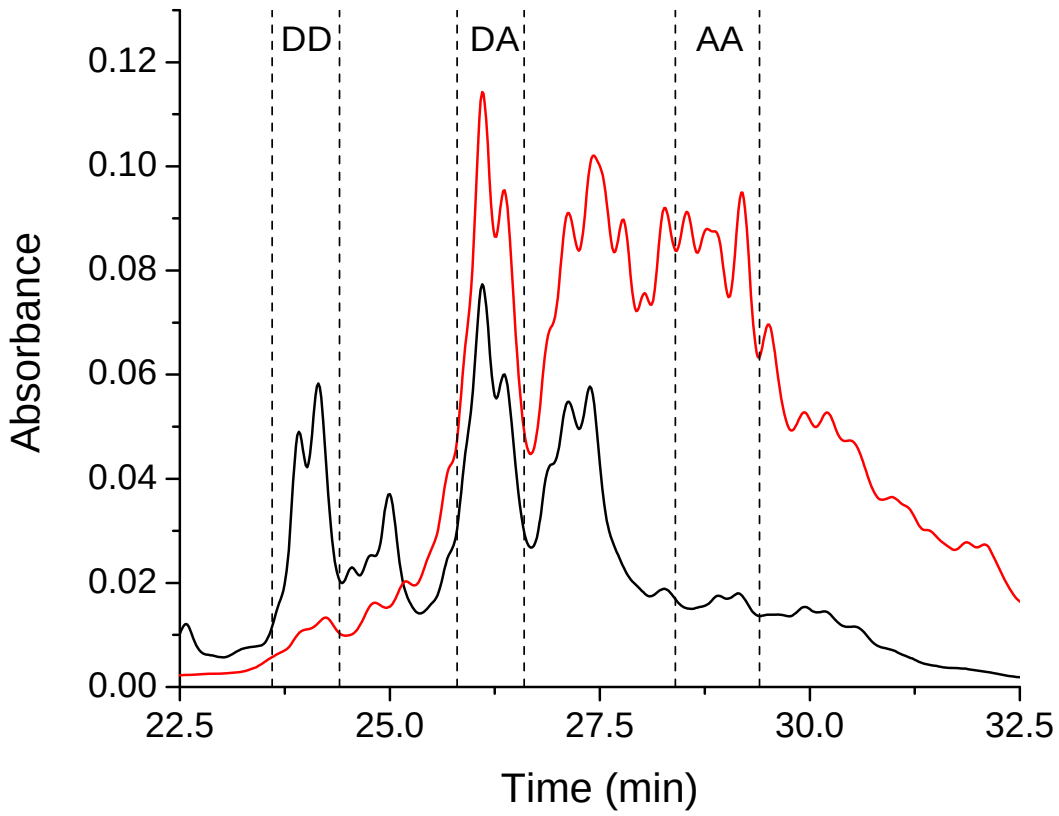

Figure 2.20: Example chromatogram for S17C-T117C-CaM Alexa Fluor 488-Texas Red purification. Alexa Fluor 488 (black line) absorbance monitored at 493 nm and Texas Red (red line) absorbance monitored at 593 nm. The dashed lines denote when the fractions were collected for each species.

dissolved in 250 μL of DMSO. The remainder of the labeling protocol remained the same.

The separation protocol consisted of the same two mobile phases as the previous section with some slight modifications to the gradient settings. Table 2.3 contains the gradient settings for the CaM-5-44 separation. The separation of the DA species was much better than other CaM mutants, as shown in Figure 2.21. It is possible that the combination of the dyes both on the N-terminal side of the CaM and the larger hydrophobic Atto 740 dye created a larger difference in the species with respect to the separation.

The collected fractions were dialyzed from the HPLC solvents to the storage buffer and the concentration was determined through absorbance measurement of the donor and acceptor dye peaks. Mass spectrometry was performed to verify the sample contents (Figure 2.22). The resulting mass agrees well with the expected mass for the donor-acceptor species. Calmodulin has a nominal mass of 16,710 Da, Alexa Fluor 488 maleimide has a nominal mass of 698 Da, and Atto 740 maleimide has a nominal mass of 591 Da. This results in a species with nominal mass of 17999 Da, in excellent agreement with the mass spectrum.

Table 2.3: Gradient settings for separation of T5C-T44C-CaM labeled with Alexa Fluor 488 and Atto 740. All ramps were linear with time.

Segment	Time	Flow	%A	%B
1	0.01	1.50	100.0	0.0
2	7.00	1.50	100.0	0.0
3	14.00	1.50	62.0	38.0
4	42.00	1.50	44.0	52.0
5	46.00	1.50	0.0	100.0
6	54.00	1.50	0.0	100.0
7	58.00	1.50	100.0	0.0
8	70.00	1.50	100.0	0.0
9	70.01	0.00	100.0	0.0

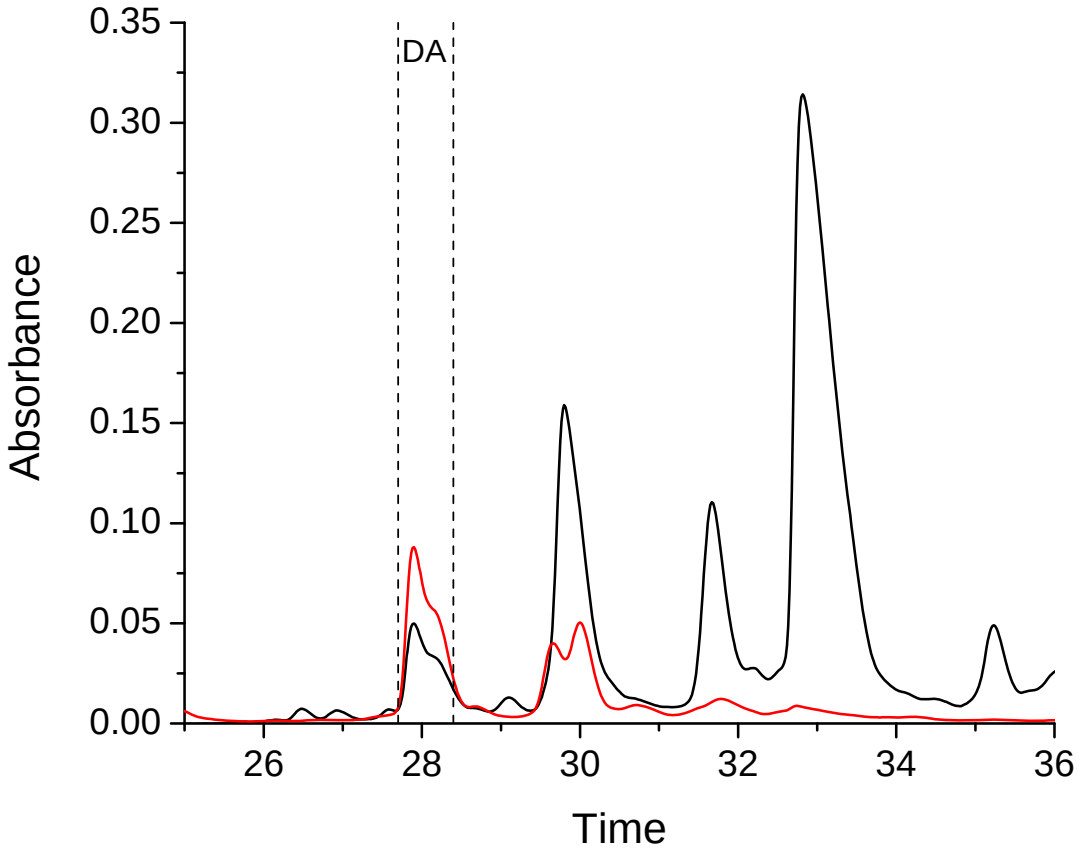

Figure 2.21: Example chromatogram for T5C-T44C-CaM Alexa Fluor 488-Atto 740 purification. Alexa Fluor 488 (black line) absorbance monitored at 493 nm and Atto 740 (red line) absorbance monitored at 700 nm. The dashed lines denote when the fractions were collected for the donor-acceptor species.

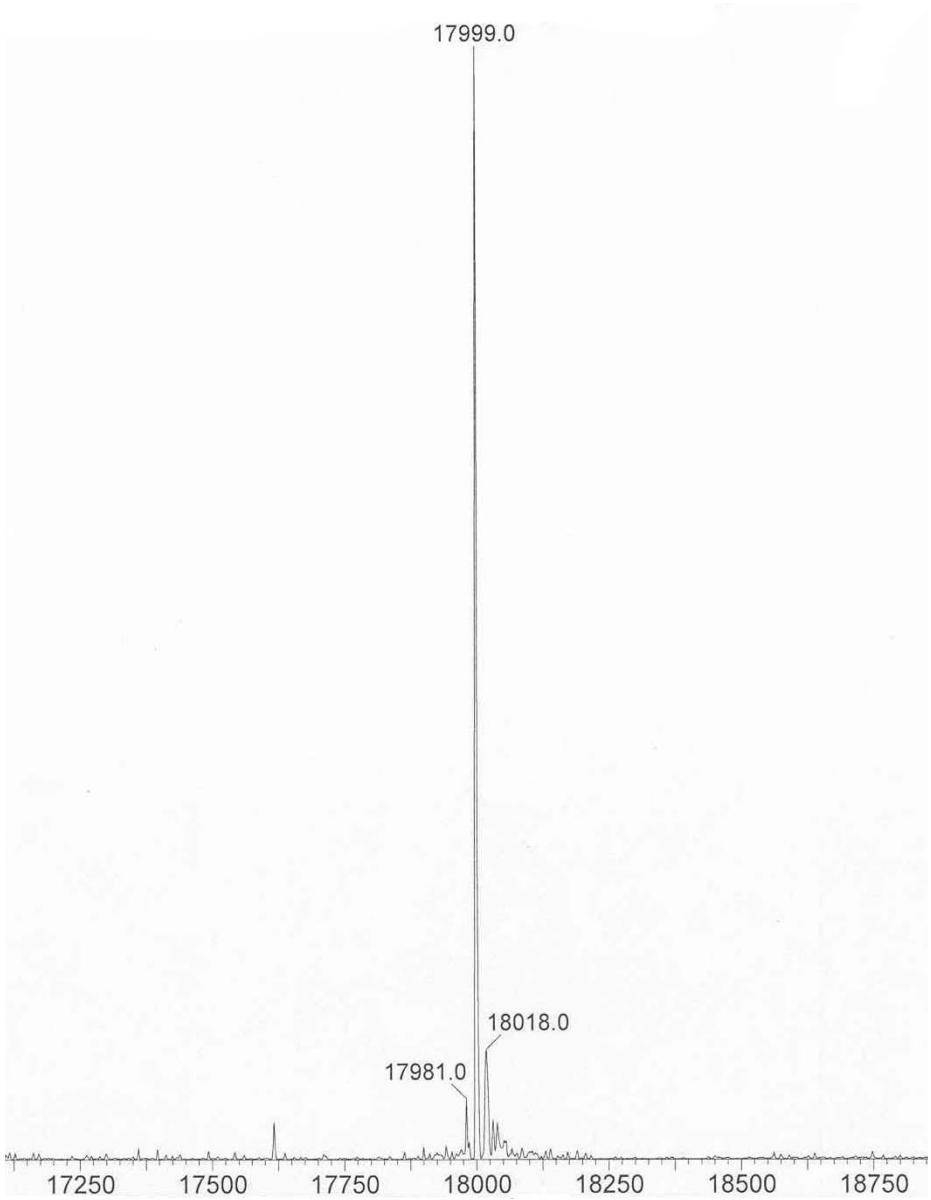

Figure 2.22: Mass spectrum of 5-44 CaM labeled with Alexa Fluor 488 maleimide and Atto 740 maleimide.

2.7. References

1. Walrafen, G. E., *Raman Spectral Studies of Effects of Temperature on Water Structure*. J. Chem. Phys., **1967**. 47(1): p. 114-126.

2. Davis, L. M., Williams, P. E., Ball, D. A., Swift, K. M., and Matayoshi, E. D., *Data Reduction Methods for Application of Fluorescence Correlation Spectroscopy to Pharmaceutical Drug Discovery*. Curr. Pharm. Biotechnol., **2003**. 4(6): p. 451-462.

3. Felekyan, S., Kuhnemuth, R., Kudryavtsev, V., Sandhagen, C., Becker, W., and Seidel, C. A. M., *Full Correlation from Picoseconds to Seconds by Time-Resolved and Time-Correlated Single Photon Detection*. Rev. Sci. Instrum., **2005**. 76(8): p.

4. Wahl, M., Gregor, I., Patting, M., and Enderlein, J., *Fast Calculation of Fluorescence Correlation Data with Asynchronous Time-Correlated Single-Photon Counting*. Opt. Express, **2003**. 11(26): p. 3583-3591.

5. Widengren, J., Mets, U., and Rigler, R., *Fluorescence Correlation Spectroscopy of Triplet States in Solution: A Theoretical and Experimental Study*. J. Phys. Chem., **1995**. 99(36): p. 13368-13379.

6. Zhao, M., Jin, L., Chen, B., Ding, Y., Ma, H., and Chen, D. Y., *Afterpulsing and Its Correction in Fluorescence Correlation Spectroscopy Experiments*. Appl. Opt., **2003**. 42(19): p. 4031-4036.

7. Allen, M. W., *Analytical Chemistry at the Extremes: Ultrafast and Single Molecule Fluorescence Spectroscopic Investigations of Biological Systems* **2004** Department of Chemistry, University of Kansas, Lawrence. 230 pp.

8. Unruh, J. R., *Development of Fluorescence Spectroscopy Tools for the Measurements of Biomolecular Dynamics and Heterogeneity* **2006** Department of Chemistry, Univeristy of Kansas. 237 pp.

9. Swaminathan, R., and Periasamy, N., *Analysis of Fluorescence Decay by the Maximum Entropy Method: Influence of Noise and Analysis Parameters on the Width of the Distribution of Lifetimes*. Proc. Indian Acad. Sci. Chem. Sci., **1996**. 108(1): p. 39-49.

10. Gopalakrishna, R., and Anderson, W. B., *Ca^{2+}-Induced Hydrophobic Site on Calmodulin - Application for Purification of Calmodulin by Phenyl-Sepharose Affinity-Chromatography*. Biochem. Biophys. Res. Commun., **1982**. 104(2): p. 830-836.

11. Allen, M. W., Urbauer, R. J. B., Zaidi, A., Williams, T. D., Urbauer, J. L., and Johnson, C. K., *Fluorescence Labeling, Purification and Immobilization of a Double Cysteine Mutant Calmodulin Fusion Protein for Single-Molecule Experiments*. Anal. Biochem., **2004**. 325(2): p. 273-284.

12. Allen, M. W., Bieber Urbauer, R. J., and Johnson, C. K., *Single-Molecule Assays of Calmodulin Target Binding Detected with a Calmodulin Energy-Transfer Construct*. Anal. Chem., **2004**. 76(13): p. 3630-3637.

13. Slaughter, B. D., Allen, M. W., Unruh, J. R., Urbauer, R. J. B., and Johnson, C. K., *Single-Molecule Resonance Energy Transfer and Fluorescence Correlation Spectroscopy of Calmodulin in Solution.* J. Phys. Chem. B, **2004**. 108(29): p. 10388-10397.

3. Fluorescence Correlation Spectroscopy of FRET-Pair Labeled Polyproline

3.1. Introduction

Fluorescence correlation spectroscopy is sensitive to any fluctuations in the fluorescence intensity as a function of time. The most common fluctuations are due to diffusion, triplet dynamics, and other quenching events as discussed in Chapter 1.4.

Introduction of donor and acceptor fluorophores into the same protein molecule opens new pathways for variation in the fluorescence intensity through Förster resonance energy transfer (FRET). The new fluorescence states make the combination of FCS and FRET a potentially powerful tool for probing molecular conformations and dynamics, as illustrated by a number of recent publications.[1-9] These new fluorescent states may be essentially *static*, *i.e.* involving interchange between FRET states that are slow on the time scale of diffusion through the detection volume, or they may be *dynamic*, leading to fluctuations in fluorescence on the time scale of the molecules' transit through the focal region. Changes in the FRET efficiency while the molecule is in the focal volume introduce fluctuations in the fluorescence signal, which will be reflected in the correlation functions. It is therefore critical to develop methods of analysis of FCS data that can clearly distinguish FRET dynamics from other sources of fluctuations.

In this chapter the relationship between FCS and FRET are studied in a system where dynamics are thought to occur on a time scale much faster or slower than the time scale of transit through the observation volume. As a result, it is expected that the FRET states will be static on the FCS time scale. It is shown that

the amplitudes of the FCS correlation functions, both autocorrelations and cross-correlations, are sensitive to the existence of multiple FRET states. Furthermore, analysis of the time dependence confirms the absence of dynamics on the time scale of transit through the focal region.

Methods of globally fitting FCS auto-correlation and cross-correlation decays for a FRET system in the absence of fluctuations in the distance between them will be discussed. If there are no fluctuations in the signal during the transit time then the correlation curves calculated from the fluorescence signal should only contain diffusional and triplet components on time scales of microseconds or longer. A system with effectively static FRET states can be found in polyprolines with lengths ranging from 6-20 prolines.[10-12] Using a polyproline sample labeled with donor and acceptor fluorophores, the effect that FRET has on the auto and cross-correlation initial amplitudes was investigated.

3.2. Theory

The basic theory behind FCS was given in Chapter 1.4 and will be expanded upon in this section. In typical FCS measurements, the initial amplitude of the correlation gives the average number of molecules in the focal volume during the measurement. This relationship breaks down when the species under study contains multiple FRET states. In this chapter the appropriate functions for fitting FCS autocorrelation and cross-correlation data generated with a static FRET system will be described. Similar equations have been derived previously in the Gratton group

for a single FRET state with multiple species (donor-donor, donor-acceptor, etc).[13] If the FRET efficiency is static on the time scale detectable by FCS (microseconds to milliseconds in this case), then the presence of multiple FRET states will affect only the initial amplitudes because there is no time dependence of the FRET efficiency.[13] For a system with static FRET states *i*, the fluorescence signal in the donor and acceptor channels (in this case for two FRET states) is written as equations 3.1 and 3.2.

$$I_G(t) = Q_1^D N_1(t) + Q_2^D N_2(t) \tag{3.1}$$

$$I_R(t) = Q_1^A N_1(t) + Q_2^A N_2(t) \tag{3.2}$$

Where N_i is the number of molecules in FRET state i and $Q_i^D = q_D \sigma_D [\phi_D (1 - E_i)]$, where q_D is the detection efficiency for the donor, σ_D is the excitation cross section, ϕ_D is the quantum yield of the donor fluorophore, and E_i is the FRET efficiency for species *i*. Similarly, for the acceptor channel, $Q_i^A = q_D \sigma_D I_0 \gamma_i$ with $\gamma_i = [\beta E_i + (1 - E_i)\alpha]$ where β is the brightness factor of the FRET excited acceptor relative to the directly excited donor, and α is the fractional contribution of cross-talk of donor emission into the acceptor channel. (No direct excitation of acceptor was assumed, although correction for it could readily be incorporated as well.)

Four correlations can be calculated from the green (donor) and red (acceptor) data streams as given in equation 3.3:

$$G_{xy}(\tau) = \frac{\langle \delta I_x(t) \delta I_y(t+\tau) \rangle}{\langle \delta I_x(t) \rangle \langle \delta I_y(t) \rangle} \tag{3.3}$$

where *x* and *y* are the green or red signal channels and $\langle\cdots\rangle$ denotes the average over *t*. Equation 3.3 gives two autocorrelation functions $G_{xx}(\tau)$ and $G_{yy}(\tau)$, and two cross-correlation functions $G_{xy}(\tau)$ and $G_{yx}(\tau)$. Fluctuations in fluorescence intensity for species i are given by equation 3.4:

$$\delta I_i(t) = \int W(r)\delta C_i(r,t)dr \tag{3.4}$$

where W(r) is the function describing the shape of the probe volume (a three dimensional Gaussian in this case) and $\delta C_i(r,t)$ is the fluctuation in the probe volume particle concentration at time t for FRET state i (where i = 1 or 2 for two state system). Using equations 3.1, 3.2, 3.3, and the relationship given in equation 3.4, the functions for the four correlations can be derived. The correlation $G_{xy}(\tau)$ can now be written as equation 3.5.

$$G_{xy}(\tau) = \frac{\iint W_x(r)W_y(r')\sum_i \langle \delta C_i(r,t)\delta C_i(r',t+\tau)\rangle drdr'}{\left(\sum_{i,j}\langle C_i\rangle\langle C_j\rangle\right)\left(\iint W_x(r)W_y(r')drdr'\right)} \tag{3.5}$$

Because the FRET states are static, the presence of multiple FRET states affects only the initial amplitudes, not the time dependence of the correlation functions, which greatly simplifies equation 3.5.

By substituting $C_1 = (f)C_{total}$ and $C_2 = (1\text{-}f)C_{total}$ for the donor-acceptor labeled species in equations 3.1 and 3.2 and then inserting those expressions into equation 3.5, the initial amplitudes of the correlation functions (apart from contributions from processes other than diffusion, such as triplet kinetics or photon antibunching) can be written as equations 3.6-3.8.

$$G_{GG}(0) = \frac{1}{N_{tot}}\left[\frac{(1-E_1)^2 f_1 + (1-E_2)^2(1-f_1)}{[(1-E_1)f_1 + (1-E_2)(1-f_1)]^2}\right] \tag{3.6}$$

$$G_{RR}(0) = \frac{1}{N_{tot}}\left[\frac{\gamma_1{}^2 f_1 + \gamma_2{}^2(1-f_1)}{[\gamma_1 f_1 + \gamma_2(1-f_1)]^2}\right] \tag{3.7}$$

$$G_{GR}(0) = \frac{1}{N_{tot}}\left[\frac{(1-E_1)\gamma_1 f_1 + (1-E_2)\gamma_2(1-f_1)}{[(1-E_1)f_1 + (1-E_2)(1-f_1)][\gamma_1 f_1 + \gamma_2(1-f_1)]}\right] \tag{3.8}$$

Equations 3.6-3.8 predict the dependence of the initial amplitudes for the correlation functions on the FRET efficiencies of the states present. Note that if only a single FRET state exists (f_1=1), the initial amplitudes predicted by equations 3.6-3.8 are identical. In the presence of two or more static FRET states the initial amplitudes are no longer equal, with $G_{GR}(0)$ falling below $G_{GG}(0)$ and $G_{RR}(0)$. Thus, the initial amplitudes of the auto and cross-correlation functions for a FRET system can be used to diagnose the presence of multiple FRET states.

These expressions are readily extended to any number of FRET states. For example, in a three FRET system the initial amplitudes can now be written as equations 3.9-3.11.

$$G_{GG}(0) = \frac{1}{N_{tot}}\left[\frac{(1-E_1)^2 f_1 + (1-E_2)^2 f_2 + (1-E_3)^2(1-f_1-f_2)}{[(1-E_1)f_1 + (1-E_2)f_2 + (1-E_3)(1-f_1-f_2)]^2}\right] \tag{3.9}$$

$$G_{RR}(0) = \frac{1}{N_{tot}}\left[\frac{\gamma_1{}^2 f_1 + \gamma_2{}^2 f_2 + \gamma_3{}^2(1-f_1-f_2)}{[\gamma_1 f_1 + \gamma_2 f_2 + \gamma_3(1-f_1-f_2)]^2}\right] \tag{3.10}$$

$$G_{GR}(0) = \frac{1}{N_{tot}}\left[\frac{(1-E_1)\gamma_1 f_1 + (1-E_2)\gamma_2 f_2 + (1-E_3)\gamma_3(1-f_1-f_2)}{[(1-E_1)f_1 + (1-E_2)f_2 + (1-E_3)(1-f_1-f_2)][\gamma_1 f_1 + \gamma_2 f_2 + \gamma_3(1-f_1-f_2)]}\right] \tag{3.11}$$

3.3. Materials and Methods

3.3.1. Sample Preparation/Peptide Labeling

Synthetic peptide with the sequence Gly-$(Pro)_{15}$-Cys was purchased from Sigma Genosys (St. Louis, MO). The amino terminal glycine and carboxyl terminal cysteine were positioned to allow conjugation of reactive fluorescent dyes to the respective sites. Maleimide reactive dyes were used for the cysteine, and succinimidyl ester reactive dyes were used for the amino terminus.

The first step in labeling was to react the cysteine site with a maleimide reactive dye. First, 0.3 mg of peptide was dissolved in 250 μL of 50 mM sodium phosphate buffer at pH 7.2. A five fold molar excess of TCEP was added to the peptide solution and allowed to stir for 5 minutes. Then 1 mg of Texas Red maleimide (Invitrogen Corp., Carlsbad, CA) or Atto 740 maleimide (Atto-TEC GmbH, Siegen, Germany) was dissolved in 250 μL of DMSO. The dissolved dye was added drop-wise to the stirring peptide/TCEP solution. The reaction was allowed to proceed for 90 minutes after which the unreacted dye was separated from the labeled peptide using a Superdex Peptide HR 10/30 size exclusion column (GE Healthcare Life Sciences, Piscataway, NJ) with 20 mM pH 7.5 sodium bicarbonate buffer as the mobile phase flowing at 0.25 mL/min. The column was used on the HPLC system described previously in Chapter 2. The separations were monitored at 220 nm (for the peptide backbone) and at a wavelength appropriate for the reacted dye (593 nm for Texas Red and 700 nm for Atto 740). Ideally Atto 740 would be monitored at its peak absorption of 740 nm but the upper range on the UV-Vis

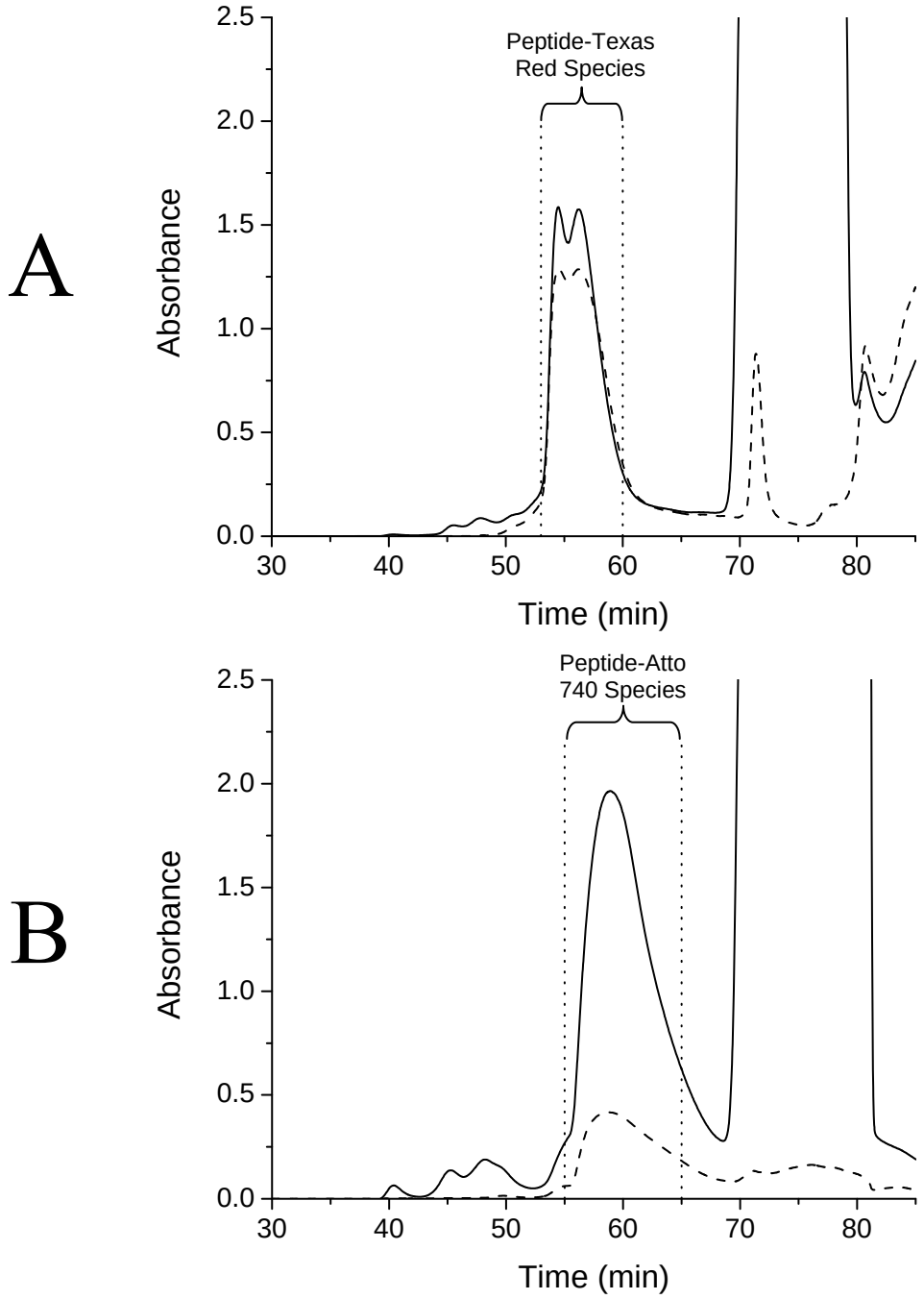

Figure 3.1: (A) Separation of polyproline labeled with Texas Red maleimide monitored at 593 nm (dashed line) from unlabeled polyproline monitored at 220 nm (solid line) peak at 75 minutes. (B) Separation of polyproline labeled with Atto 740 maleimide monitored at 700 nm (dashed line) from unlabeled polyproline monitored at 220 nm (solid line) peak at 75 minutes.

detector was 700 nm. Figure 3.1 is an example chromatogram for each of the labelings. It was found that the hydrophobic dyes (Texas Red , Atto 740) tended to adsorb to the stationary phase and would not elute off with the buffer mobile phase. Both dyes required a 50% acetonitrile/50% H_2O wash to remove the residual dye from the column between separations.

The collected fractions were then concentrated to ~0.25 mM with a final volume of 400 μL through the use of a SpeedVac and dialyzed into 100 mM pH 7.5 sodium bicarbonate buffer. Reaction of the amino terminus was carried out using Alexa Fluor 488 succinimidyl ester (Invitrogen Corp. Carlsbad, CA) dissolved in 150 μL of DMSO and mixed with the dialyzed polyproline at room temperature for 90 minutes. Purification of the doubly labeled peptide was performed using the same separation method previously performed for the singly labeled species (Figure 3.2). If further purification was required, an H_2O/Acetonitrile gradient elution was performed using a C_{18} 4.6 mm x 250 mm, 5 μm particle size column (Vydac model 218TP4). The samples were concentrated through the use of a SpeedVac and finally dialyzed into 50 mM sodium phosphate pH 7.0 buffer. Dye labeling was verified via mass spectrometry and UV-Vis absorbance measurements (results not shown).

3.3.2. FCS Setup

The FCS system was arranged with the dual channel/two pinhole setup and aligned as described in Chapter 2.1.3 using a 60x water immersion objective (UPLSAPO 60XW, Olympus, Center Valley, PA). For the polyproline-Alexa Fluor

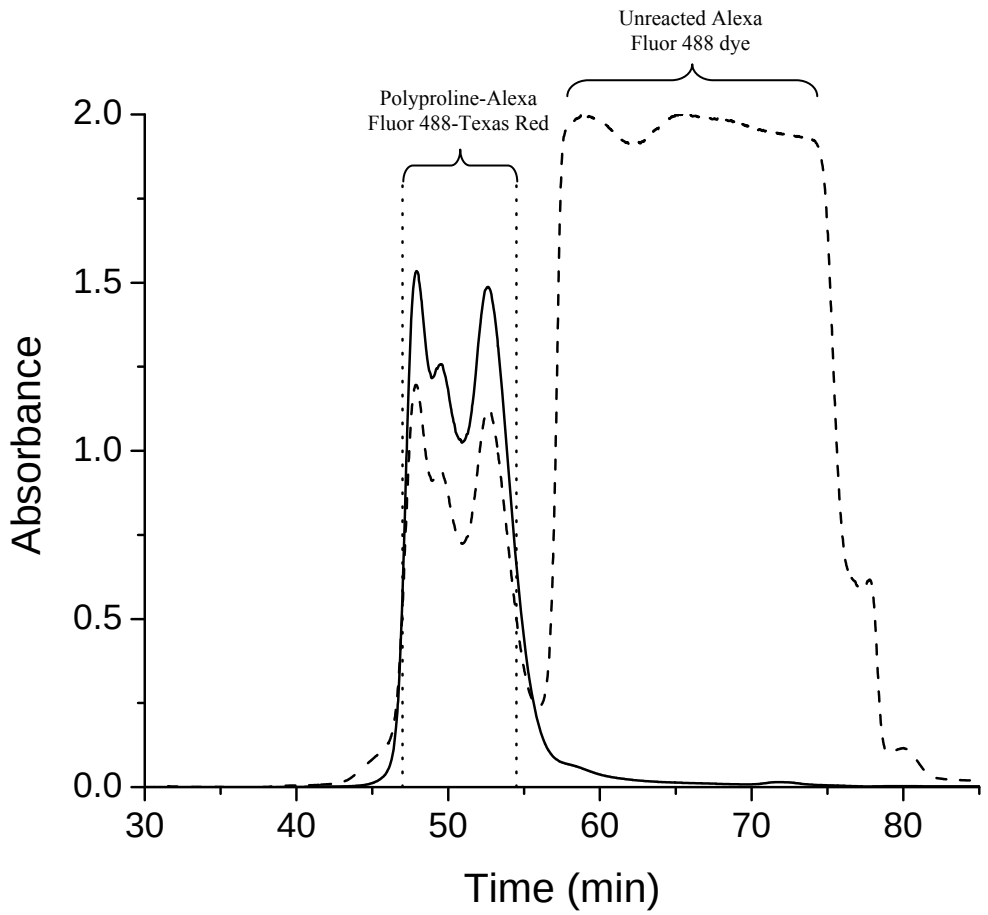

Figure 3.2: Separation of polyproline-Alexa Fluor 488-Texas Red from unreacted Alexa Fluor 488 dye. Texas Red was monitored at 593 nm (solid line) and Alexa Fluor 488 was monitored at 493 nm (dashed line).

488-Texas Red sample, the optical filters (all from Chroma, Rockingham, VT) used included the microscope dichroic (500DCXR), FRET dichroic (565DCLP), donor emission filter (HQ535/50M), and the acceptor emission filter (HQ620/75M). The only change when measuring the polyproline-Alexa Fluor 488-Atto 740 sample was the acceptor emission filter, which was changed to an HQ667/LP. Data were collected in photon mode and software-correlated with afterpulsing correction. The results were fit using Origin (Origin Labs) or Excel (Microsoft).

3.4. Fluorescence Lifetime/Anisotropy Measurements

To measure the distribution of FRET efficiencies in labeled polyproline samples the fluorescence lifetime of the donor (Alexa Fluor 488) was measured using the TCSPC system described previously. The system was tuned to 940 nm, then frequency doubled to 470 nm. Data were collected using a laser power of 750 nW for the donor-only peptide and 9.0 μW for the double labeled peptide sample with the single-pass monochromator set to monitor the emission at 510 nm. The lifetime of a sample of donor-only labeled polyproline was measured along with the polyproline-Alexa Fluor 488-Texas Red sample. The donor-only species was fit using a single discrete lifetime (Figure 3.3). The FRET-pair labeled peptide lifetime was fit using two methods. The first fitting method involved the use of 3 discrete exponential components with the results shown in Figure 3.4A. The second fitting method used the maximum entropy algorithm [14,15] for fitting as described in Unruh *et al*.[16] The results for the fit are shown in Figure 3.4B, where each peak represents a

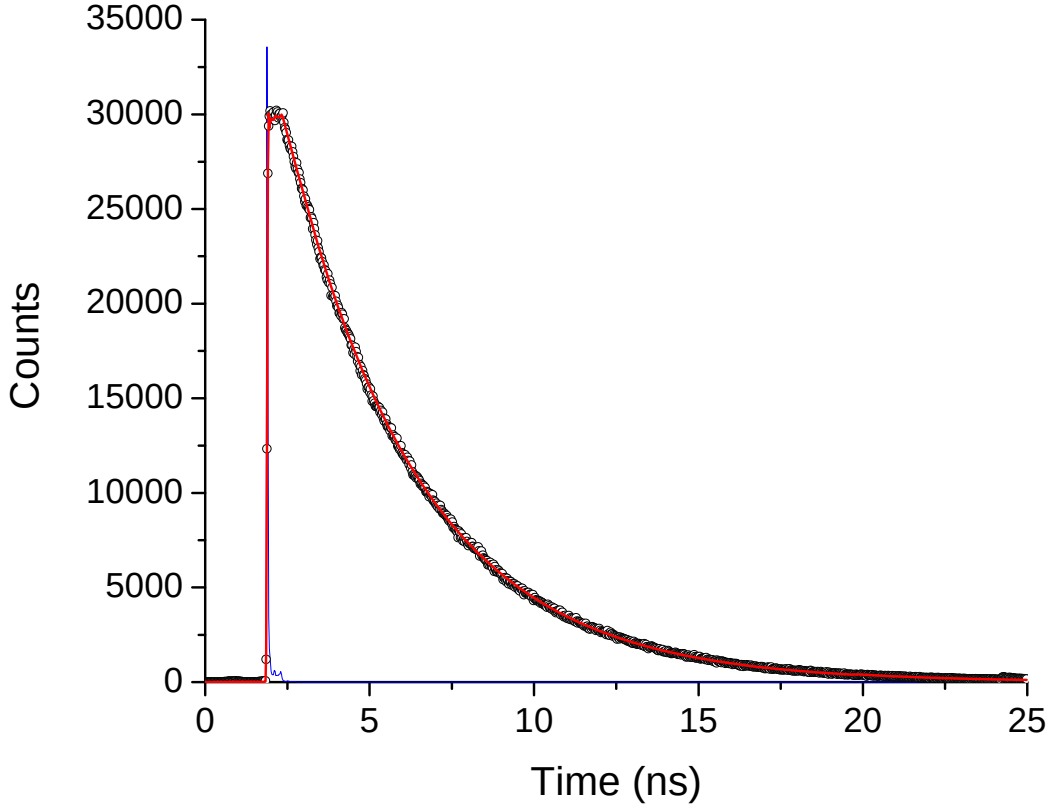

Figure 3.3: TCSPC fluorescence lifetime measurement (open circles), instrument response function (blue line), and fit (red line) of Alexa Fluor 488 only polyproline sample to a single exponential lifetime of 3.98 ± 0.02 ns.

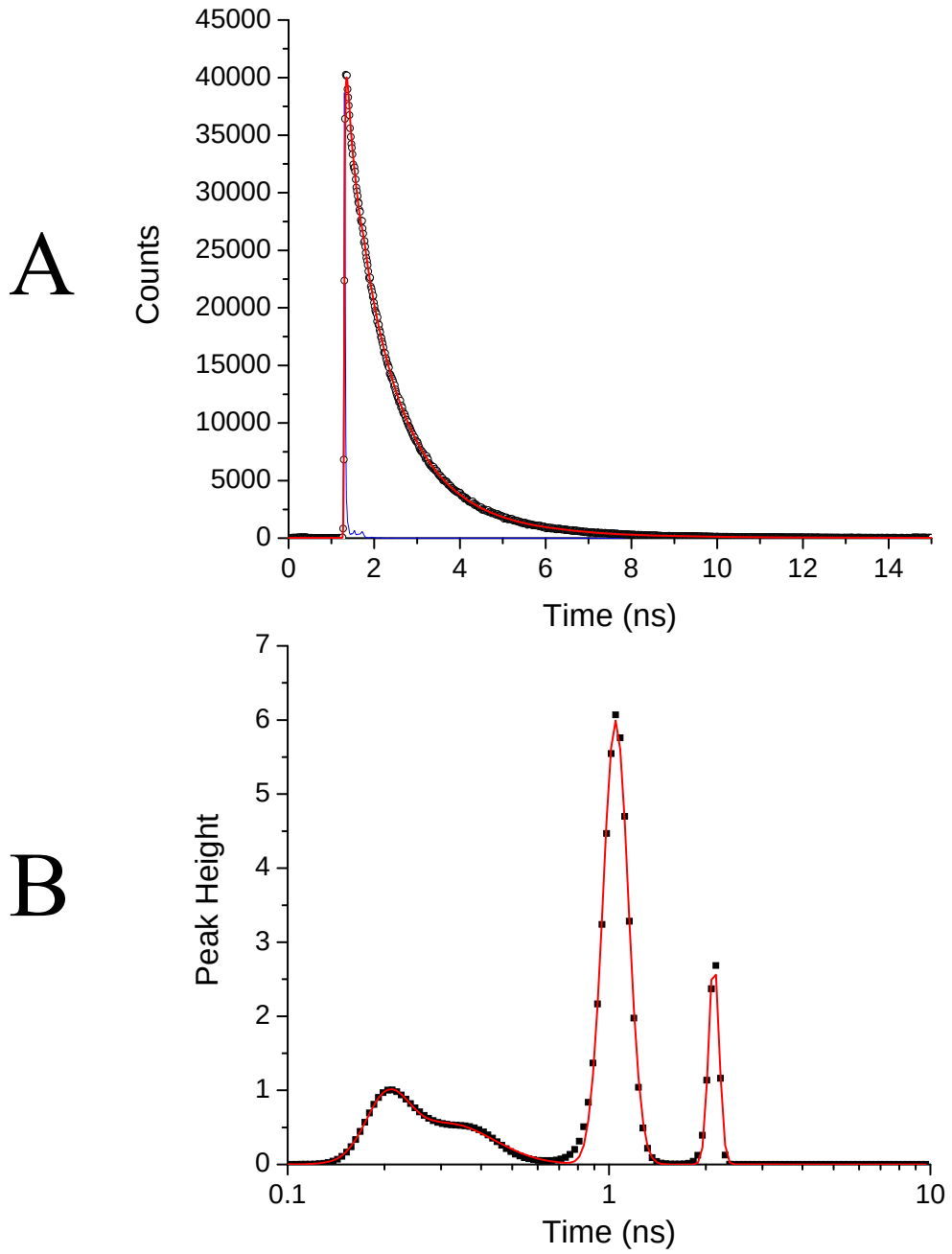

Figure 3.4: (A) Discrete lifetime fit (red line) to Polyproline-Alexa Fluor 488-Texas Red data (open circles) along with the IRF (blue line). (B) MEM fit (black squares) to the same data set as A. A Gaussian fit was performed on the MEM results (red line) to produce the lifetimes for each peak.

contribution to the fluorescence decay with the underlying decay time constants. The lifetime fit to the polyproline AF488-Texas Red sample resulted in three discrete lifetimes (four using the MEM algorithm). Table 3.1 shows the values for the lifetimes and fractions for each component from the discrete and maximum entropy (MEM) fits.

The anisotropy of the Alexa Fluor 488 dye attached to polyproline was also measured to check for dye mobility. If the dye sticks to the polyproline, it could lead to a κ^2 value other than the value of two-thirds that is generally assumed for FRET measurements. Free Alexa Fluor 488 dye in 50 mM sodium phosphate pH 7.0 buffer was used for the measurement of the g-factor as defined in Chapter 2.5.2. The anisotropy data was globally fit to discrete rotational correlation times using the parallel and perpendicular data (Figure 3.5).

The anisotropy of the Texas Red dye attached to polyproline was measured using the photonic crystal fiber to produce the necessary excitation wavelength. A 594/10x (Chroma, Rockingham, VT) excitation filter was placed after the output of the crystal fiber to filter out the unwanted wavelengths. The emission was monitored with the monochromator set to 615 nm. The polyproline-Texas Red lifetime was first measured at the magic angle and fit using a single discrete lifetime (Figure 3.6). The g-factor was determined using free Texas Red dye in buffer. The anisotropy was then collected and fit in the same manner as the Alexa Fluor 488 data (Figure 3.7).

Table 3.2 presents the results of the FRET efficiencies calculated from the lifetime fits. While the MEM fits resulted in four FRET efficiencies vs. the three for

Table 3.1: TCSPC lifetimes and fractions calculated for polyproline Alexa Fluor 488-Texas Red using two fitting methods. Uncertainties calculated using the method of support plane analysis.

Discrete Fit		MEM Fit	
Lifetime (ns)	Fraction	Lifetime (ns)	Fraction
2.0 ± 0.2	0.15 ± 0.01	2.120 ± 0.007	0.11 ± 0.01
0.95 ± 0.08	0.56 ± 0.03	1.049 ± 0.002	0.58 ± 0.06
0.17 ± 0.04	0.29 ± 0.02	0.32 ± 0.05	0.19 ± 0.06
		0.20 ± 0.01	0.13 ± 0.06

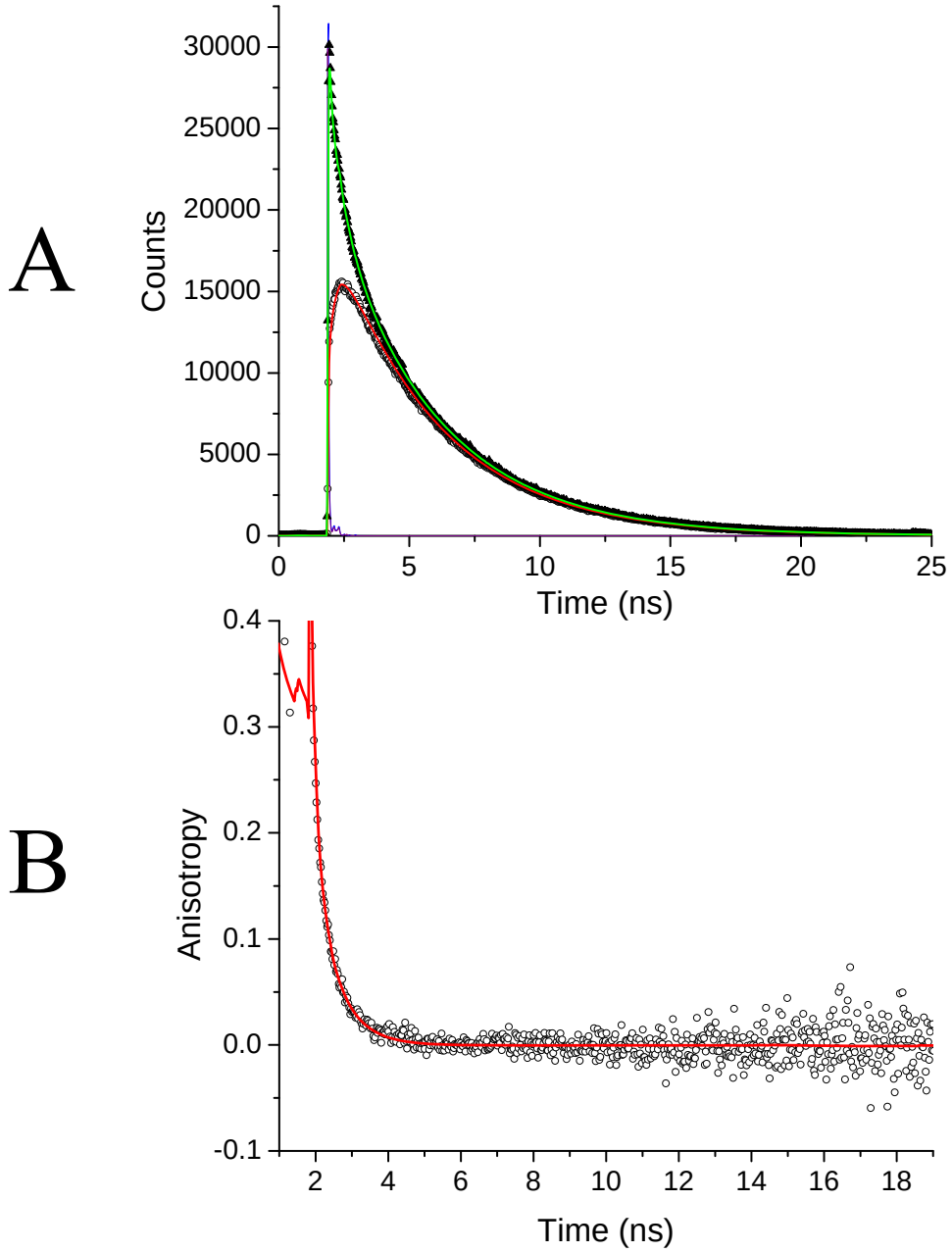

Figure 3.5: (A) Parallel (green line) and perpendicular (red line) fits to polyproline-Alexa Fluor 488 parallel (closed triangles) and perpendicular (open circles) anisotropy data. (B) Calculated anisotropy decay from the collected data (open circles) and the resulting fit (red line) using the parameters from A (g-factor = 0.948, r_0 = 0.38, ϕ_1 = 0.17±0.09 ns with a fraction of 0.6 ± 0.2 and ϕ_2 = 0.7 ± 0.3 ns).

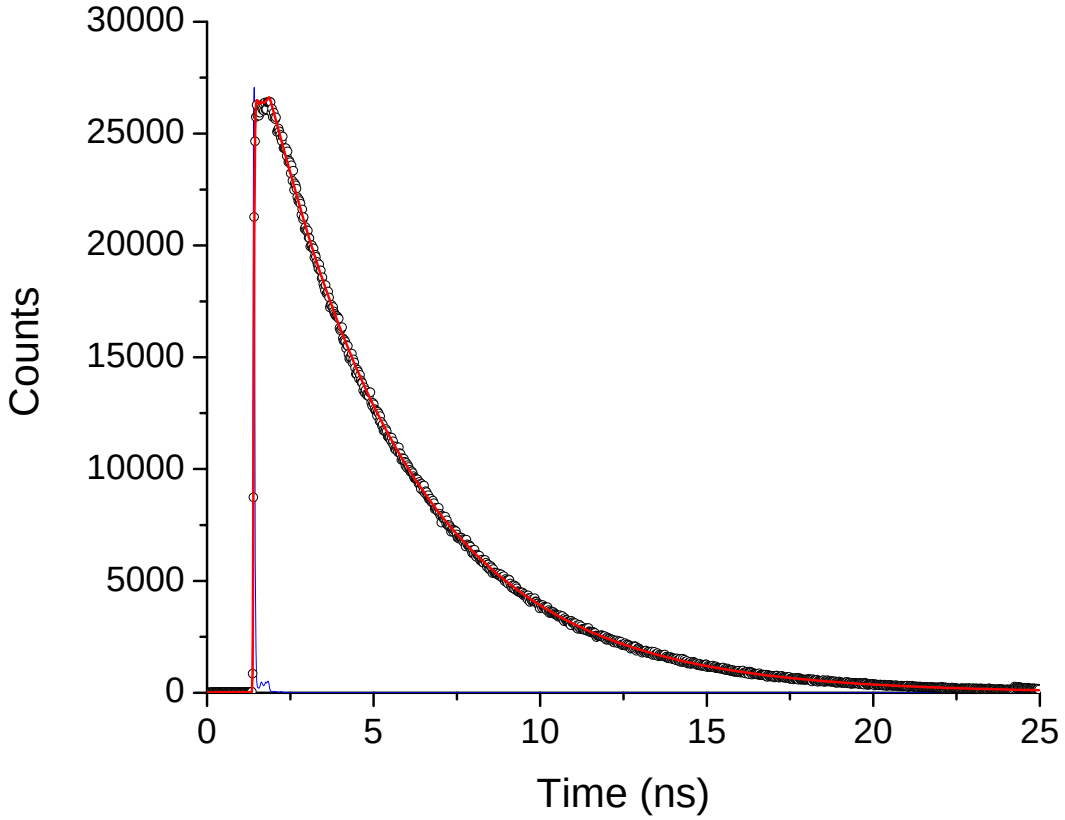

Figure 3.6: TCSPC fluorescence lifetime measurement (open circles), instrument response function (blue line), and fit (red line) of Texas Red bound to polyproline. The fit was to a single exponential lifetime of 4.21 ± 0.01 ns.

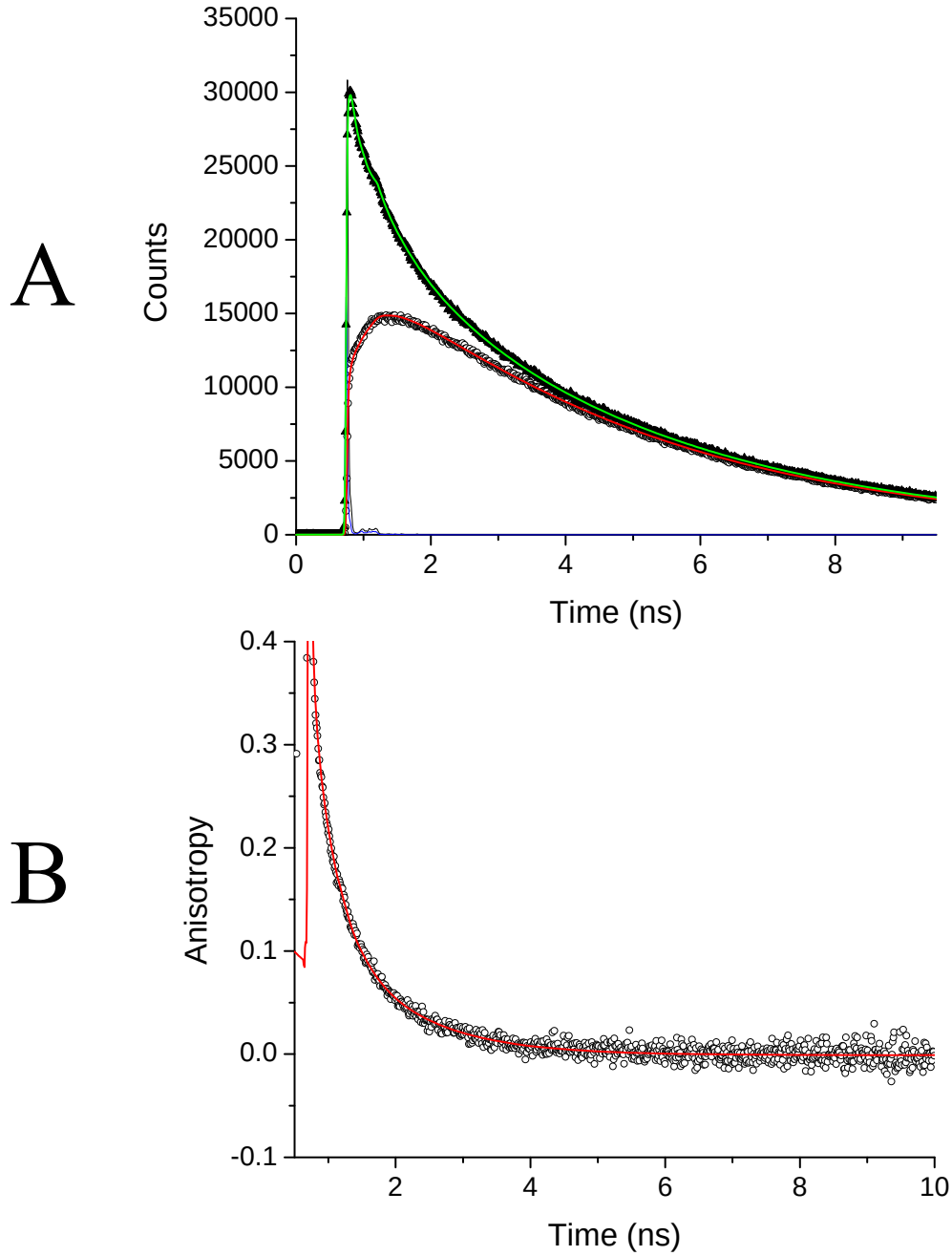

Figure 3.7: (A) Parallel (green line) and perpendicular (red line) fits to polyproline-Texas Red parallel (closed triangles) and perpendicular (open circles) anisotropy data. (B) Calculated anisotropy decay from the collected data (open circles) and the resulting fit (red line) using the parameters from A (g-factor = 0.957, r_0 = 0.38, ϕ_1 = 0.27±0.05 ns with a fraction of 0.62 ± 0.09 and ϕ_2 = 1.1 ± 0.2 ns).

Table 3.2: FRET efficiencies and fractions calculated from lifetime fits of polyproline Alexa Fluor 488-Texas Red using the two fitting methods.

Discrete Fit		MEM Fit	
FRET Efficiency	Fraction	FRET Efficiency	Fraction
0.51 ± 0.05	0.15 ± 0.01	0.467 ± 0.004	0.11 ± 0.01
0.76 ± 0.02	0.56 ± 0.03	0.735 ± 0.002	0.58 ± 0.06
0.96 ± 0.01	0.29 ± 0.02	0.92 ± 0.01	0.19 ± 0.06
		0.947 ± 0.002	0.13 ± 0.06

discrete fitting, the two methods produced very similar results, demonstrating multiple FRET states for polyproline. The presence of multiple conformations in polyproline has been shown previously.[12,17,18] Polyproline is known to isomerize from the all *trans* form to single or multiple *cis* conformations in the peptide. Each of these *cis* conformations introduces a bend in the peptide backbone leading to a higher FRET efficiency. The transition between these states has been shown to be very long (seconds to minutes) compared to the FCS timescale.[18]

The anisotropy data for the two dyes show two rotational correlation times for each. The fast components for both Alexa Fluor 488 and Texas Red anisotropies (170 ps and 270 ps) are very similar to the free dye rotational correlation time and in both cases make up about 60% of the decay. The longer rotational correlation time could either be from the dye sticking to the peptide or from a motion in a cone behavior. The motion in a cone model assumes a cone with a half angle θ, in which the local motion is assumed to be free but outside of which the potential rises to infinity. Both models restrict the reorientation of the dye resulting in κ^2 values other than two-thirds. It is possible that the long rotational correlation time would give rise to a κ^2 value different from the rotationally averaged value.

3.5. Fluorescence Correlation Spectroscopy

To decrease adsorption of polyproline onto the surface of the glass coverslips used, they were pretreated with bovine serum albumin (BSA) using the following procedure. A 5 mg/mL solution of BSA was prepared using ultrapure water. Then

50 μL of the solution was spread over the surface of a coverslip, allowed to sit for 5 minutes, and then dried with a stream of N_2. The slide was then placed on the microscope for immediate use (keeping the treated side up), then about 30 μL of a 5 nM solution of the peptide in 50 mM sodium phosphate pH 7.0 buffer was placed on the coverslip. The laser power was adjusted to 10 μW and the focus positioned 20 μm above the surface of the coverslip. The resulting photon stream was collected for ~5 minutes. After calculating the four correlations, the data were first fit globally using equation 1.12.

The initial amplitudes were allowed to vary independently, while linking the transit times (τ_d). The two autocorrelations contained a unique triplet fraction (f) and triplet time (τ_t) while the cross-correlations did not include a triplet component. The triplet components were not linked because the triplet parameters are unique for each dye and will only affect the autocorrelation of that dye. Unless otherwise stated the axial-radial ratio (p) in all of the fits was fixed to a value of eight. Figure 3.8A contains the correlations and the resulting fit and Table 3.3 contains the best fit parameters. The values 2.5 ± 0.2, 3.7 ± 0.4, and 6.1 ± 0.6 in Table 3.3 are the reciprocals of the initial amplitudes as measured by the individual correlation functions.

The correlations were also normalized (Figure 3.8B) to visually demonstrate the similarities in the curves. The normalization was performed by first dividing out the triplet contributions from the data for the two autocorrelations, and then using the initial amplitudes from the global fit to scale all of the correlations to the same initial

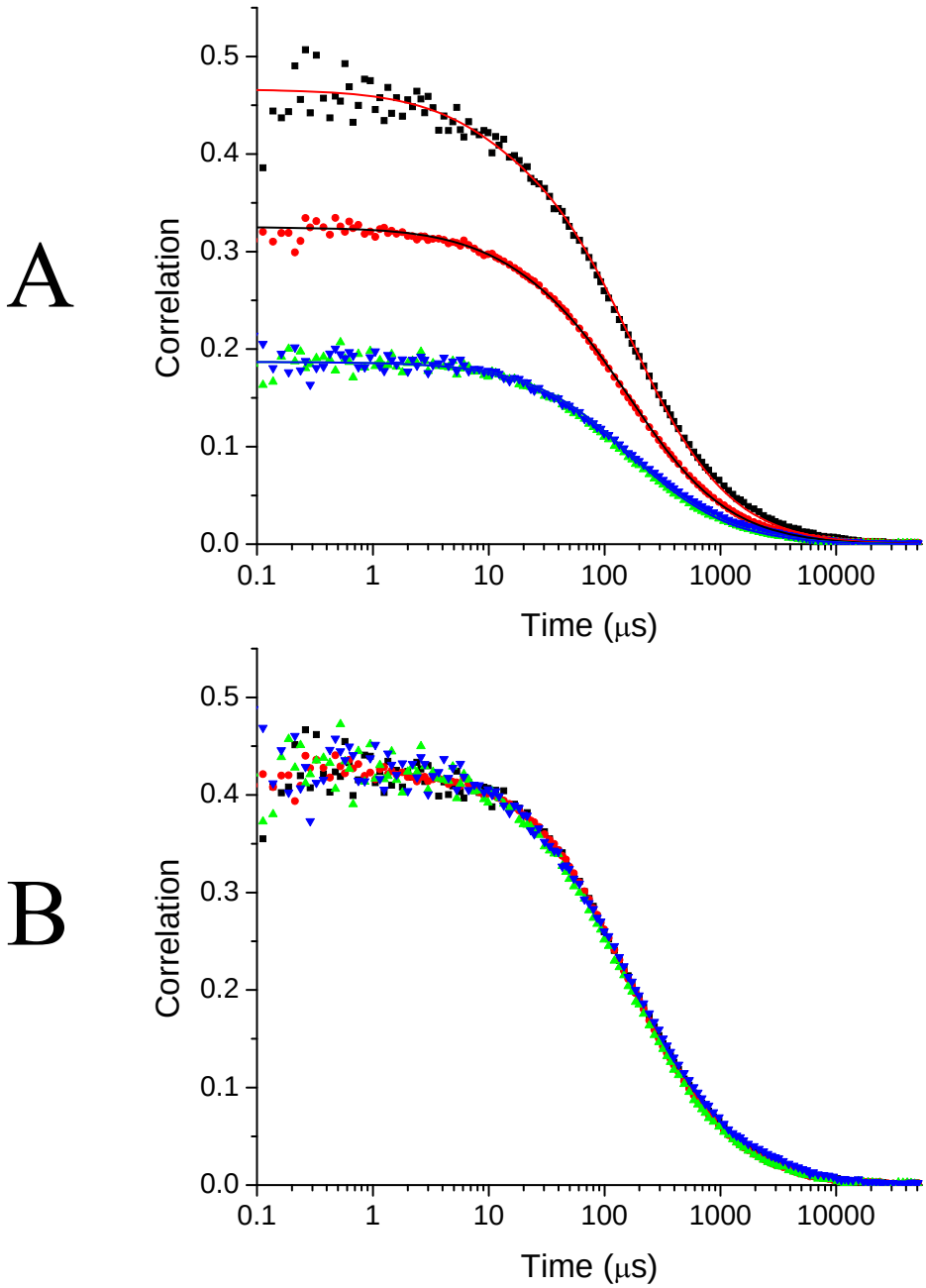

Figure 3.8 (A) Global fit (solid lines) result for polyproline-Alexa Fluor 488-Texas Red. The transit times are linked and the initial amplitudes are allowed to vary independently. Unless noted otherwise $G_{GG}(\tau)$, $G_{RR}(\tau)$, $G_{GR}(\tau)$, and $G_{RG}(\tau)$ are represented by black squares, red circles, green triangles, and blue inverted triangles respectively. (B) Overlay of the normalized correlations demonstrating good overlap of all four correlations.

Table 3.3: Global fit parameters for polyproline-AF488-Texas Red averaged from different days. The initial amplitudes were allowed to vary independently. The parameters τ_{t1} and f_{t1} are the triplet time and fraction for the donor autocorrelation, τ_{t2} and f_{t2} are the triplet time and fraction for the acceptor autocorrelation.

Parameter	Average from 3 days
f_{t1}	0.08 ± 0.02
τ_{t1} (μs)	11 ± 6
f_{t2}	0.07 ± 0.02
τ_{t2}(μs)	19 ± 2
N_{GG} (apparent)	2.5 ± 0.2
N_{RR} (apparent)	3.7 ± 0.4
N_{GR} and N_{RG} (apparent)	6.1 ± 0.6
τ_D (μs)	158 ± 10
p (fixed)	8

amplitude. If there were fluctuations in the FRET efficiency on the microsecond to millisecond timescale, then two extra features would be present. First, each of the autocorrelations would have an additional decay component due to another source of fluctuations in the fluorescence signal. Second, the cross-correlations would contain a rise component due to the anti-correlated nature of FRET fluctuations between the two channels. FRET fluctuations would therefore result in the curves not overlapping as they do in Figure 3.8B.

After developing equations 3.9-3.11, they were verified for a three-state FRET system in SimFCS using the FRET efficiencies and fractions determined from the TCSPC data. The simulation result is shown in Figure 3.9 and the fit parameters given in Table 3.4. The values obtained from the fit of the simulation are in excellent agreement with the FRET efficiencies used in the simulation, validating the ability of the functions to fit multiple FRET states.

Equations 3.9-3.11 were then employed in a global fit using the FRET efficiencies and fractions obtained from the TCSPC measurements as the initial guess and linking all of the variables (except the triplet fractions) across the four correlations as performed previously in Figure 3.8A. Upon examination of the fitting functions it can be seen that the correlations provide only three unique initial amplitudes for each data set (one for $G_{GG}(0)$, $G_{RR}(0)$, and $G_{GR/RG}(0)$). With three initial amplitudes, it is only possible to fit three variables that affect the initial amplitude to a unique solution. For a three-state FRET system, the variables that affect the initial amplitude include N_{tot}, E_1, f_1, E_2, f_2, and E_3. One of the variables

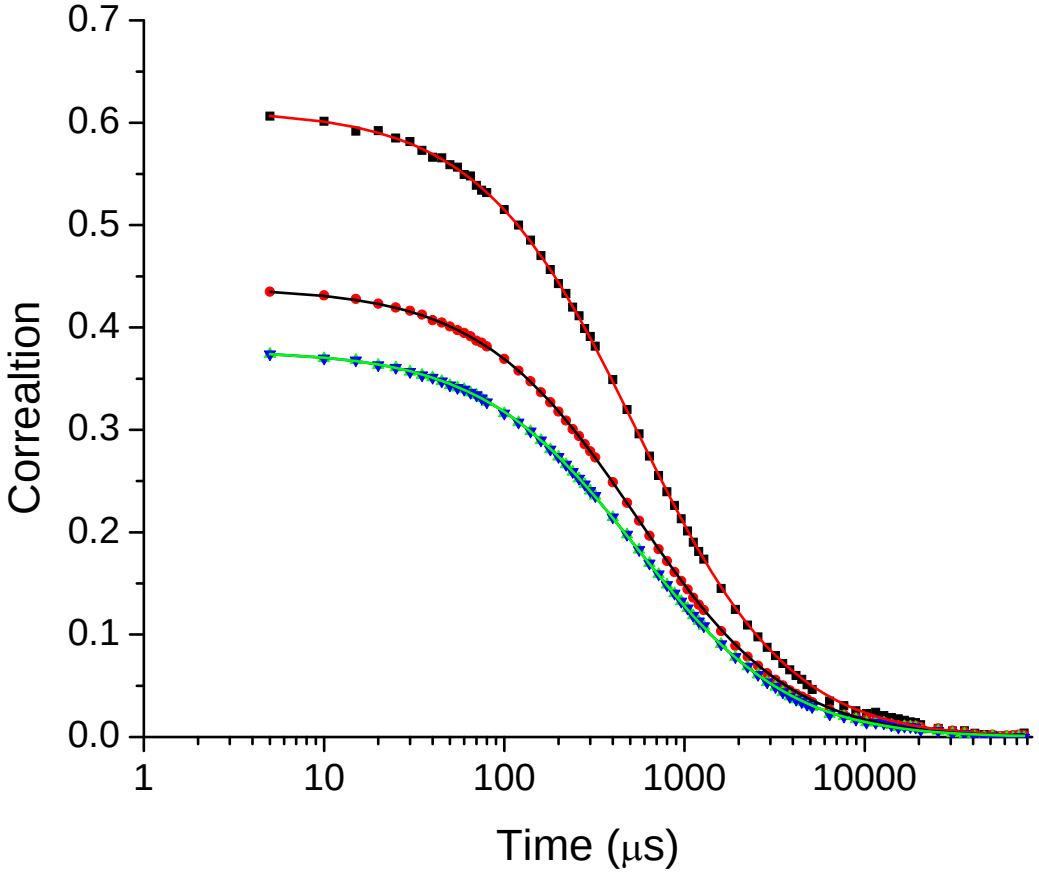

Figure 3.9: Global fit of SimFCS simulation using the 3 FRET efficiencies and fractions from the TCSPC data for the input parameters of the simulation.

Table 3.4: Fit parameters to SimFCS simulation shown in Figure 3.9. The E_2, f_2, and E_3 parameters were fixed to the values used in the simulation.

Fitting Parameter	Fit Values	Simulation Input Parameters
N_{tot}	2.346 ± 0.008	2.35
τ_d (μs)	541 ± 5	544
p (fixed)	5	5
E_1	0.519 ± 0.007	0.51
f_1	0.13 ± 0.01	0.15
E_2 (fixed)	0.76	0.76
f_2 (fixed)	0.56	0.56
E_3 (fixed)	0.96	0.96
f_3 ($1-f_1-f_2$)	0.31 ± 0.01	0.29
β (fixed)	1	1
α (fixed)	0	0

determines the height of the initial amplitudes (N_{tot}) while the other two variables adjust the relative positions of the correlations. With this requirement the variables E_2, f_2, and E_3 were fixed to 0.76, 0.58, and 0.96, respectively, as given by the discrete lifetime fits. The results from this fit are shown in Figure 3.10 and the fit parameters given in Table 3.5. The values for E_1 and f_1 differed significantly from the TCSPC fit which led to further investigation to explain the discrepancy.

To better identify the fluorescent states that were being measured on the microscope, burst measurements of the polyproline sample were taken as described previously by Slaughter *et al.*[19] The concentration of polyproline was lowered to 200 pM and the laser power increased to 20 μW so that individual molecules could be measured as they diffused through the observation volume, allowing FRET efficiencies to be calculated. The data was binned at 300 μs time resolution and all of the bins where the sum of the green and red channels was greater than fourteen were collected into an array of green and red counts. The FRET efficiencies were calculated using equation 1.7 with a cross-talk factor of 0.11 and a correction factor of 1.1. In typical burst measurements a minimum count in the red channel is required to ensure that all of the bins contain a green and red dye that are both photoactive. In FCS measurements however, this is not possible. Consequently, in order to reflect the signals detected in FCS, burst measurements with low acceptor counts were not rejected. The resulting histogram of the apparent FRET efficiencies is shown in Figure 3.11. A threshold was chosen at a FRET efficiency of 0.4 with the average E and fraction above and below the threshold calculated. The average efficiency below

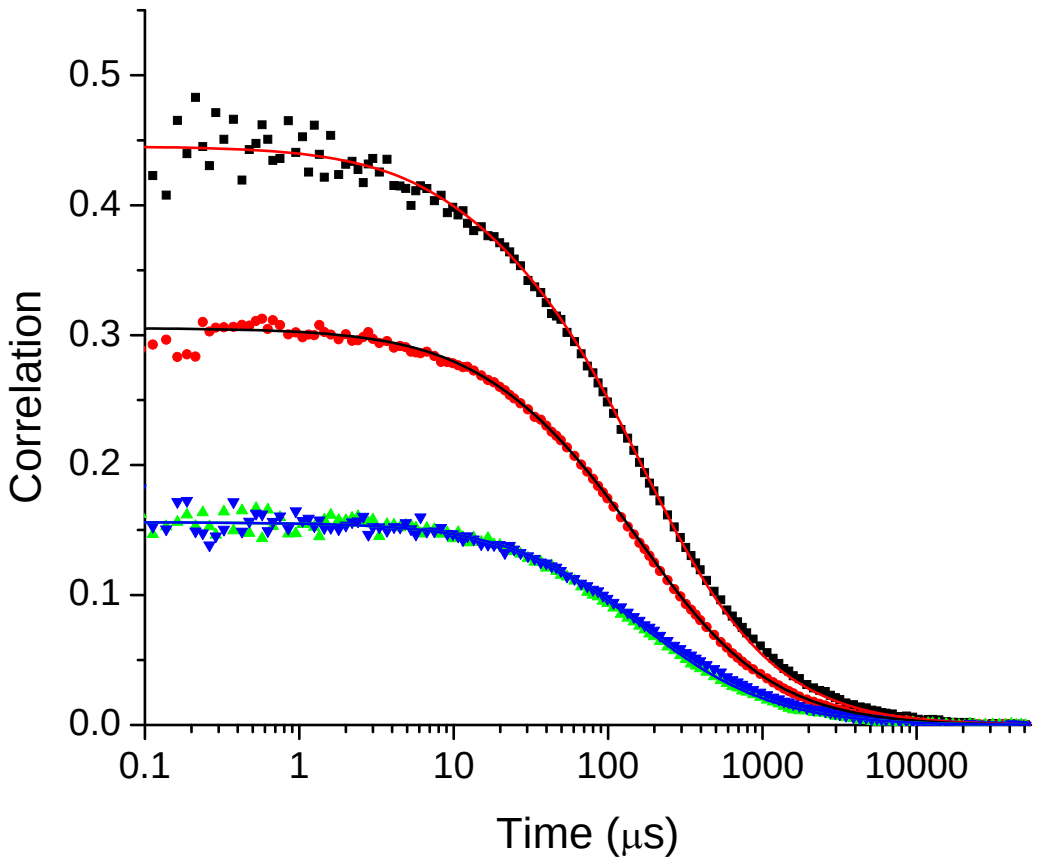

Figure 3.10: Global fit of polyrproline-AF488-Texas Red using three FRET efficiencies to describe the difference in initial amplitude.

Table 3.5: Fit parameters using 3 static FRET state model for polyproline-AF488-Texas Red while fixing E_2, f_2, and E_3. The triplet parameters were fixed the values given in Table 3.3.

Parameter	Average from 3 days
N_{tot}	4.2 ± 0.4
τ_d (μs)	158 ± 8
p (fixed)	8
E_1	0.16 ± 0.05
F_1	0.25 ± 0.04
E_2 (fixed)	0.76
f_2 (fixed)	0.56
E_3 (fixed)	0.96
f_3 ($1-f_1-f_2$)	0.19 ± 0.04
β (fixed)	0.91
α (fixed)	0.11

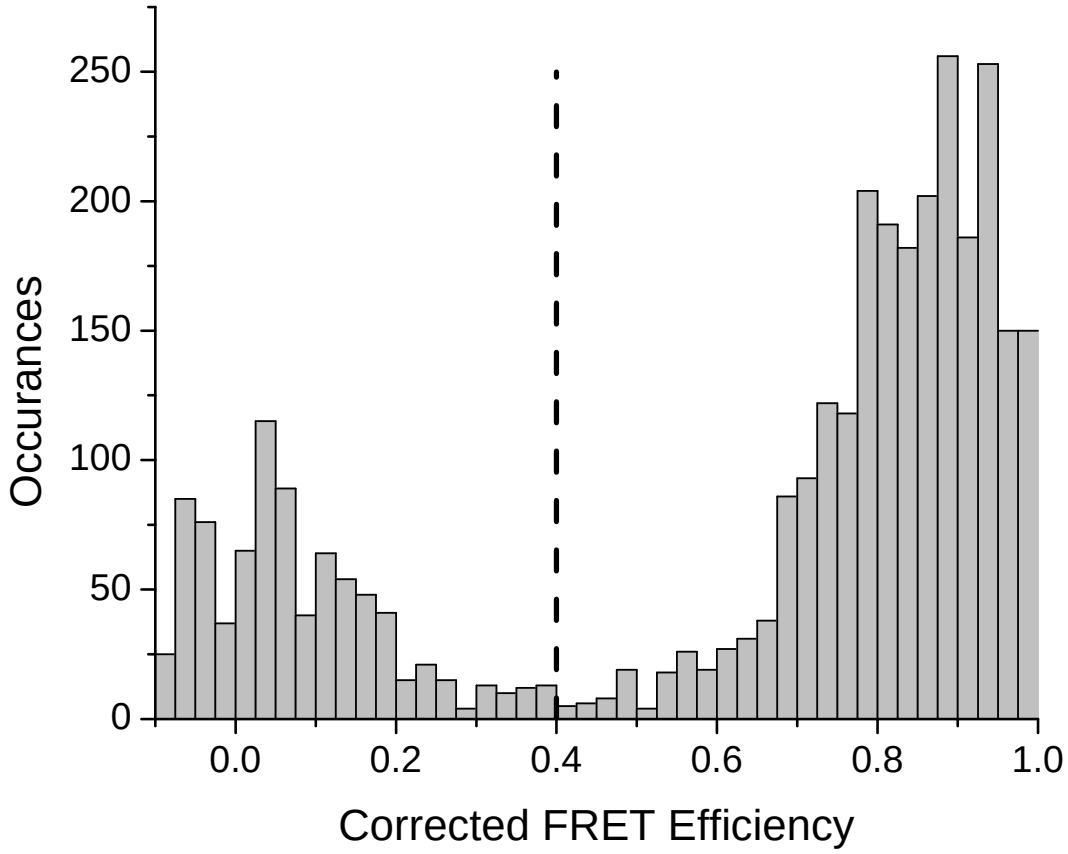

Figure 3.11: FRET efficiency distribution of polyproline-Alexa Fluor 488-Texas Red. The average E and fraction below (E_1, f_1) and above (E_2, f_2) the threshold level (dashed line) was calculated. $E_1 = 0.08$, $f_1 = 0.26$, $E_2 = 0.82$, and $f_2 = 0.74$.

the threshold (E_1) was 0.08 with a fraction of 0.26, and the average efficiency above the threshold E_2 was 0.82 with a fraction of 0.74

Using the values obtained from the burst measurements, the FCS data was fit using the two-state FRET equations 3.5-3.7. The parameter E_2 was fixed to 0.82 while N_{tot}, E_1, and f_1 were varied. The resulting fit values were $E_1 = 0.15 \pm 0.04$ and $f_1 = 0.26 \pm 0.06$, which are in close agreement to the values measured in the burst distributions.

The FRET efficiency distribution from the bursts was clearly different from what was predicted from the TCSPC fit. A possible explanation for the discrepancy is that the burst distribution cannot resolve the high FRET states (0.95, 0.76) resulting in an averaged FRET efficiency for those states. In the TCSPC fits those high FRET states accounted for 90% of the total population. The absence of the 0.51 FRET efficiency state could be a result of the low percent of the total population based on the TCSPC measurements, or the 0.51 FRET efficiency is possibly not a true FRET state but a donor quenched state that produces a lifetime that appears as a FRET efficiency of 0.51. The population with a very low apparent FRET efficiency that is in the burst distributions is most likely a result of the photobleaching of the acceptor molecule. Such molecules have a non-negligible probability that the same molecule re-enters the observation volume, yielding a fluorescence burst where the FRET state appears very low.

To check the value obtained for N_{tot} the photon streams from the two channels were combined and correlated to remove the effect of FRET on the initial amplitude

giving the true average number of molecules in the observation volume. The combined correlations were fit using a single diffusion time and a triplet component. The average total number of particles in the focal volume was then determined from the initial amplitude of the fit. Table 3.6 compares the N_{tot} values from the global fits to the values obtained in the combined photon stream correlation fits. The values of N_{tot} obtained from the global fit are in good agreement with the combined photon stream.

The same two-channel FCS measurements were planned using the polyproline-Alexa Fluor 488-Atto 740 labeled sample. It was expected that the average FRET efficiency would be lower due to the decrease in the R_0 for this FRET pair (34 Å) when compared to Alexa Fluor 488-Texas Red (52 Å). Due to the low quantum yield of the Atto 740 dye (~0.1) it was not possible to perform burst measurements on the sample to generate a distribution of FRET efficiencies. FCS measurements were carried out with the sample anyway. Figure 3.12 shows the correlations of the data and the resulting fit using the multiple static FRET state model. Table 3.7 contains the parameters for the fit shown in Figure 3.12. It is again clear that there are multiple FRET states with the Alexa Fluor 488-Atto740 labeled sample as would be expected. The changing of dyes used in the FRET pair should not affect the presence of multiple FRET states but only change the average FRET efficiency.

Table 3.6: Comparison of N_{tot} values obtained from global correlation fits and combined photon stream correlation fits.

Data set #	1	2	3
N_{tot} from global fits	4.14 ± 0.03	3.77 ± 0.03	4.63 ± 0.03
N_{tot} from combined stream	4.1 ± 0.1	3.8 ± 0.2	4.6 ± 0.2

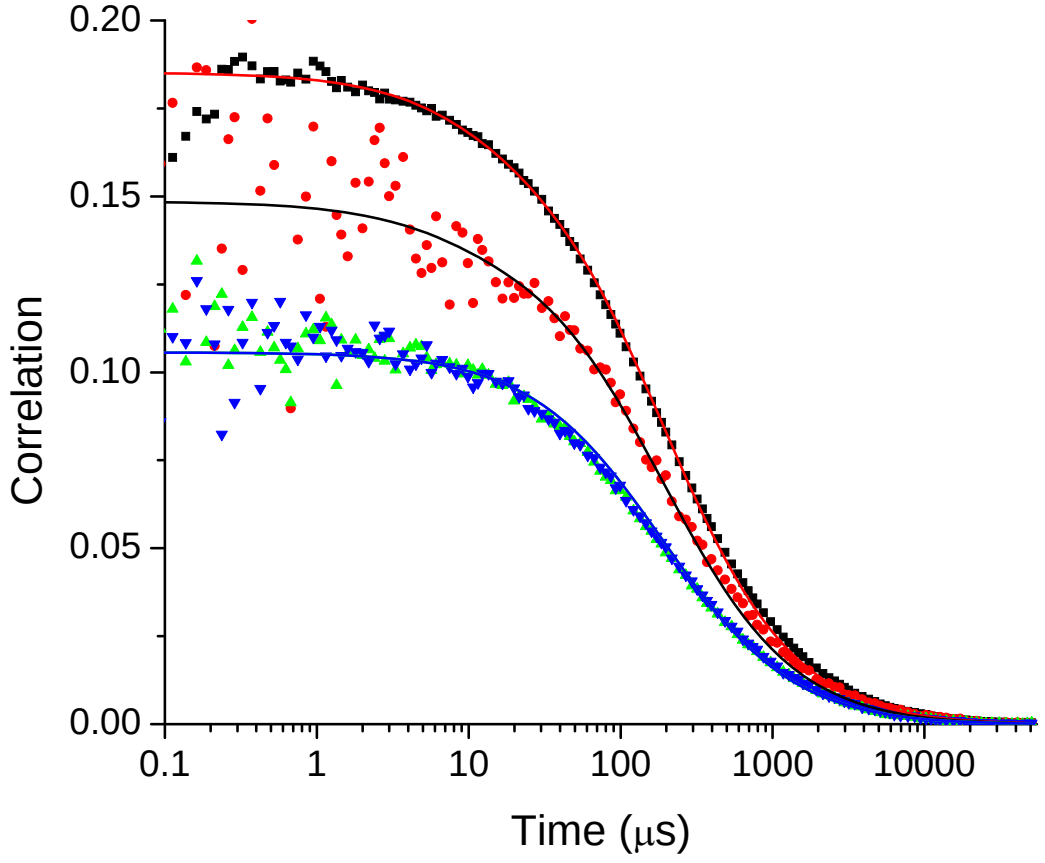

Figure 3.12: Correlations and resulting fit for polyproline-Alexa Fluor 488-Atto 740.

Table 3.7: Fitting parameters for polyproline Alexa Fluor 488-Atto 740.

Parameter	Value
f_{t1}	0.07
τ_{t1} (μs)	10
f_{t2}	0.06
τ_{t2}(μs)	6.7
N_{tot}	7.81
τ_d (μs)	188
P (fixed)	8
E_1	0.89
f_1	0.36
E_2	0.27
f_2 (1-f_1)	0.64
β (fixed)	0.3
α (fixed)	0.1

3.6. Conclusions

This chapter presents a global fitting approach for treating FCS FRET data using a homebuilt two-channel confocal microscope system. Two-channel FRET measurements were performed on a 15-mer polyproline peptide labeled with AlexaFluor 488 and Texas Red to investigate the effect that static FRET states (on the FCS timescale) had on the auto- and cross-correlations of the data. The dramatic difference between the values for the initial amplitudes of the correlations led to an investigation to explain the cause of the differences. The sample was known to be only donor-acceptor labeled peptide as determined through mass spectrometry and absorbance measurements, so a difference in concentration of the different fluorophores was not the cause for the difference in initial amplitudes.

When the correlations were scaled as shown in Figure 3.8B, it was visibly apparent that no FRET dynamics were occuring on the timescale of the measurements. The high quality of the fits when using only triplet and diffusional terms (Figure 3.8A) indicated the absence of any FRET dynamics on the correlations timescale.

Simulations were performed containing three static FRET states and fit to equations 3.8-3.10. The correlations fit very well to the input values used for the simulation demonstrating the validity of the derived equations. If the presence of multiple FRET states was included in fitting of the polyproline data using equations 3.8-3.10, the difference in initial amplitudes were well fit. It should be noted that although using multiple FRET states accurately describes the differences in initial amplitudes, the uncertainty in the value and fraction of the FRET states is high if all

parameters are allowed to vary due to the under determination of the initial amplitudes. If two FRET efficiencies were fixed to those obtained through the discrete fits of the TCSPC measurements (0.76 and 0.96) the third FRET efficiency drops to 0.16 with a fraction of 0.25, much different than the TCSPC fits. The fitting was greatly improved through the use of FRET efficiency distributions from burst measurements with a two state FRET system. The photobleaching of the acceptor leads to a very low apparent FRET state in the FCS correlations that cannot be filtered out as is typically done in burst measurements.

This formal treatment of multiple FRET states and the effect that those have on FCS measurements has not been seen in the literature. While this treatment provides an explanation for the differences in initial amplitudes it is not suited for the determination of the values for all of the FRET states as the parameters in the fit are overdetermined. There are three intial amplitudes and in the case of three FRET states there are six variables affecting the intial amplitudes resulting in multiple parameter combinations that will fit the data if all are allowed to vary.

3.7. References

1. Hom, E. F. Y., and Verkman, A. S., *Analysis of Coupled Bimolecular Reaction Kinetics and Diffusion by Two-Color Fluorescence Correlation Spectroscopy: Enhanced Resolution of Kinetics by Resonance Energy Transfer*. Biophys. J., **2002**. 83(1): p. 533-546.

2. Margittai, M., Widengren, J., Schweinberger, E., Schroder, G. F., Felekyan, S., Haustein, E., Konig, M., Fasshauer, D., Grubmuller, H., Jahn, R., and Seidel, C. A. M., *Single-Molecule Fluorescence Resonance Energy Transfer Reveals a Dynamic Equilibrium between Closed and Open Conformations of Syntaxin 1*. Proc. Natl. Acad. Sci. U.S.A., **2003**. 100(26): p. 15516-15521.

3. Slaughter, B. D., Allen, M. W., Unruh, J. R., Urbauer, R. J. B., and Johnson, C. K., *Single-Molecule Resonance Energy Transfer and Fluorescence Correlation Spectroscopy of Calmodulin in Solution.* J. Phys. Chem. B, **2004**. 108(29): p. 10388-10397.

4. Kapanidis, A. N., Lee, N. K., Laurence, T. A., Doose, S., Margeat, E., and Weiss, S., *Fluorescence-Aided Molecule Sorting: Analysis of Structure and Interactions by Alternating-Laser Excitation of Single Molecules*. Proc. Natl. Acad. Sci. U.S.A., **2004**. 101(24): p. 8936-8941.

5. Eggeling, C., Kask, P., Winkler, D., and Jager, S., *Rapid Analysis of Forster Resonance Energy Transfer by Two-Color Global Fluorescence Correlation Spectroscopy: Trypsin Proteinase Reaction*. Biophys. J., **2005**. 89(1): p. 605-618.

6. Müller, B. K., Zaychikov, E., Brauchle, C., and Lamb, D. C., *Pulsed Interleaved Excitation*. Biophys. J., **2005**. 89(5): p. 3508-3522.

7. Rüttinger, S., Macdonald, R., Kramer, B., Koberling, F., Roos, M., and Hildt, E., *Accurate Single-Pair Forster Resonant Energy Transfer through Combination of Pulsed Interleaved Excitation, Time Correlated Single-Photon Counting, and Fluorescence Correlation Spectroscopy*. J Biomed Opt, **2006**. 11(2): p. 024012.

8. Torres, T., and Levitus, M., *Measuring Conformational Dynamics: A New FCS-FRET Approach*. J. Phys. Chem. B, **2007**. 111(25): p. 7392-7400.

9. Nettels, D., Hoffmann, A., and Schuler, B., *Unfolded Protein and Peptide Dynamics Investigated with Single-Molecule FRET and Correlation Spectroscopy from Picoseconds to Seconds*. J. Phys. Chem. B, **2008**. 112(19): p. 6137-6146.

10. Schuler, B., Lipman, E. A., and Eaton, W. A., *Probing the Free-Energy Surface for Protein Folding with Single-Molecule Fluorescence Spectroscopy*. Nature, **2002**. 419: p. 743-747.

11. Schuler, B., Lipman, E. A., Steinbach, P. J., Kumke, M., and Eaton, W. A., *Polyproline and The "Spectroscopic Ruler" Revisited with Single-Molecule Fluorescence*. Proc. Natl. Acad. Sci. U.S.A., **2005**. 102(8): p. 2754-2759.

12. Doose, S., Neuweiler, H., Barsch, H., and Sauer, M., *Probing Polyproline Structure and Dynamics by Photoinduced Electron Transfer Provides Evidence for Deviations from a Regular Polyproline Type II Helix*. Proc. Natl. Acad. Sci. U.S.A., **2007**. 104(44): p. 17400-17405.

13. Eid, J. S., *Two-Photon Dual Channel Fluctuation Correlation Spectroscopy: Theory and Application* **2002** Department of Biophysics and Computational Biology, University of Illinois, Urbana-Champaign. 109 pp.

14. Livesey, A. K., and Brochon, J. C., *Analyzing the Distribution of Decay Constants in Pulse-Fluorometry Using the Maximum Entropy Method*. Biophys. J., **1987**. 52(5): p. 693-706.

15. Swaminathan, R., and Periasamy, N., *Analysis of Fluorescence Decay by the Maximum Entropy Method: Influence of Noise and Analysis Parameters on the Width of the Distribution of Lifetimes*. Proc. Indian Acad. Sci. Chem. Sci., **1996**. 108(1): p. 39-49.

16. Unruh, J. R., Liyanage, M. R., and Johnson, C. K., *Tyrosyl Rotamer Interconversion Rates and the Fluorescence Decays of N-Acetyltyrosinamide and Short Tyrosyl Peptides*. J. Phys. Chem. B, **2007**. 111(19): p. 5494-5502.

17. Best, R. B., Merchant, K. A., Gopich, I. V., Schuler, B., Bax, A., and Eaton, W. A., *Effect of Flexibility and Cis Residues in Single-Molecule FRET Studies of Polyproline*. Proc. Natl. Acad. Sci. U.S.A., **2007**. 104(48): p. 18964-18969.

18. Watkins, L. P., Chang, H. Y., and Yang, H., *Quantitative Single-Molecule Conformational Distributions: A Case Study with Poly-(L-Proline)*. J. Phys. Chem. A, **2006**. 110(15): p. 5191-5203.

19. Slaughter, B. D., Unruh, J. R., Allen, M. W., Urbauer, R. J. B., and Johnson, C. K., *Conformational Substates of Calmodulin Revealed by Single-Pair Fluorescence Resonance Energy Transfer: Influence of Solution Conditions and Oxidative Modification*. Biochemistry, **2005**. 44(10): p. 3694-3707.

4. CaM FRET FCS Dynamics

4.1. Introduction

The ability of calmodulin (CaM) to bind and activate such a wide variety of targets has led to much research on what gives CaM that capability.[1-6] As discussed in Chapter 1 CaM is able to adopt multiple conformations. It is believed that CaM's ability to bind such a wide range of targets stems from its flexibility and dynamics. Understanding the effect of Ca^{2+} binding on CaM conformational dynamics could be used to aid in a better understanding of CaM binding.

Several techniques have been used to measure the dynamics of CaM. Nuclear magnetic resonance (NMR) has been a popular method for many years using HSQC spectra to measure backbone dynamics.[5,7] These results have demonstrated an exchange rate of 2×10^4 s^{-1} for select residues as a result of Ca^{2+} binding. Another technique involved the use of a micromixer with a fluorescent probe to measure fast kinetics of Ca^{2+} binding. Two events were identified upon Ca^{2+} binding of ~490 μs and ~20 ms timescales that were proposed to be a result of conformational transitions of the C- and N-terminal domains of the protein.[8] Simulations also have been used to probe conformational dynamics of CaM, calculating a transition from a closed to open form of the N-terminus with a rate of 4×10^4 s^{-1} which compares well with the NMR measurement of 2×10^4 s^{-1} for the C-terminus.[9-12]

In this work, FCS was used to measure the dynamics of FRET pair labeled CaM mutants. As discussed in Chapter 1, FRET is the non-radiative transfer of energy from a donor to an acceptor molecule. As the transfer becomes more efficient

fewer photons are emitted from the donor and more photons are emitted from the acceptor. This results in an anti-correlated behavior which can be measured in FCS measurements as discussed in Section 4.2.

In this chapter methods for fitting the FCS correlations are also discussed along with limitations and concerns that need to be considered when reporting dynamics measured through FCS.

4.2. Theory

In FRET fluorescence correlation (FCS) and fluorescence cross-correlation spectroscopy (FCCS) measurements, the dynamics from FRET appear differently in the autocorrelations vs. the cross-correlations of the two channels. Take for example the autocorrelation of the green channel: if while diffusing through the probe volume the FRET efficiency changes from high to low FRET, it will appear as an additional fluctuation in the fluorescence signal, leading to an additional decay component in the correlation much like triplet blinking. This additional decay term can be written as equation 4.1:[13]

$$G_{GG}(\tau) = \left[G_{Triplet}(\tau)G_{Diff}(\tau)\right]\left(1 + a * e^{\left(-t/\tau\right)}\right) \tag{4.1}$$

However, if the green channel is cross-correlated with the red channel then each drop in fluorescence of the green channel due to a change in FRET would be accompanied by an increase in fluorescence in the red channel. Hence, the signals are anti-correlated and result in a rise to the cross-correlation written as equation 4.2:

$$G_{GR}(\tau) = \left[G_{Triplet}(\tau)G_{Diff}(\tau)\right]\left(1 - a * e^{\left(-t/\tau\right)}\right) \tag{4.2}$$

As shown in Chapter 3.2 there are four correlations that can be calculated from the green and red photon streams. Using this, one can set up a set of equations for globally fitting FRET data that contains fluctuations in FRET efficiency. Equations 4.3-4.5 contain the set of equations used for fitting dynamics with two possible time constants (τ_1 and τ_2).

$$G_{GG}(\tau) = \left[G_{Triplet}(\tau)G_{Diff}(\tau)\right]\left[1 + \left(\frac{a}{c^2}\right)e^{\left(-t/\tau_1\right)} + \left(\frac{b}{c^2}\right)e^{\left(-t/\tau_2\right)}\right] \tag{4.3}$$

$$G_{RR}(\tau) = \left[G_{Triplet}(\tau)G_{Diff}(\tau)\right]\left[1 + \left(\frac{a}{d^2}\right)e^{\left(-t/\tau_1\right)} + \left(\frac{b}{d^2}\right)e^{\left(-t/\tau_2\right)}\right] \tag{4.4}$$

$$G_{GR/RG}(\tau) = \left[G_{Diff}(\tau)\right]\left[1 - \left(\frac{a}{cd}\right)e^{\left(-t/\tau_1\right)} - \left(\frac{b}{cd}\right)e^{\left(-t/\tau_2\right)}\right] \tag{4.5}$$

Where a, b, c, and d are constants that are included in the fitting parameters.

Notice that the pre-exponential terms for equations 4.3-4.5 take on forms analogous to the relationship of the initial amplitudes from FRET in Chapter 3.2. At time t = 0 equations 4.3-4.5 are equivalent to equations 3.6-3.8. In the event of one dynamic and one static FRET state one exponential is set to one, which is the equivalent of setting the time constant equal to ∞, leaving a pre-exponential term independent of time. To demonstrate some various scenarios encountered when measuring FRET dynamics, the program SimFCS was used to simulate two channel dynamic FRET data that could then be correlated and fit.

4.3. FCS Simulations

When performing FRET state simulations the total brightness of each FRET pair was fixed to 160,000 cpsm and the relative green and red signals were adjusted to achieve the desired FRET efficiency. The total number of molecules in the simulation box was 300. The final simulation results were correlated on a log scale and globally fit using Excel. Errors for each parameter were determined through the use of support plane analysis using home written Excel macros.

In the first simulation all molecules had the same FRET efficiency where the donor count rate was 100,000 cpsm and the acceptor count rate was 60,000 cpsm. The correlations overlapped as expected (Figure 4.1) and the $\langle N \rangle$ and τ_D values were the same as the fit parameters in Figure 2.12. The next series of simulations used two FRET efficiencies with a dynamics time constant of 147.5 μs to check the ability of the global fitting to recover the dynamics. The FRET efficiencies used and the corresponding count rates are given in Table 4.1. Figure 4.2 contains results from the simulations with decreasing differences in FRET efficiency with the final fit parameters given in Table 4.2. It is clear that in the case of simple diffusion with two well-defined dynamic states the global fitting can reliably recover the FRET dynamics until the FRET efficiencies become too similar as shown with FRET efficiencies of 0.7 and 0.8. In that case, while identifying the presence of dynamics, the fitting parameters had a large uncertainty in the time constant.

In order to better assess the ability to measure FRET dynamics in a system

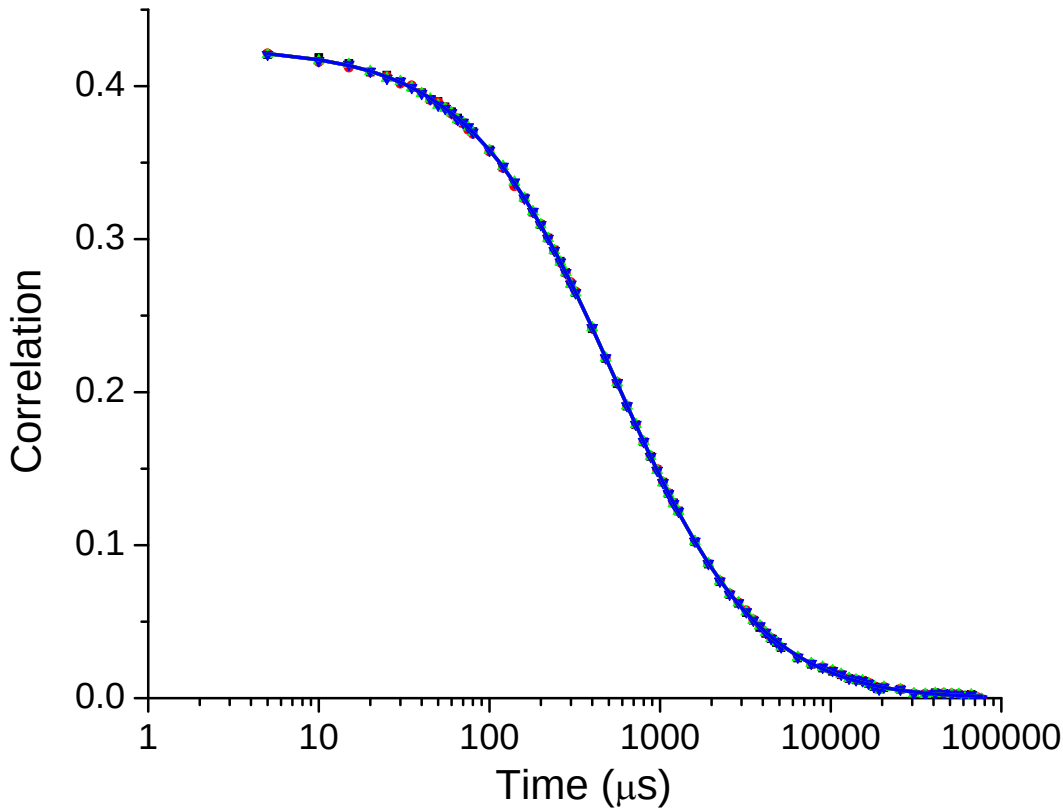

Figure 4.1: SimFCS results for a single FRET state species. All four correlations are perfectly overlapping with $\langle N \rangle = 2.336 \pm 0.006$ and $\tau_D = 546 \pm 3$ μs. Unless noted otherwise $G_{GG}(\tau)$, $G_{RR}(\tau)$, $G_{GR}(\tau)$, and $G_{RG}(\tau)$ in all figures are represented by black squares, red circles, green triangles, and blue inverted triangles respectively with the fits represented by solid lines.

Table 4.1: FRET states used for dynamic FRET simulations with 147 μs switching time constant.

	FRET State 1			FRET State 2		
Simulation #	Donor cpsm	Acceptor cpsm	FRET E	Donor cpsm	Acceptor cpsm	FRET E
1	140,000	20,000	0.125	20,000	140,000	0.875
2	100,000	60,000	0.375	40,000	120,000	0.750
3	80,000	80,000	0.500	40,000	120,000	0.750
4	48,000	112,000	0.700	32,000	128,000	0.800

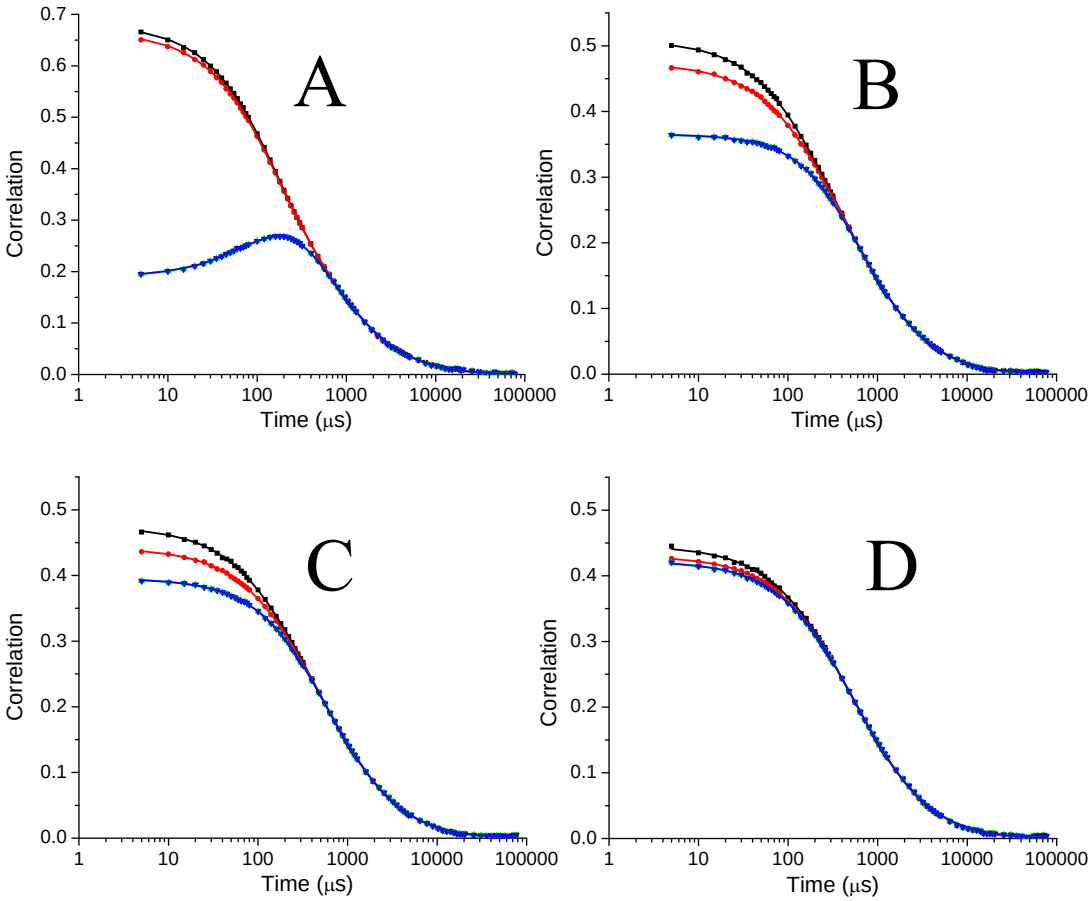

Figure 4.2: FCS simulation correlations and fits with two FRET states interchanging. (A) FRET E of 0.125 and 0.875. (B) FRET E of 0.375 and 0.750. (C) FRET E of 0.500 and 0.750. (D) FRET E of 0.700 and 0.800.

Table 4.2: Fitting results from dynamic FRET simulations. The parameter τ_1 is the dynamics time constant.

FRET E	$\langle N \rangle$	τ_D (μs)	τ_1 (μs)
0.125, 0.875	2.320 ± 0.005	540 ± 5	146 ± 2
0.375, 0.750	2.342 ± 0.005	539 ± 4	149 ± 7
0.500, 0.750	2.355 ± 0.005	542 ± 4	141 ± 12
0.700, 0.800	2.336 ± 0.006	548 ± 5	125^{+62}_{-40}

more similar to CaM, static FRET states were added to the simulation. The two FRET efficiencies were held constant throughout and the percent of species with dynamics was varied to observe the effect a population of static species would have on the ability to fit the dynamics. For each simulation there were always an equal number of molecules in the two static FRET states with the remaining molecules undergoing dynamic FRET. The dynamic FRET efficiencies were the same FRET efficiencies as the static states. For example, the simulation shown in Figure 4.3A was performed with 75 molecules with a static FRET efficiency of 0.4 and 75 molecules with a FRET efficiency of 0.9. The remaining 150 molecules were set to dynamically switch between FRET efficiencies of 0.4 and 0.9 with a time constant of 147.5 μs. Figure 4.3 contains the simulation results for FRET efficiencies 0.4 and 0.9. As is shown in Table 4.3 the fitting is able to recover the dynamics time constant until the percent of dynamic molecules falls to 2%, where the uncertainty in the dynamics time constant is undefined. A more challenging simulation was run with FRET states that are more similar of 0.72 and 0.91 shown in Figure 4.4. As Table 4.3 shows the value for the dynamics time constant is less than the expected value and the uncertainties become large with as low as 17% of the molecules undergoing transitions.

The time constants are not the only information that can be interpreted from the fits. The pre-exponential terms hold information about the relative contribution of the dynamic and static FRET states relative to the diffusional decay of the correlation. The pre-exponential terms for the $G_{GG}(\tau)$ correlation are shown in Table 4.3

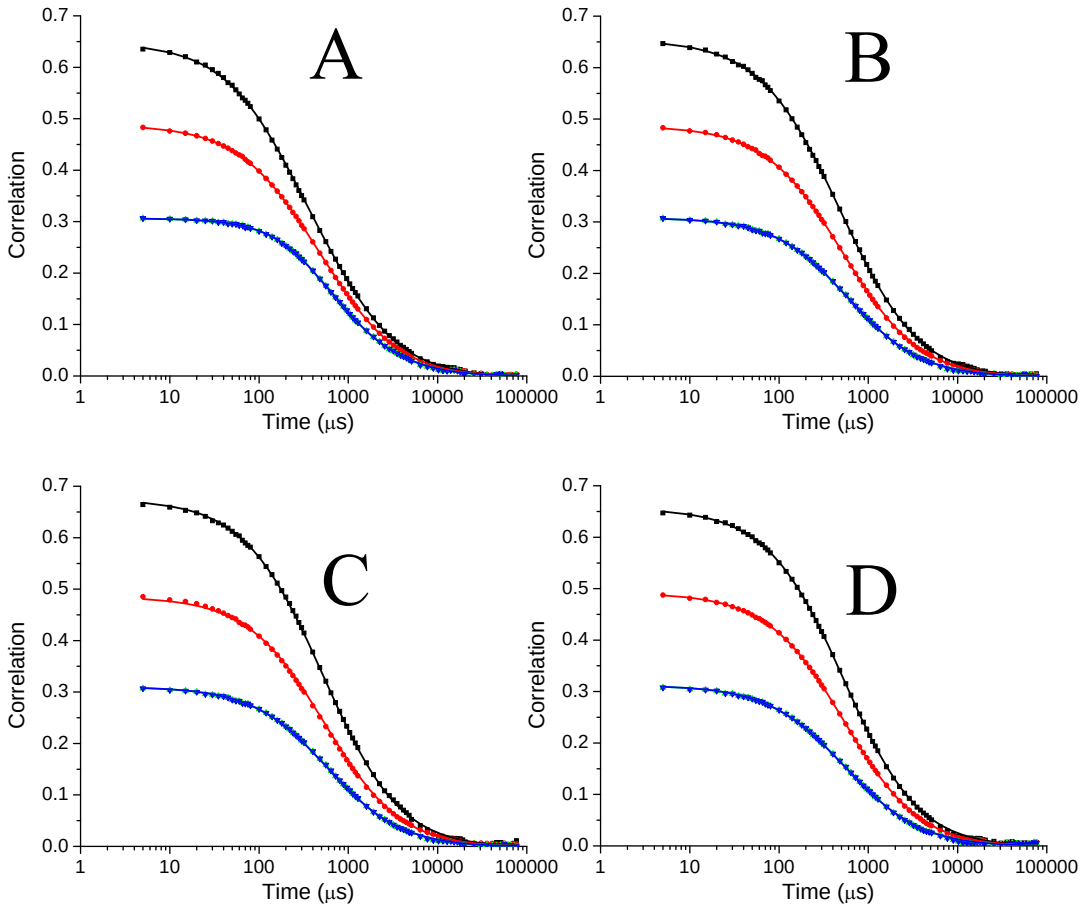

Figure 4.3: FCS simulation results with combined dynamic and static FRET states. The two FRET efficiencies used were 0.4 and 0.9. (A) 50% of dynamic molecules. (B) 17% of dynamic molecules. (C) 6% of dynamic molecules. (D) 2% of dynamic molecules.

Table 4.3: Fitting results from two different combined dynamic and static FRET simulation batches. The parameter τ_1 is the dynamics time constant. The fraction τ_1 is determined by $(a/c^2)/(a/c^2+b/c^2)$.

	% Dynamic	⟨N⟩	τ_D (μs)	τ_1 (μs)	(a/c^2)	(b/c^2)	Fraction τ_1
FRET States 0.4 0.9	50%	2.352 ± 0.006	543 ± 5	145 ± 10	0.25	0.27	0.49
	17%	2.347 ± 0.005	543 ± 4	141 ± 29	0.08	0.46	0.15
	6%	2.333 ± 0.009	557 ± 7	153^{+130}_{-75}	0.05	0.53	0.08
	2%	2.324 ± 0.008	544 ± 7	1300 ± ∞	0.04	0.49	0.07
FRET States 0.72 0.91	50%	2.332 ± 0.007	536 ± 5	142 ± 25	0.12	0.11	0.52
	30%	2.356 ± 0.008	542 ± 5	141^{+70}_{-45}	0.07	0.18	0.27
	17%	2.321 ± 0.008	549 ± 5	122^{+140}_{-65}	0.04	0.21	0.16
	10%	2.33 ± 0.01	542 ± 6	125^{+860}_{-120}	0.02	0.23	0.07

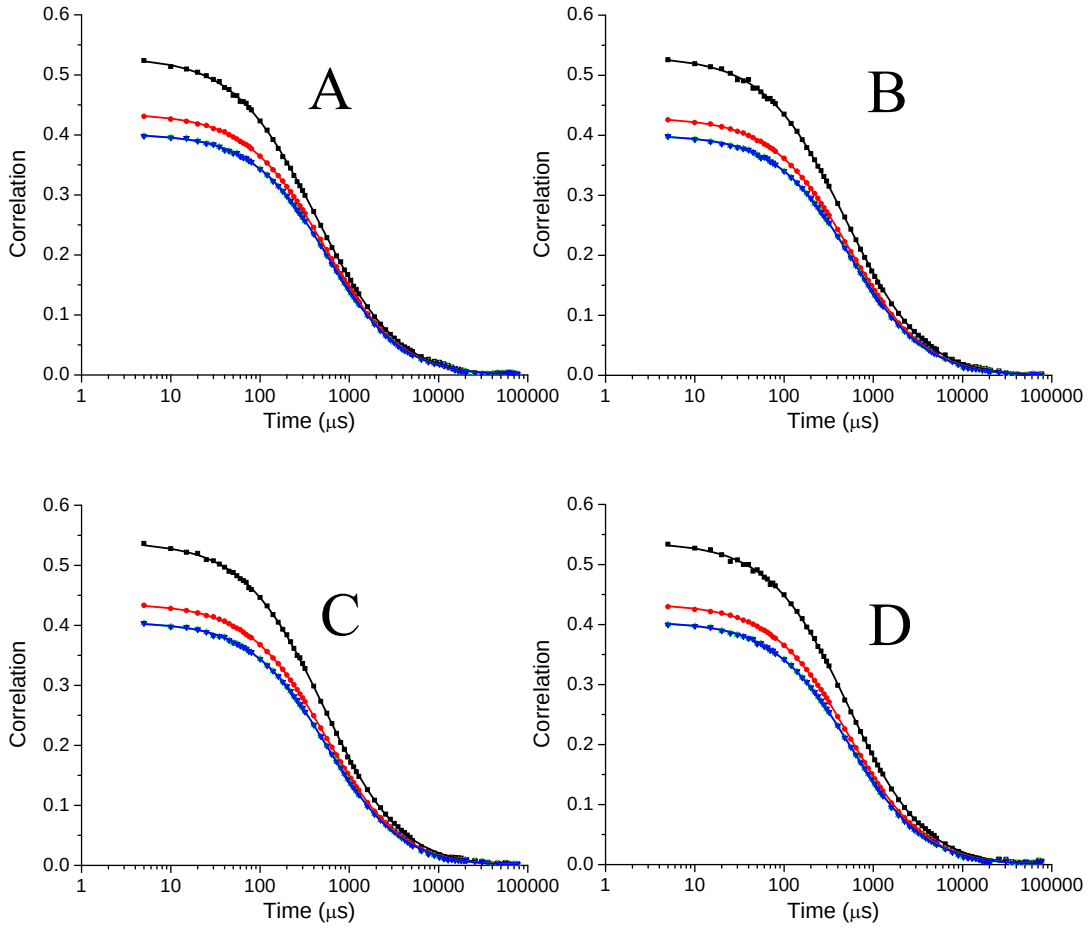

Figure 4.4: FCS simulation results with a percent of two FRET states interchanging and the remainder as static FRET. The two FRET efficiencies used were 0.72 and 0.91. (A) 50% of dynamic molecules. (B) 30% of dynamic molecules. (C) 17% of dynamic molecules. (D) 10% of dynamic molecules.

demonstrating that both the magnitude of the difference in FRET states and the relative contribution of dynamics can be measured from the pre-exponential terms.

From these results it can be said that the global fitting routine is successful in measuring dynamics due to fluctuations in FRET efficiency. However, if the FRET fluctuations are between two states with similar FRET efficiencies and/or if the percentage of molecules is too low, the fit will be unable to discern the presence of dynamics. The fitting becomes even more complex when a real system is used, which also contains triplet dynamics for each dye, adding additional decay components to the correlation curves. The triplet dynamics are an additional exponential decay in the two autocorrelations that generally fall in the 10 μs range. If there are weak dynamics also on that timescale it is possible that they would be partially masked by the triplet decay.

4.4. Materials and Methods

4.4.1. Sample Preparation

Double-labeled CaM was prepared as described in Chapter 2.5.2. The mutants used in this work included CaM-T34C-T110C, CaM-S17C-T117C, and CaM-T5C-T44C. The 34-110 mutant and 17-117 mutant were labeled with the Alexa Fluor 488 and Texas Red dye FRET pair. The 5-44 mutant was labeled with Alexa Fluor 488 and Atto 740 to produce a dye pair with a smaller R_0 than Alexa Fluor 488-Texas Red. High Ca^{2+} buffer was made up of 10 mM HEPES, 0.1 M KCl, 1 mM $MgCl_2$ and 0.1 mM $CaCl_2$. The pH was adjusted to 7.4 using HCl and KOH, then

filtered using a 0.2-μm syringe filter. The low Ca^{2+} buffer was prepared with 10 mM HEPES, 100 mM KCl, 1 mM $MgCl_2$ and 3 mM EGTA. The pH was adjusted to 7.4 using HCl and KOH, then filtered using a 0.2 μm syringe filter. These buffers are sufficient to produce Ca^{2+}-saturated CaM and CaM with no Ca^{2+} bound (apo CaM).

4.4.2. FCS Setup

The microscope arrangement used for this work is the same system as described in Section 3.3.2. The microscope coverslips were pretreated with BSA (as described in Section 3.5) prior to placing about 30 μL of sample on the coverslip. The photon stream was collected to 15 million photons in one of the channels. This limit was chosen solely due to software limitations for correlating the files.

Data collection was performed in photon-mode and the files were correlated and corrected for afterpulsing using the same procedure as described in Chapter 2.2.2.3. The probe volume overlap was checked daily using a sample of ~5 nM fluorescein in 0.1 M NaOH to observe the overlap of the correlations.

4.5. Fluorescence Correlation Spectroscopy

Fluorescence correlation spectroscopy measurements were performed on each CaM mutant using BSA treated slides using each buffer. The concentration of each sample was adjusted to give correlation curves with initial amplitudes in the range of 0.2-1.0. This generally resulted in concentrations of 10-20 nM for each sample.

Correlations were performed on each of the data sets for fitting. In order to calculate the appropriate weighting to use in the fits, each data file was cut into eight equal sections. The correlations were calculated for each of the eight sections from which the variance (σ^2) around each correlation point was calculated. The fits were then weighted by $1/\sigma^2$. The axial-radial ratio for the system had previously been determined to equal eight and was fixed throughout the fitting of the data sets. Figure 4.5 shows the results from correlating a donor-only sample of CaM double labeled with Alexa Fluor 488 that was used for a transit-time reference, as the only dynamics measured in the sample would be diffusion and triplet blinking. The difference in τ_d for the high and low Ca^{2+} buffers was reproducible and does not appear to be a result of changes to the buffer viscosity, as the transit times of free Alexa Fluor 488 dye was 65 ± 3 μs and 64 ± 3 μs for the high and low Ca^{2+} buffers respectively.

The triplet contribution to the $G_{GG}(\tau)$ and $G_{RR}(\tau)$ correlations needed to be considered before determining the dynamics time constant(s). For the mutants labeled with Alexa Fluor 488 and Texas Red, the triplet times and fractions for Alexa Fluor 488 were fixed to values obtained from the CaM-AF488-AF488 sample, and for Texas Red, the polyproline sample results were used to give the Texas Red triplet time and fraction. The values used for the triplet portion of the fits are given in Table 4.4. These values are laser power dependent and were determined using the same laser powers used for the measurements of CaM.

To demonstrate the importance of fixing the triplet components a fit was performed on the CaM-34-110 high Ca^{2+} correlations using equations 4.3-4.5

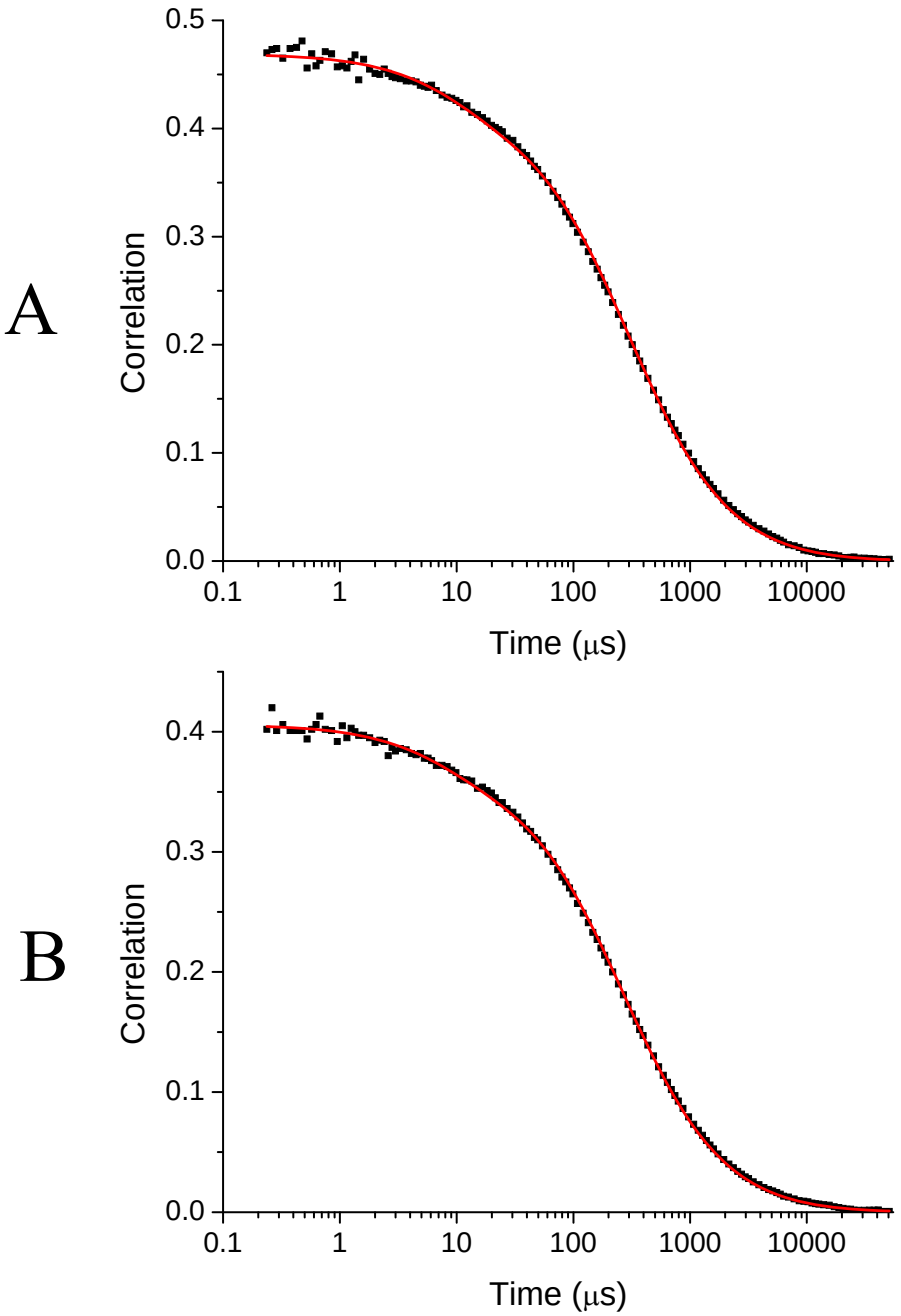

Figure 4.5: CaM-Alexa Fluor 488-Alexa Fluor 488 correlations (black squares) and fits (solid line). (A) High Ca^{2+} buffer fit to $\tau_D = 297 \pm 10$ μs, $f_{triplet} = 0.10 \pm 0.02$, and $\tau_t = 8 \pm 3$ μs. (B) Low Ca^{2+} buffer fit to $\tau_D = 267 \pm 8$ μs, $f_{triplet} = 0.10 \pm 0.02$, and $\tau_t = 8 \pm 3$ μs.

Table 4.4: Triplet parameters used for the correlation fits of CaM samples containing Alexa Fluor 488 and Texas Red.

Parameter	Value
f_1 G_{GG}	0.1
τ_t G_{GG} (μs)	8
f_2 G_{RR}	0.09
τ_t G_{RR} (μs)	18

allowing the triplet parameters to vary. The fits were performed using one exponential for the dynamics with e^{-t/τ_2} fixed to a value of one to account for the apparent static FRET states in each sample. Table 4.5 demonstrates the effect that allowing the triplet component to vary has on the final fit results for CaM 34-110 in high Ca^{2+} buffer. When the triplet component was allowed to vary freely, the FRET dynamics time constant was about 4.2 ms with a very large uncertainty. This is very different from the result that shows a time constant for the high Ca^{2+} CaM 34-110 mutant on the order of 100 μs. In the experiments presented here the triplet times and fractions are well known through the use of the donor only and polyproline controls measured on the same day using the same system settings.

Using the fixed triplet parameters, the CaM-34-110-Alexa Fluor 488-Texas Red correlations were fit to equations 4.3-4.5. After inspection of the fits it was found that the $G_{RR}(\tau)$ correlation had a shorter transit time than the $G_{GG}(\tau)$ correlation. This was most likely due to photobleaching of the acceptor as CaM diffused through the probe volume. To improve the global fitting results two transit times were used to account for the photobleaching, one for $G_{GG}(\tau)$ and the two cross-correlations and another for the $G_{RR}(\tau)$ correlation. Figure 4.6 contains the correlations and resulting fits for CaM-34-110 comparing one or two transit times. Table 4.6 shows the final fit parameters for the plots in Figure 4.6. The reduced χ^2 value for two transit times is much improved over the single transit time as well as the transit time for the $G_{GG}(\tau)$ correlation being in much closer agreement with Figure 4.5A. It was decided that all of the remaining fits would be performed using two transit times.

Table 4.5: Comparison of fits for CaM 34-110 in high Ca^{2+} buffer when fixing or varying the triplet parameters.

Fit Parameter	Fix Triplet	Vary Triplet
$\langle N \rangle$	3.13 ± 0.02	3.15 ± 0.04
f_G	0.1	0.17 ± 0.03
τ_{tG} (μs)	8	32 ± 16
f_R	0.09	0.09 ± 0.02
τ_{tR} (μs)	18	18 ± 12
τ_1 (μs)	92^{+170}_{-60}	4200 ± ∞
a/c^2	0.12 ± 0.06	0.05 ± ∞
b/c^2	1.0 ± 0.6	0.88 ± ∞
τ_1 fraction	0.11 ± 0.06	0.06 ± ∞
χ^2	1.420	1.163

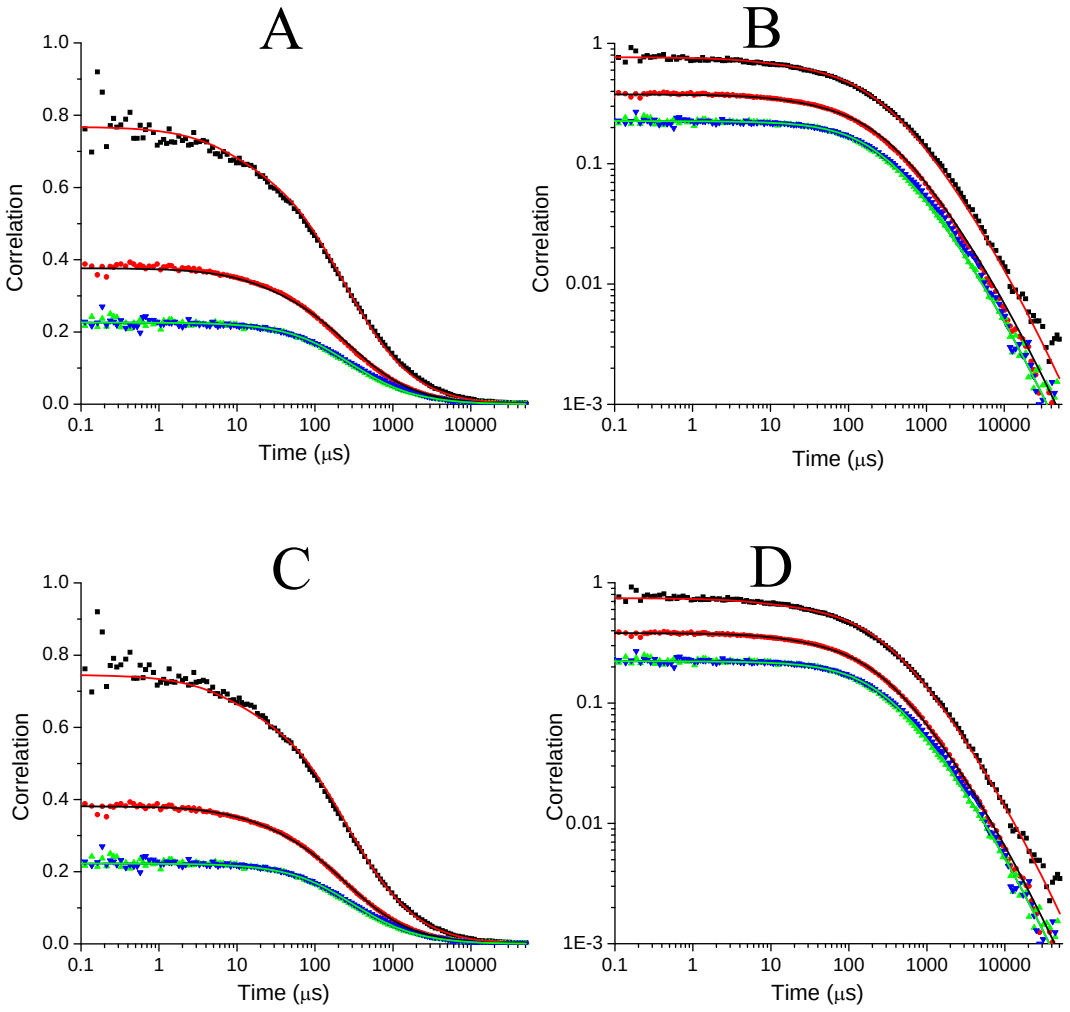

Figure 4.6: Fitting of CaM-34-110 correlations in high Ca^{2+} buffer to one or two transit times. (A) Fit to a single global transit time. (B) Log-Log plot of A to better visualize fitting near the end of the correlation. (C) Fit to two transit times as described in the text. (D) Log-Log plot of C.

Table 4.6: Fitting results for CaM-34-110 in high Ca^{2+} buffer comparing one global transit time to individual transit times for $G_{GG}(\tau)$ and $G_{RR}(\tau)$.

Fit Parameter	Fit using 1 τ_D	Fit using 2 τ_D
$\langle N \rangle$	3.13 ± 0.03	3.13 ± 0.02
τ_D GG (μs)	262 ± 6	281 ± 6
τ_D RR (μs)	N/A	246 ± 5
τ_1 (μs)	81^{+150}_{-60}	92^{+170}_{-60}
a/c^2	0.15 ± 0.09	0.12 ± 0.06
b/c^2	1.0 ± 0.8	1.0 ± 0.6
τ_1 fraction	0.13 ± 0.09	0.11 ± 0.06
χ^2	2.647	1.431

Figure 4.7 shows the correlation results from the two CaM-34-110 samples and the two CaM-17-117 samples and Table 4.7 lists the final fit parameters for each of the samples. To aid in visualizing the dynamics Figure 4.8 shows the correlations normalized using the same method as performed on polyproline in Figure 3.8B. The high Ca^{2+} CaM 34-110 correlations clearly show a fluctuation on the 100's of microseconds timescale (Figure 4.8A) that disappeared in the low Ca^{2+} buffer while the CaM 17-117 correlations do not show dynamics at either Ca^{2+} level. The dynamics measured in the high Ca^{2+} CaM 34-110 correlations agree well with other work that states the Ca^{2+} saturated form of CaM is more dynamic allowing it to adopt the conformations necessary to bind to its targets.[14,15]

One possible explanation for the absence of dynamics in the CaM 17-117 correlations could be due to the position of the dyes on the protein not being as sensitive to the fluctuations that are occurring on the FCS timescale. The 17 and 117 positions are on helices A and G compared to the 34 and 110 residues which are on helices B and F as shown in Figure 4.9. The ~100 microsecond timescale seen with the high Ca^{2+} 34-110 mutant is likely from a wobbling motion of the lobes that results in a measureable change in the distance between residues 34 and 110 while not significantly affecting the distance between residues 17 and 117. One possible wobble could pivot around residue 64 (the residue directly behind 17 when looked at from the perspective of Figure 4.9). This wobble would have a much greater impact on the 34-110 distance without changing the 17-117 distance. A large change from an extended to compact structure of CaM (as shown in the crystal structures in

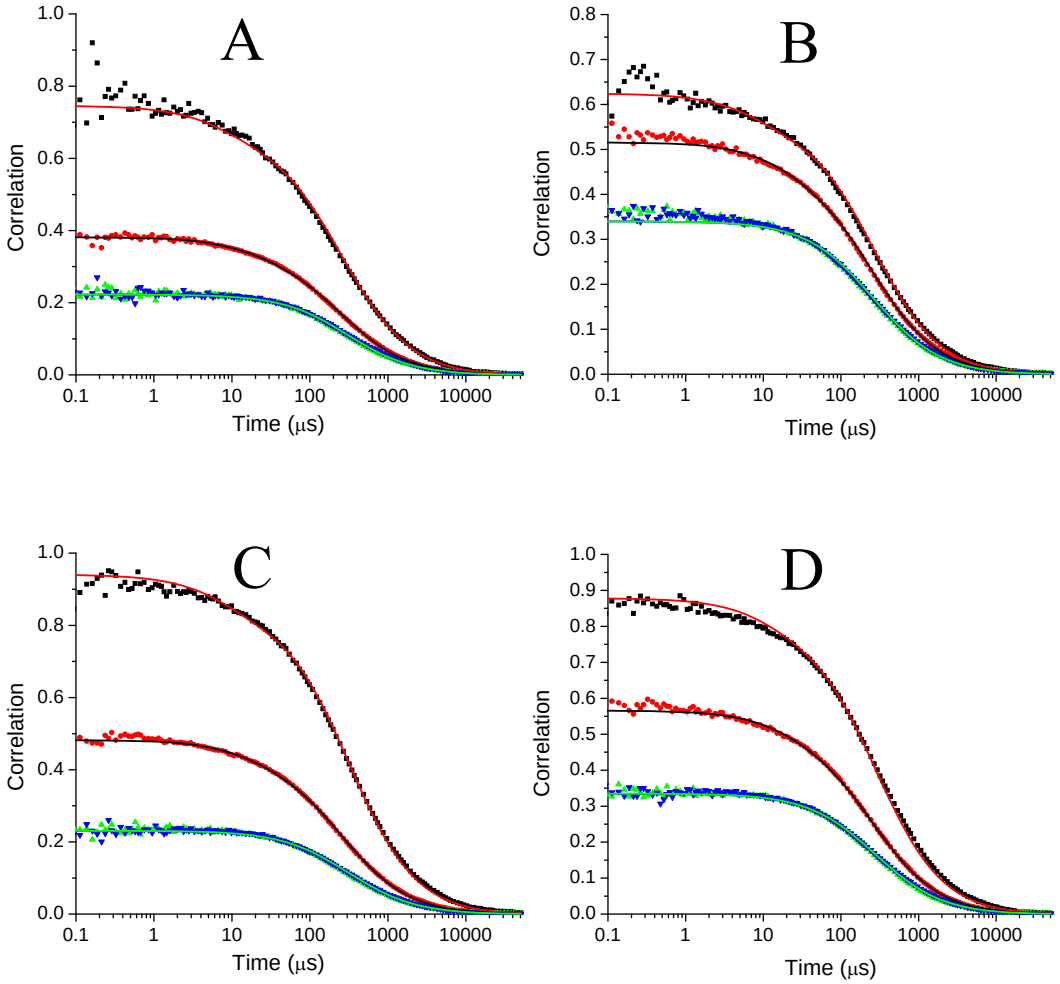

Figure 4.7: Correlation data and fits of CaM-34-110 and CaM 17-117 samples. (A) CaM-34-110 high Ca^{2+} buffer. (B) CaM-34-110 low Ca^{2+} buffer. (C) CaM-17-117 high Ca^{2+} buffer. (D) CaM-17-117 low Ca^{2+} buffer.

Table 4.7: Fitting results for CaM 34-110 and CaM 17-117 samples in both high and low Ca^{2+} buffers. N/A denotes no contribution of that parameter to the fit. All fits contained a static FRET component.

Fit Parameter	34-110 High Ca^{2+}	34-110 Low Ca^{2+}	17-117 High Ca^{2+}	17-117 Low Ca^{2+}
$\langle N \rangle$	3.13 ± 0.02	2.37 ± 0.02	2.59 ± 0.02	2.14 ± 0.02
τ_D GG (μs)	281 ±6	264 ± 6	314 ± 7	279 ± 6
τ_D RR (μs)	246 ± 5	247 ± 8	256 ± 5	250 ± 6
τ_1 (μs)	92^{+170}_{-60}	24,000 ± ∞	N/A	N/A
a/c^2	0.12 ± 0.06	0.10 ± ∞	0.0	0.0
b/c^2	1.0 ± 0.6	0.23 ± ∞	1.19 ± 0.04	0.73 ± 0.03
τ_1 fraction	0.11 ± 0.06	0.30 ± ∞	0.0	0.0
χ^2	1.431	2.532	1.447	3.301

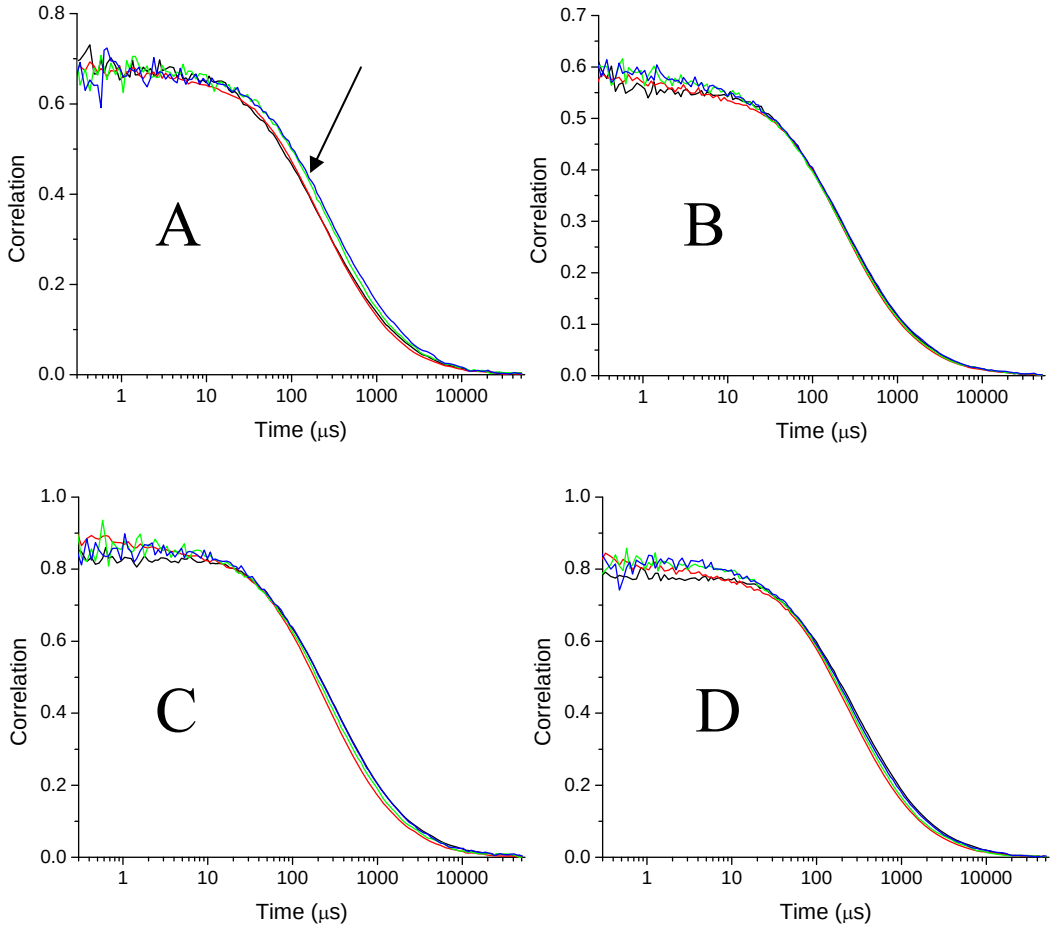

Figure 4.8: Normalized correlations with triplet dynamics removed from data to compare FRET dynamics. $G_{GG}(\tau)$, $G_{RR}(\tau)$, $G_{GR}(\tau)$, and $G_{RG}(\tau)$ shown as black, red, green, and blue lines respectively. (A) High Ca^{2+} 34-110 CaM arrow showing presence of dynamics causing cross-correlations to contain a rise component. (B) Apo 34-110 CaM (C) High Ca^{2+} 17-117 CaM (D) Apo 17-117 CaM.

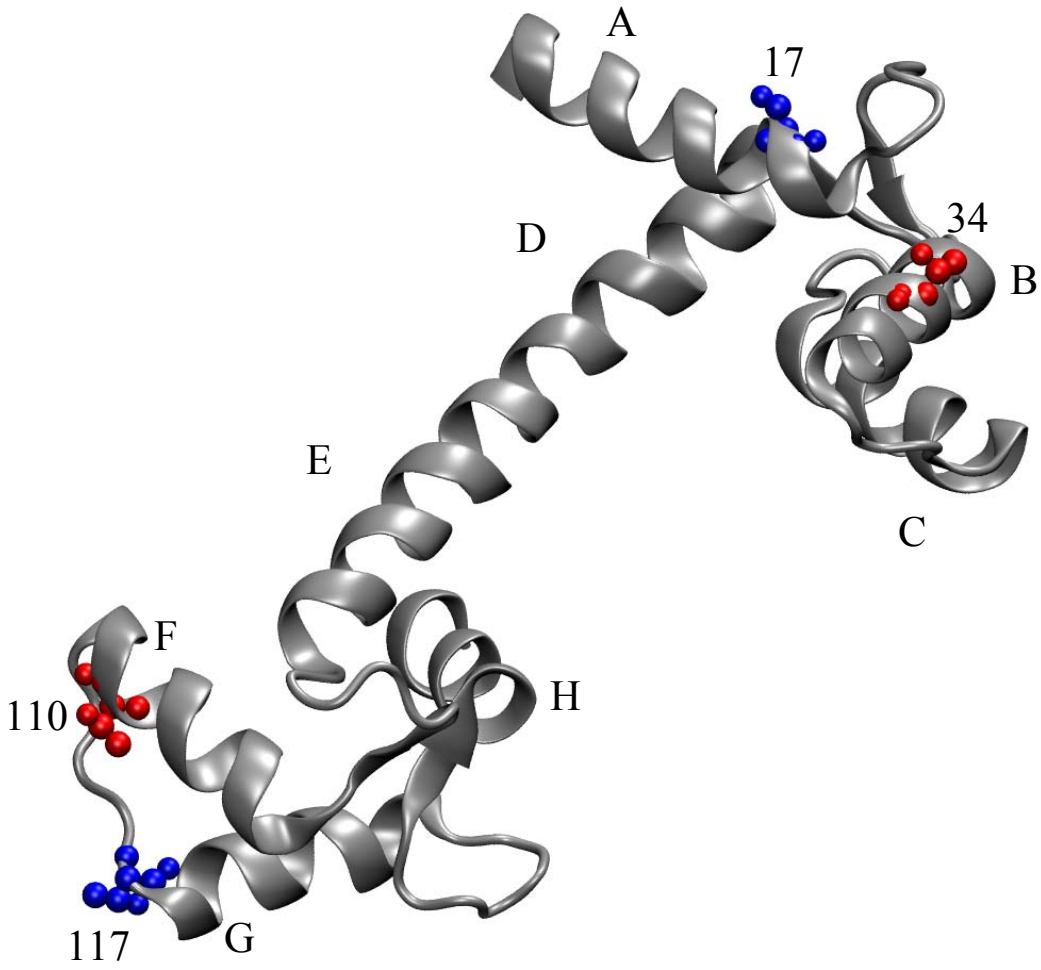

Figure 4.9: Structure of high Ca^{2+} CaM (pdb 3CLN) with residues 34, 110 (shown in red) and 17, 117 (shown in blue) displayed. The helices are labeled A-H.

Figure 1.2) would result in both mutants containing dynamics in the correlations. Also, the change in FRET efficiency from a conformational change like that shown in Figure 1.2 would be large resulting in a larger amplitude in the correlations as demonstrated by the simulations.

The other CaM mutant that was tested was the 5-44 mutant labeled with Alexa Fluor 488 and Atto 740. This mutant was chosen to measure intra-lobe motion of the N-terminus of CaM with and without Ca^{2+} bound. The correlation results and fits for the 5-44 sample at high and low Ca^{2+} levels are shown in Figure 4.10 using a single exponential component for the dynamics as well as a static FRET component. Using the polyproline Alexa Fluor 488-Atto 740 correlation fits from Table 3.7 the triplet times for Alexa Fluor 488 and Atto 740 were fixed to 10 μs and 6.7 μs respectively, the triplet fraction of Alexa Fluor 488 was fixed to 0.07 and the triplet fraction of Atto 740 was allowed to vary due to the high level of noise in the Atto 740 autocorrelation in the polyproline fit. Table 4.8 shows the values of the fits to the high and low Ca^{2+} CaM-5-44 correlations using one dynamics time constant and a static FRET component. According to the fits both the high Ca^{2+} and apo CaM contained FRET dynamics around the 30 μs timescale.

Inspection of Figure 4.10B suggested the need for an additional dynamics time constant to account for the fast dynamics that the fit was missing. A fit was performed using two dynamics time constants and a static FRET component on both high and low Ca^{2+} using equations 4.6-4.8.

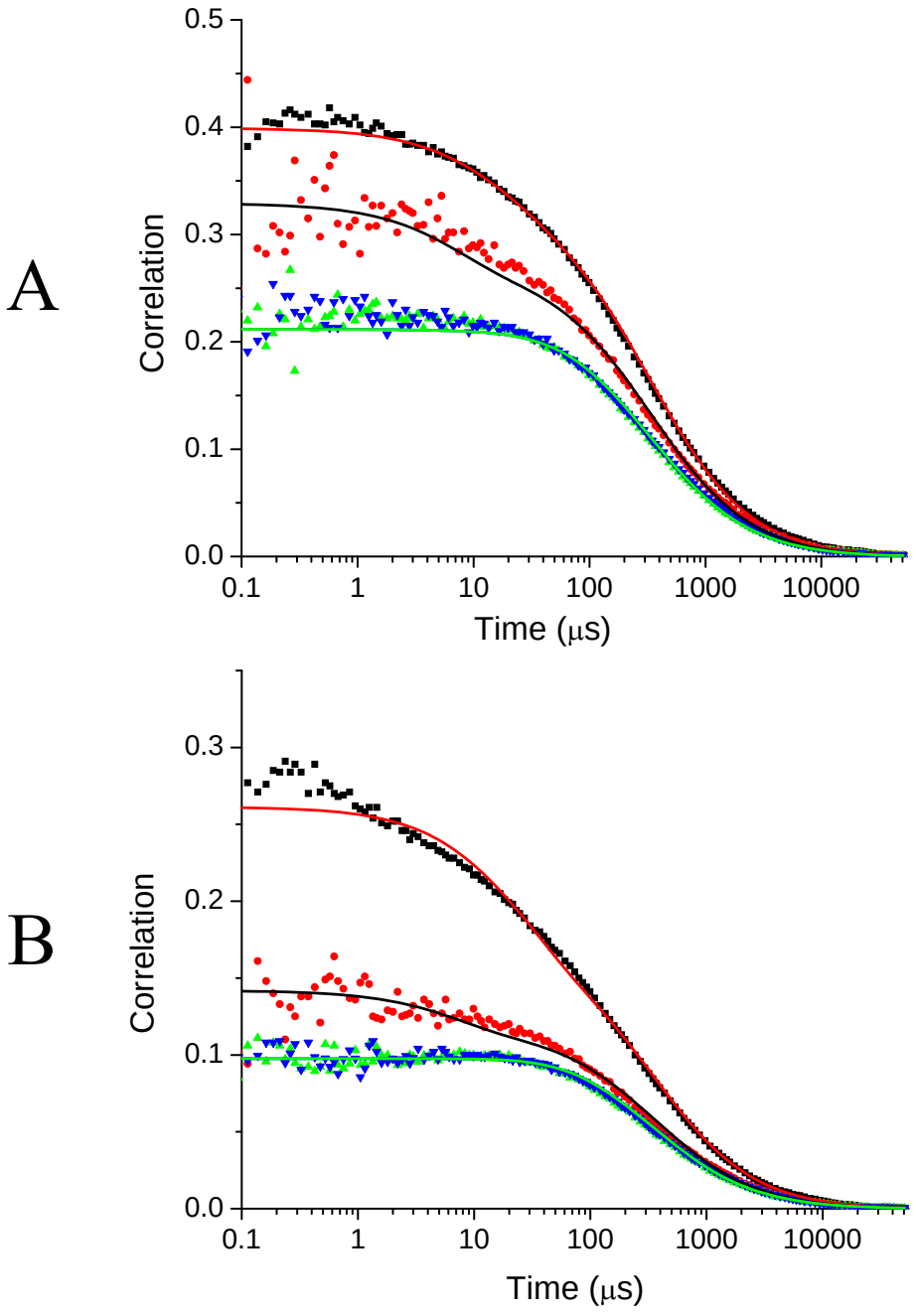

Figure 4.10: Correlation data and fits of CaM-5-44-Alexa Fluor 488-Atto740. (A) High Ca^{2+} CaM 5-44. (B) apo CaM 5-44.

Table 4.8: Fitting results for CaM-5-44 using a single exponential dynamics component (τ_1) and a static FRET component.

Fit Parameter	5-44 High Ca^{2+}	5-44 Low Ca^{2+}
$\langle N \rangle$	3.91 ± 0.08	8.7 ± 0.2
τ_d GG (μs)	330 ± 8	347 ± 10
τ_d RR (μs)	338 ± 21	362 ± 19
τ_1 (μs)	29 ± 14	30 ± 15
a/c^2	0.15 ± 0.03	0.60 ± 0.08
b/c^2	0.3 ± 0.1	0.5 ± 0.1
τ_1 fraction	0.32 ± 0.09	0.54 ± 0.07
χ^2	3.844	9.526

$$G_{GG}(\tau) = \left[G_{Triplet}(\tau)G_{Diff}(\tau)\right]\left[1 + \left(\frac{a}{c^2}\right)e^{\left(-t/\tau_1\right)} + \left(\frac{b}{c^2}\right)e^{\left(-t/\tau_2\right)} + \left(\frac{e}{c^2}\right)\right] \quad (4.6)$$

$$G_{RR}(\tau) = \left[G_{Triplet}(\tau)G_{Diff}(\tau)\right]\left[1 + \left(\frac{a}{d^2}\right)e^{\left(-t/\tau_1\right)} + \left(\frac{b}{d^2}\right)e^{\left(-t/\tau_2\right)} + \left(\frac{e}{d^2}\right)\right] \quad (4.7)$$

$$G_{GR/RG}(\tau) = \left[G_{Diff}(\tau)\right]\left[1 - \left(\frac{a}{cd}\right)e^{\left(-t/\tau_1\right)} - \left(\frac{b}{cd}\right)e^{\left(-t/\tau_2\right)} - \left(\frac{e}{cd}\right)\right] \quad (4.8)$$

The high Ca^{2+} CaM 5-44 fit was not statistically improved though the use of the extra dynamics time constant. The low Ca^{2+} CaM 5-44 fit however, was improved as shown in Figure 4.11 and Table 4.9. Using the pre-exponential terms the relative contributions of the dynamics were compared between the high and low Ca^{2+} correlations. Table 4.10 summarizes the pre-exponential terms calculated for the high Ca^{2+} fit parameters from the fit in Figure 4.10 and for the low Ca^{2+} fit parameters the fit from Figure 4.11. The high Ca^{2+} correlation has a much lower contribution from dynamics (0.15) when compared to the contributions of the two low Ca^{2+} pre-exponentials (0.39 and 0.44) showing that while the high Ca^{2+} sample does have dynamics on the 30 μs timescale, the magnitude of the dynamics is much less than the low Ca^{2+} time constants of ~2 and ~60 μs.

This result suggests a very fast motion of the N-terminal domain when there is no Ca^{2+} bound that is decreased when two Ca^{2+} are complexed with the N-terminal lobe as has been previously discussed.[16] This is in good agreement with NMR work that demonstrates poor structure and high dynamics of the N-terminal lobe when in the absence of Ca^{2+}.[5,9,17,18]

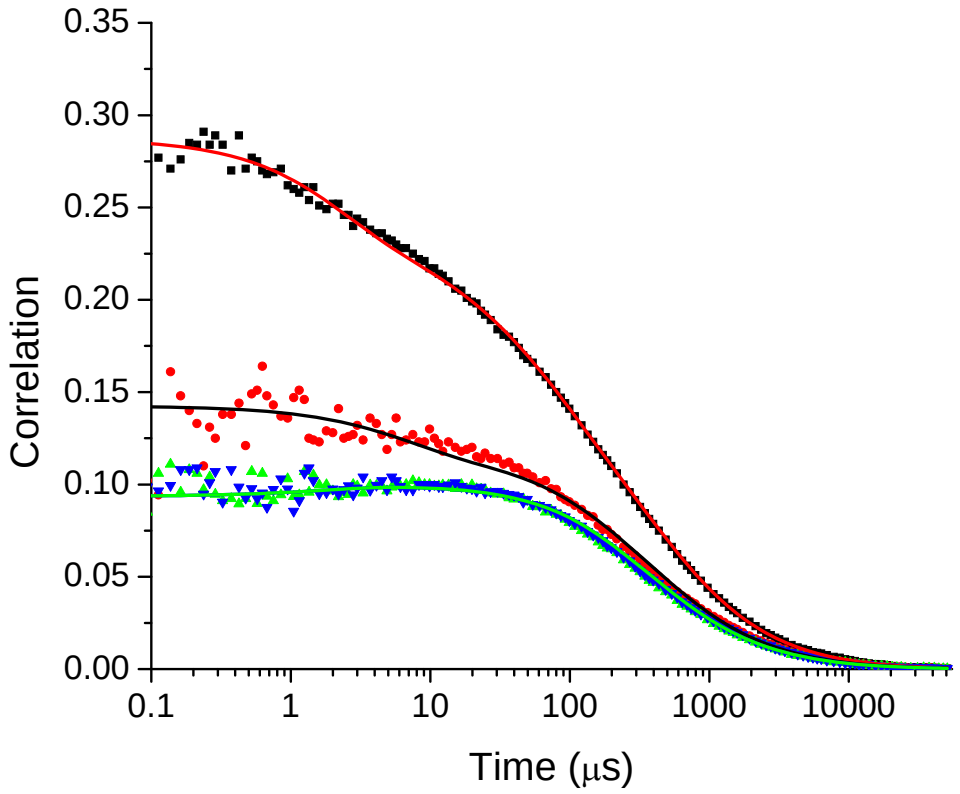

Figure 4.11: Fit of CaM 5-44 correlations in low Ca^{2+} buffer to two dynamics time constants and a static FRET state.

Table 4.9: Fitting results for CaM-5-44 using a single exponential dynamics component (τ_1) and a static FRET component.

Fit Parameter	5-44 Low Ca^{2+}
$\langle N \rangle$	8.7 ± 0.2
τ_d GG (μs)	349 ± 10
τ_d RR (μs)	362 ± 20
τ_1 (μs)	$2^{+5.2}_{-1.7}$
τ_2 (μs)	60^{+60}_{-30}
a/c^2	0.4 ± 0.2
b/c^2	0.5 ± 0.4
e/c^2	0.4 ± 0.4
τ_1 fraction	0.3 ± 0.1
τ_2 fraction	0.3 ± 0.1
χ^2	7.920

Table 4.10: Pre-exponential terms comparison between high and low Ca^{2+} correlation fits.

Parameter	5-44 High Ca^{2+}	5-44 Low Ca^{2+}
a/c^2 (dynamic)	0.15 ± 0.03	0.4 ± 0.2
b/c^2 (static)	0.3 ± 0.1	0.5 ± 0.4
e/c^2 (dynamic)	N/A	0.4 ± 0.4

4.6. Conclusions

The work shown in this chapter has demonstrated the ability to globally fit auto and cross-correlation curves from FCS data while including FRET dynamics. Using FCS simulations it was demonstrated that it was possible in a system that contained both dynamic and static species to recover the correct time constant for the dynamics and compare the magnitude and fraction of the dynamics through the use of the pre-exponential terms. The limit of the technique depended on the difference in FRET efficiency for the two states. A larger difference in FRET efficiency (Figure 4.3) meant that even with only six percent of the molecules in a dynamic state it was possible to still fit the dynamics.

The inter-lobe dynamics measured using the 34-110 and 17-117 mutants of CaM fit to a dynamic state for only the high Ca^{2+} 34-110 CaM correlations. It was proposed that there are wobble motions that could explain this result where the distance between the 34 and 110 residues were changing while the distance between the 17 and 117 residues were not undergoing a measurable fluctuation. It has been shown previously that the two lobes of CaM can undergo a wobbling motion in the presence of Ca^{2+} which supports the proposed 34-110 results.[15,19] Future work to elucidate the motions could be performed using additional mutants such as 34-117 and 17-110 to provide more points of reference for the source of the motions.

The 5-44 mutant correlations showed interesting results with the apo CaM sample showing more dynamics than the high Ca^{2+} CaM sample on the microsecond timescale. When considering the position of the mutations at the beginning of helix

A and helix C as shown in Figure 4.12, the fluctuations in those helices should decrease upon the binding of Ca^{2+} as it adds rigidity to the N-terminal lobe that is absent in the apo state. The fast 2 μs component could possibly arise from random motions of helix A that occur when there is no Ca^{2+} bound to loop I (the EF-hand loop directly after helix A). The 30 μs timescale dynamics measured for the high Ca^{2+} 5-44 CaM is possibly a measure of the opening and closing of the EF-hands as Ca^{2+} exchanges on and off of the N-terminus, which agrees well with previous work measuring exchange times on the order of 50 μs for the C-terminus through NMR measurements [5] and 30 μs for the N-terminus using simulations.[9] The 60 μs dynamics measures for apo CaM could be a result of similar opening and closing of the EF-hands but without the exchange of Ca^{2+}.

Through this work it was learned that consideration must be made to the effect of triplet dynamics when measuring FRET dynamics. Ideally the triplet dynamics would be measured independently in a system that contained no other dynamics so that the triplet parameters could be fixed in the fitting of the FRET dynamics. With careful measurements the use of FCS to measure dynamics is a powerful single-molecule tool capable of monitoring fast microsecond dynamics that are difficult to resolve using other methods.[8]

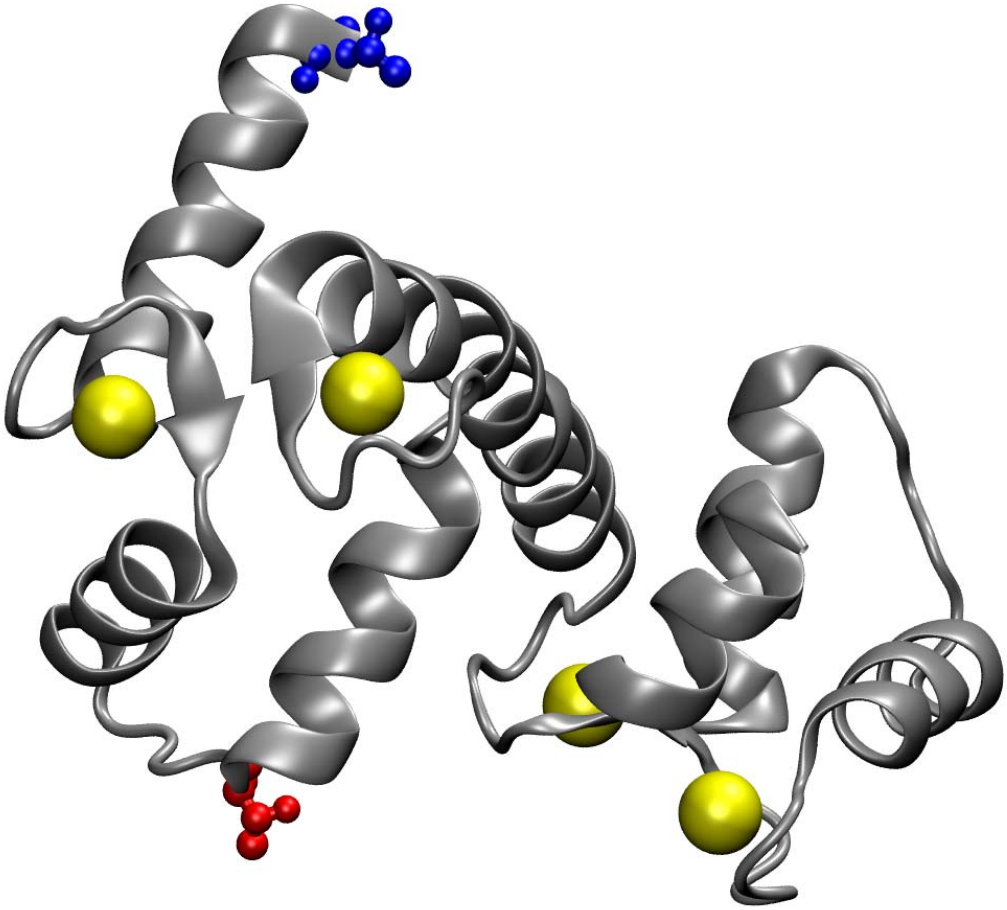

Figure 4.12: Structure of high Ca^{2+} CaM (pdb 3CLN) with residues 5 (blue) and 44 (red) shown. Yellow spheres represent bound Ca^{2+}.

4.7. References

1. Barbato, G., Ikura, M., Kay, L. E., Pastor, R. W., and Bax, A., *Backbone Dynamics of Calmodulin Studied by 15N Relaxation Using Inverse Detected Two-Dimensional NMR Spectroscopy: The Central Helix Is Flexible*. Biochemistry, **1992**. 31(23): p. 5269-5278.

2. Chen, B. W., Mayer, M. U., Markillie, L. M., Stenoien, D. L., and Squier, T. C., *Dynamic Motion of Helix a in the Amino-Terminal Domain of Calmodulin Is Stabilized Upon Calcium Activation*. Biochemistry, **2005**. 44(3): p. 905-914.

3. Ehrhardt, M. R., Urbauer, J. L., and Wand, A. J., *The Energetics and Dynamics of Molecular Recognition by Calmodulin*. Biochemistry, **1995**. 34(9): p. 2731-2738.

4. Wriggers, W., Mehler, E., Pitici, F., Weinstein, H., and Schulten, K., *Structure and Dynamics of Calmodulin in Solution*. Biophys. J., **1998**. 74(4): p. 1622-1639.

5. Evenäs, J., Forsen, S., Malmendal, A., and Akke, M., *Backbone Dynamics and Energetics of a Calmodulin Domain Mutant Exchanging between Closed and Open Conformations*. J. Mol. Biol., **1999**. 289(3): p. 603-617.

6. Best, R. B., and Hummer, G., *Biochemistry Unfolding the Secrets of Calmodulin*. Science, **2009**. 323(5914): p. 593-594.

7. Chen, B. W., Lowry, D. F., Mayer, M. U., and Squier, T. C., *Helix A Stabilization Precedes Amino-Terminal Lobe Activation Upon Calcium Binding to Calmodulin*. Biochemistry, **2008**. 47(35): p. 9220-9226.

8. Park, H. Y., Kim, S. A., Korlach, J., Rhoades, E., Kwok, L. W., Zipfel, W. R., Waxham, M. N., Webb, W. W., and Pollack, L., *Conformational Changes of Calmodulin Upon Ca^{2+} Binding Studied with a Microfluidic Mixer*. Proc. Natl. Acad. Sci. U.S.A., **2008**. 105(2): p. 542-547.

9. Tripathi, S., and Portman, J. J., *Inherent Flexibility and Protein Function: The Open/Closed Conformational Transition in the N-Terminal Domain of Calmodulin*. J. Chem. Phys., **2008**. 128(20): p.

10. Laine, E., Blondel, A., and Malliavin, T. E., *Dynamics and Energetics: A Consensus Analysis of the Impact of Calcium on Ef-Cam Protein Complex*. Biophys. J., **2009**. 96(4): p. 1249-1263.

11. Yang, C., Jas, G. S., and Kuczera, K., *Structure and Dynamics of Calcium-Activated Calmodulin in Solution*. J. Biomol. Struct. Dyn., **2001**. 19(2): p. 247-271.

12. Yang, C., Jas, G. S., and Kuczera, K., *Structure, Dynamics and Interaction with Kinase Targets: Computer Simulations of Calmodulin*. Biochim. Biophys. Acta, **2004**. 1697(1-2): p. 289-300.

13. Widengren, J., and Mets, U., *Conceptual Basis of Fluorescence Correlation Spectroscopy and Related Techniques as Tools in Bioscience*. in *Single Molecule Detection in Solution*. Zander, C., and Keller, R. A., editors. **2003**. Wiley-VCH: Berlin. p. 69-120.

14. Chou, J. J., Li, S., Klee, C. B., and Bax, A., *Solution Structure of Ca^{2+}-Calmodulin Reveals Flexible Hand-Like Properties of Its Domains*. Nat. Struct. Biol., **2001**. 8(11): p. 990-997.

15. Baber, J. L., Szabo, A., and Tjandra, N., *Analysis of Slow Interdomain Motion of Macromolecules Using NMR Relaxation Data*. J. Am. Chem. Soc., **2001**. 123(17): p. 3953-3959.

16. Vigil, D., Gallagher, S. C., Trewhella, J., and Garcia, A. E., *Functional Dynamics of the Hydrophobic Cleft in the N-Domain of Calmodulin*. Biophys. J., **2001**. 80(5): p. 2082-2092.

17. Kuboniwa, H., Tjandra, N., Grzesiek, S., Ren, H., Klee, C. B., and Bax, A., *Solution Structure of Calcium-Free Calmodulin*. Nat. Struct. Biol., **1995**. 2(9): p. 768-776.

18. Zhang, M., Tanaka, T., and Ikura, M., *Calcium-Induced Conformational Transition Revealed by the Solution Structure of Apo Calmodulin*. Nat. Struct. Biol., **1995**. 2(9): p. 758-767.

19. Chang, S.-L., and Tjandra, N., *Analysis of NMR Relaxation Data of Biomolecules with Slow Domain Motions Using Wobble-in-a-Cone Approximation*. J. Am. Chem. Soc., **2001**. 123(46): p. 11484-11485.

5. Immobilized CaM FRET Dynamics

5.1. Introduction

To measure slower dynamics of CaM than the microsecond timescales that can be sampled with FCS methods an alternative approach is needed. A common method to measure slow dynamics with single molecules is to immobilize the molecules, allowing the fluorescence from each molecule to be collected until the fluorophore irreversibly photobleaches. Many methods have been used to immobilize molecules for single-molecule spectroscopic techniques such as an agarose gel,[1-3] hydrogels,[4] or surface immobilization techniques.[5-10] Agarose gels and hydrogels require the protein to be large enough to be held within the polymer matrix. In the case of CaM the pores in agarose gels are too large, and it is able to freely diffuse throughout the gel.[2] Within the realm of surface immobilization, the use of biotin-streptavidin chemistry has proved to be very useful. By functionalizing a coverslip surface with a biotin molecule, streptavidin can then be washed over the surface where it forms one of the strongest known protein-ligand interactions with a K_d on the order of a few femtomolar.[11] A single streptavidin protein has the ability to bind up to four biotin molecules, making it a very convenient linker when the species that one wants to immobilize also contains a biotin, forming a biotin-streptavidin-biotin system at the coverslip surface.

The difficulty lies in the fact that the very act of immobilizing a protein has the potential to alter the structure and dynamics, defeating the whole purpose of the measurements. If the protein itself is biotinylated, it can easily participate in the

immobilization. However, now a part of the protein is tethered to the surface, which if not carefully checked could result in changes to the protein function and possibly even denaturation of the protein. A promising technique to avoid the direct tethering of the protein is through the use of unilamellar vesicles.[10,12,13] By using lipids functionalized with biotin when forming the vesicles and encapsulating the protein for study within the vesicle, the system can now be immobilized to a coverslip surface.

Several studies have demonstrated millisecond motion for calmodulin.[14-16] This chapter will present work performed on CaM-34-110 labeled with Alexa Fluor 488 and Texas Red as used in Chapter 4. Through encapsulation of the protein inside of immobilized unilamellar lipid vesicles millisecond dynamics were measured for both Ca^{2+} saturated CaM and apo CaM.

5.2. Materials and Methods

5.2.1. Protein Encapsulation

Calmodulin was encapsulated inside 100 nm vesicles using techniques described by Haran.[12,17-19] For the immobilization to work, a small fraction of the lipids forming the vesicles must be functionalized with biotin. Stock solutions of phosphatidylcholine (PC) and 16:0 biotinyl cap phosphatidylethanolamine (biotin PE) (Avanti Polar Lipids, Alabaster, AL) were prepared by dissolving 100 mg of PC in 10 mL of chloroform and 5 mg of biotin PE in 5 mL of chloroform and stored at -20°C. A 100:1 mixture of PC to biotin PE was prepared by pipeting 500 μL of the PC stock

and 70 μL of the biotin PE stock into a microcentrifuge tube where it was mixed thoroughly. The chloroform was then evaporated under nitrogen and the sample was then placed in a vacuum desiccator overnight. The next morning CaM that had been dialyzed into the buffer of choice for the experiment was diluted to give a final concentration of ~25 nM of CaM with a volume of 250 μL. The desiccated lipid was then hydrated with the CaM sample and subjected to ten freeze-thaw cycles between a liquid nitrogen bath and a 30°C water bath.

To form the large unilamellar vesicles the sample was extruded using the apparatus described by Macdonald et al.[20] The extrusion was performed eleven times using a 100 nm pore membrane. The unencapsulated protein was separated from the vesicle-entrapped protein using a Sepharose 4B column (GE Healthcare, Piscataway, NJ) equilibrated with the same buffer used to prepare the vesicles. Fractions were collected dropwise (4 drops each) and analyzed by placing 10 μL of each fraction on the single-molecule microscope, exciting with the 488 nm laser, and recording the count rates. A crude chromatogram was then constructed to determine the appropriate fraction to use for the immobilization procedure (Figure 5.1). The vesicles were used within 24 hours of formation to ensure their integrity.[12]

5.2.2. Flow Cell Preparation

In order to allow for extended scanning and recording of immobilized molecules, flow cells were constructed to reduce evaporation and ease the surface modifications needed for immobilization. Prior to construction the bottom and top

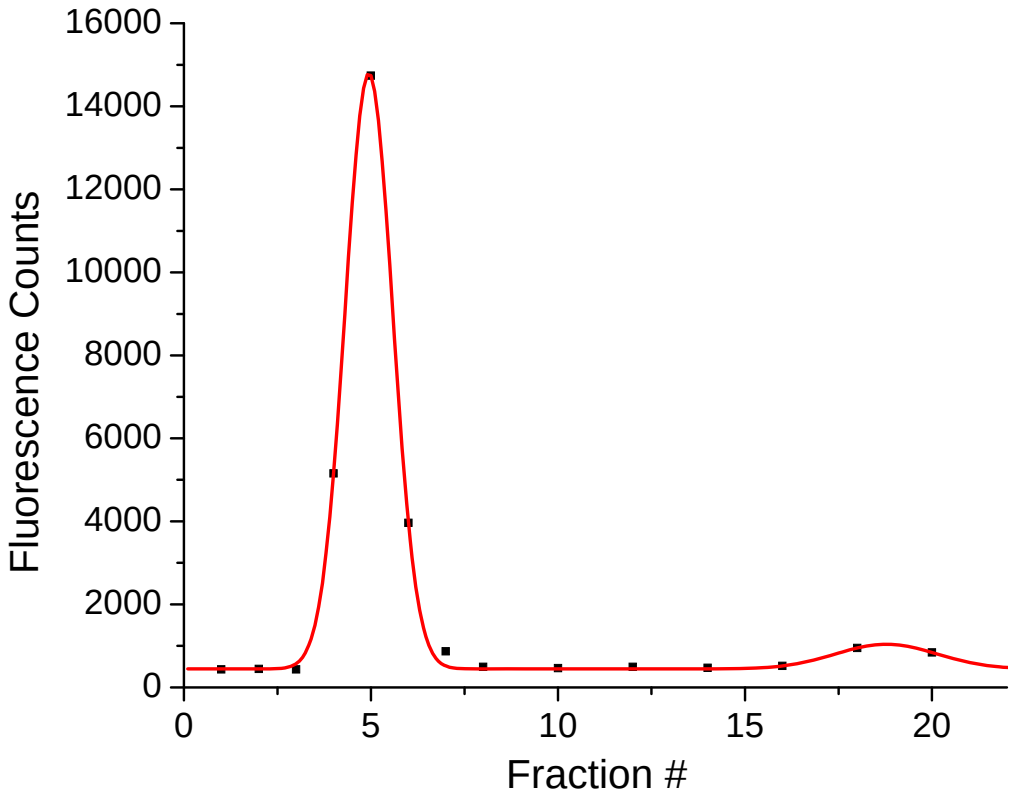

Figure 5.1: Separation of encapsulated CaM (peak at fraction 5) from un-encapsulated CaM (peak at fraction 19). Data represented by squares and Gaussian fits to data represented by red line.

coverslips (25 x 25 mm and 22 x 22 mm, respectively; Fisher Scientific, Pittsburgh, PA) were cleaned by soaking in methylene chloride then alternating between a concentrated sulfuric acid wash and a 70% 2-propanol, 30% 0.7 M KOH base wash four times with thorough rinsing with 18 MΩ water between the acid and base washes with a final drying using a dry nitrogen gas stream. The actual flow-cells were constructed by using liquid superglue to glue two pairs of uncleaned 25 x 25 mm coverslips together to form a spacer for the channel. Then the final flow-cell was glued together using one cleaned 25 x 25 mm coverslip for the bottom glued to the two spacers followed by a cleaned 22 x 22 mm coverslip for the top (Figure 5.2). The flow-cells were allowed to dry for at least one hour.

The best method to fill and exchange solutions in the flow-cells was through the use of a 100 μL syringe with a 33 gauge needle and a lab tissue. The lab tissue was used to draw the solution through the flow-cell while continuously replacing it with the solution in the syringe. To prepare the surface of the flow-cell for immobilization, a 20 mg/mL lipid solution in water was prepared using the same procedure for forming the vesicles up to the hydrating of the lipids. This lipid solution was incubated in the flow-cell for 30 minutes to form the lipid bilayer. The excess lipid was then washed out using 500 μL of the same buffer used for the preparation of the vesicles. A 0.2 mg/mL streptavidin solution in the same buffer as the wash buffer was then incubated in the flow cell for 10 minutes after which it was washed with 500 μL of buffer, leaving the surface prepared for immobilization (Figure 5.3A). The final step was the incubation of the separated fraction at an

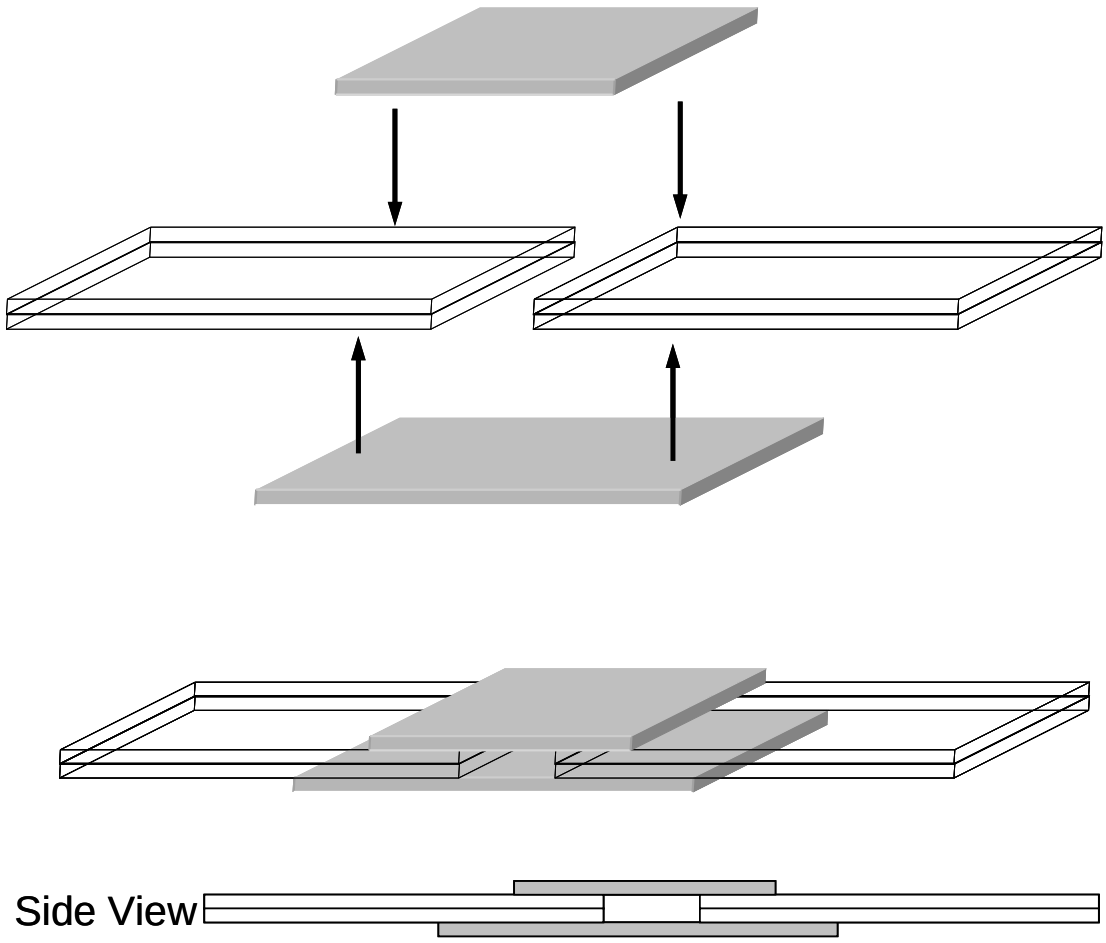

Figure 5.2: Construction of a flow cell for vesicle immobilization. Gray represents cleaned slides. The final channel dimensions are approximately 0.3 mm x 4 mm x 22 mm.

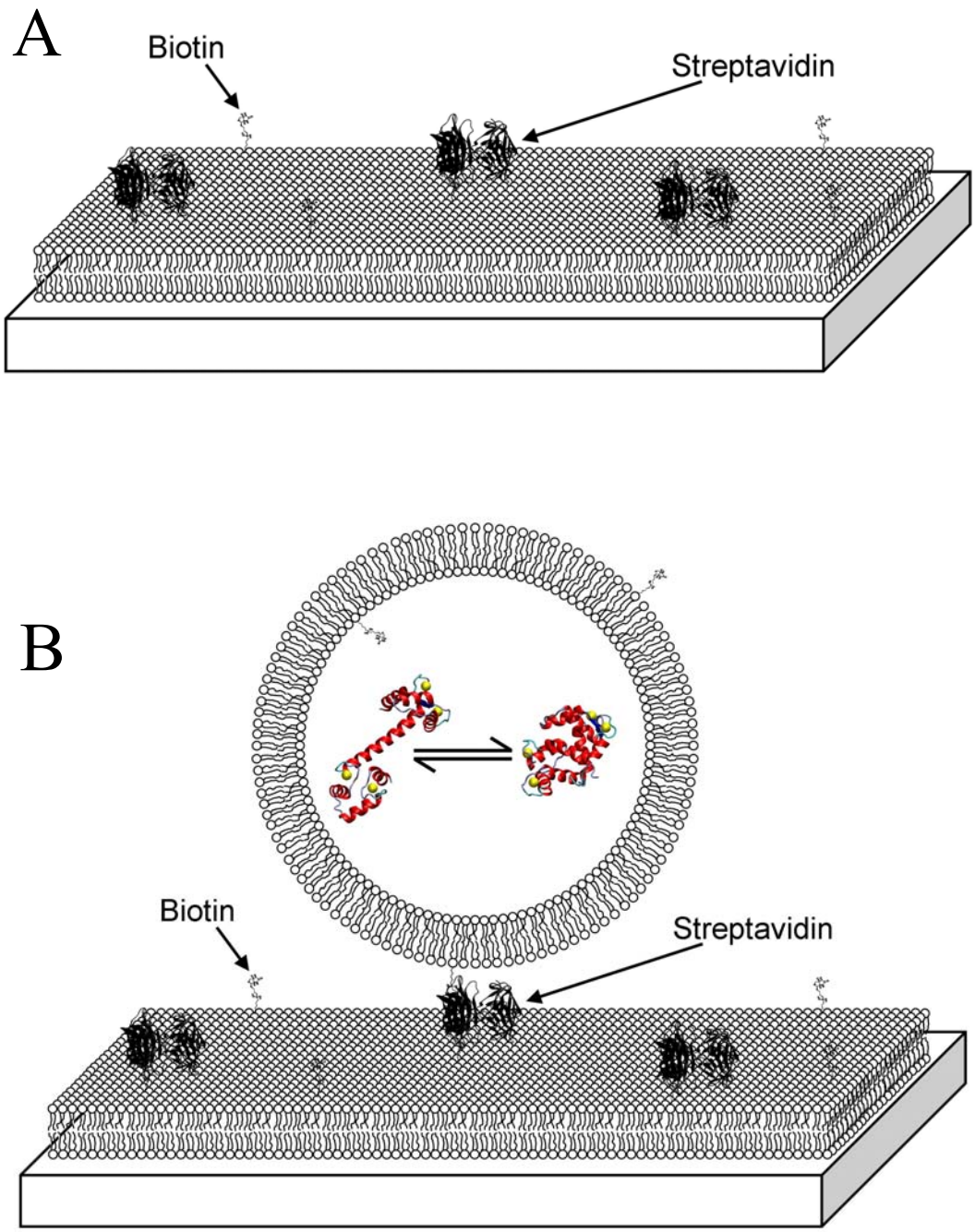

Figure 5.3: (A) Final treated flow-cell surface makeup. (B) Final vesicle immobilization on surface of flow cell.

appropriate dilution for 5 minutes. The dilution of the fraction needed to be sufficient enough to keep the molecules well separated on the surface, but if the dilution was to0 great, finding molecules on the surface was very difficult. The non-specifically bound vesicles were then thoroughly washed out with 1 mL of buffer and the finished flow cell was then placed on the microscope scanning stage and carefully held in place with tape. Figure 5.3B is a representation of the final surface conditions with a vesicle specifically bound to a streptavidin. A well-made flow cell was capable of containing the ~20 μL volume for at least 30 minutes. While scanning with a single slide the buffer was replenished in the flow cell regularly to keep the sample hydrated.

5.2.3. Single-Molecule Scanning

Vesicles containing double-labeled CaM-34-110 were prepared in high and low Ca^{2+} buffers. The high Ca^{2+} buffer consisted of 10 mM HEPES, 100 mM KCl, 1 mM $MgCl_2$, and 0.1 mM $CaCl_2$, which was adjusted to pH 7.4 with KOH and HCl, then filtered using a 0.2 μm syringe filter. The low Ca^{2+} buffer was made up of 10 mM HEPES, 100 mM KCl, 1 mM $MgCl_2$ and 3 mM EGTA, which was adjusted to pH 7.4 using KOH and HCl, then filtered using a 0.2 μm syringe filter. Each prepared flow-cell was used for a period of about 2 hours, refilling the cell with buffer as needed.

Immobilized molecules were located using the single-molecule imaging setup described in Chapter 2.2.4. In order to visualize the molecules in the scanning software the signal from one of the APD's had to be sent to both the PCI-6602 card

(for data acquisition) and the PCI-6052E card for the building of the image. For this work a T-junction was placed in the output line from the acceptor channel APD leading to only observing acceptor active molecules while scanning. This greatly reduced the number of molecules in the image that were either impurities or ones where the acceptor was absent or photobleached when compared to scanning in the donor channel.

All scans were performed on a 15 x 15 μm area using a raster scanning mode with a scan rate of 1.5 Hz per line with a laser power of 1 μW at 488 nm. To form an image of 256 x 256 pixels the scanner stepped in 60 nm increments with a dwell time of 1.3 ms for each pixel. Once an image was produced the laser was shuttered and molecules were identified based on the intensity of the spots over the background. The scanning stage was then moved one molecule at a time to position each in the observation volume. The laser power was adjusted to 5 μW, the data collection software started, and the shutter opened until after photobleaching of the molecules had occurred. The data from each channel was collected in photon mode and written to donor and acceptor files, which were subsequently loaded into a Labview program written to display the fluorescence counts in each channel as a function of time (Figure 5.4). For every single-molecule trajectory the start time (laser on) and stop time (photobleach event) for the trajectory was found by eye (see examples in Figure 5.5) and then the file name, start time, and stop time was written to a batch file for further processing. The use of a batch file allowed for data analysis to be performed on all molecules of a given experimental condition quickly and easily.

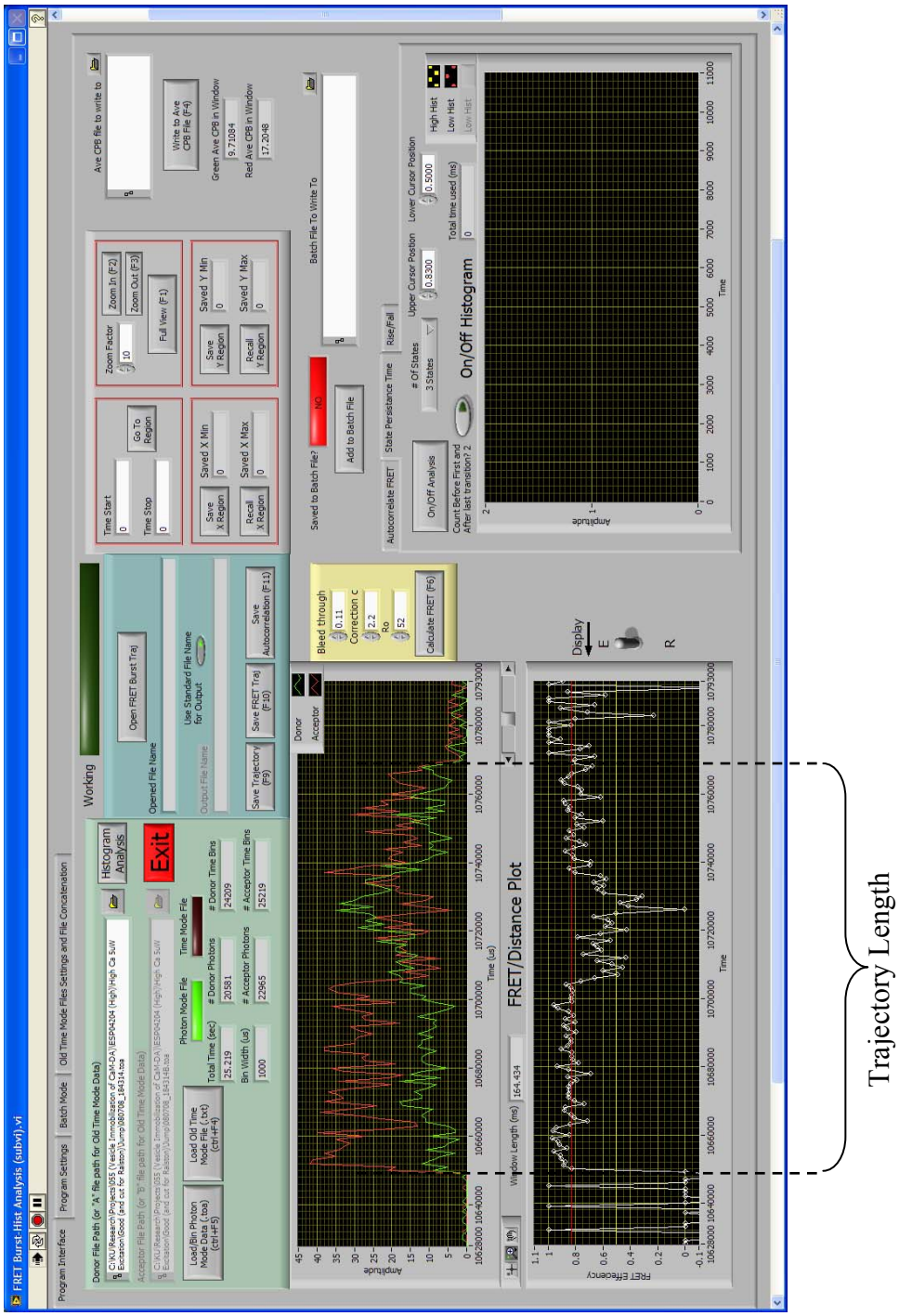

Trajectory Length

Figure 5.4: Example of immobilized molecule trajectory analysis. The green and red lines represent the donor and acceptor signals respectively. The laser on and photobleaching point can be easily seen in the trajectory window. The FRET efficiency used for analysis is limited to the region between 1.065×10^7 μs and 1.077×10^7 μs resulting in a single trajectory lasting 120 ms.

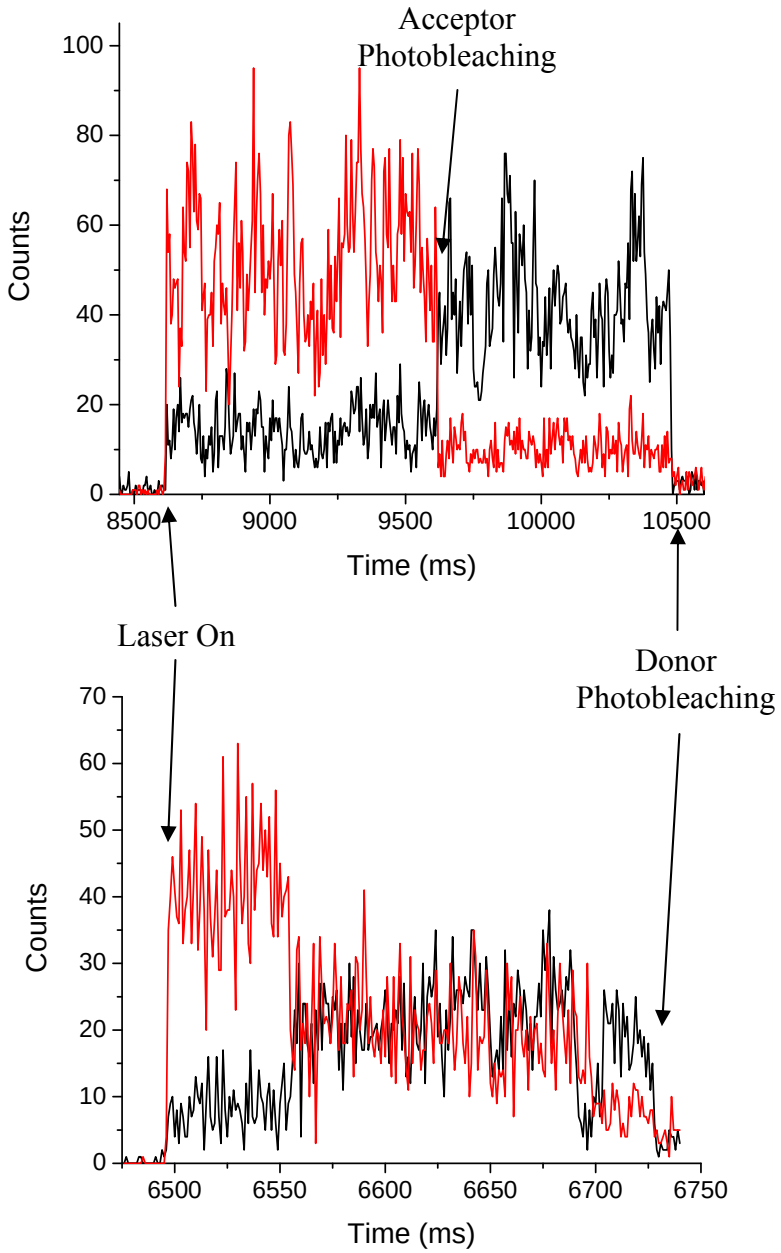

Figure 5.5: Example immobilized molecule trajectories of donor (black line) and acceptor (red line) fluorescence. The laser on time is easily seen and tagged as the start time. Upon acceptor photobleaching there is no longer any FRET information with that molecule.

5.3. System Checks

Due to the requirement of the current system to split the signal for the scanning software there was concern of the presence of reflections due to the T placed just before the PCI-6602 inputs. Reflections could lead to one channel having double the expected counts resulting in incorrect calculated FRET efficiencies. To check for reflections a blank cover slip was placed on the microscope and the signal from the scatter was collected and correlated. This is the same measurement performed for collecting the afterpulse profile used in corrections. Therefore if there are no reflections then the correlations should contain no peaks after correction for afterpulsing. Figure 5.6 shows the results from the correlation demonstrating the absence of reflections in the system.

Before collecting data on immobilized molecules it was crucial to verify that the molecules found in the images were due to specific binding of the vesicles to the biotin-streptavidin linker. Figure 5.7 contains three trials demonstrating first the background counts and then comparing images in the absence and presence of streptavidin. As Figure 5.7 shows the immobilization is very specific when streptavidin is added to the flow-cell. The faint spots seen in Figure 5.7B would not have been identified as molecules for imaging.

5.4. Results

The first analysis method used was to autocorrelate the FRET efficiencies for each trajectory and average the results for all molecules. The autocorrelation function

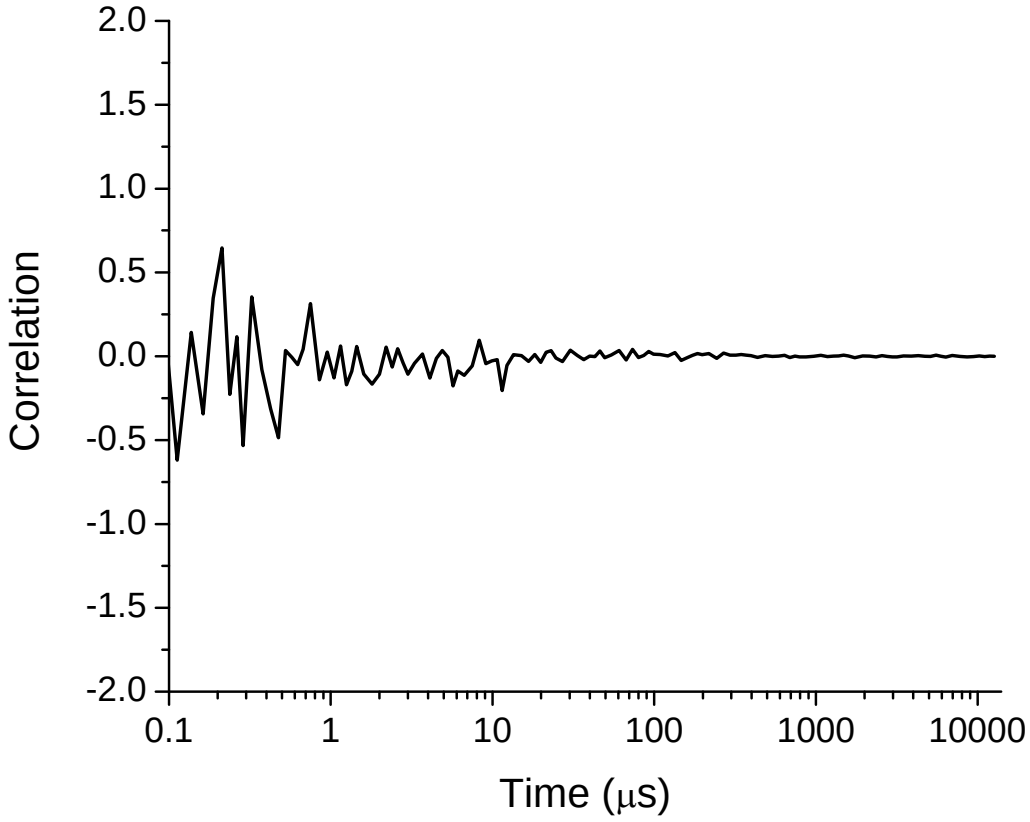

Figure 5.6: Afterpulse corrected correlation of background scatter signal from acceptor APD after T-junction addition for use with PCI card NI-6052 for scanner control. Any reflection(s) would appear as large peak(s) in the correlation.

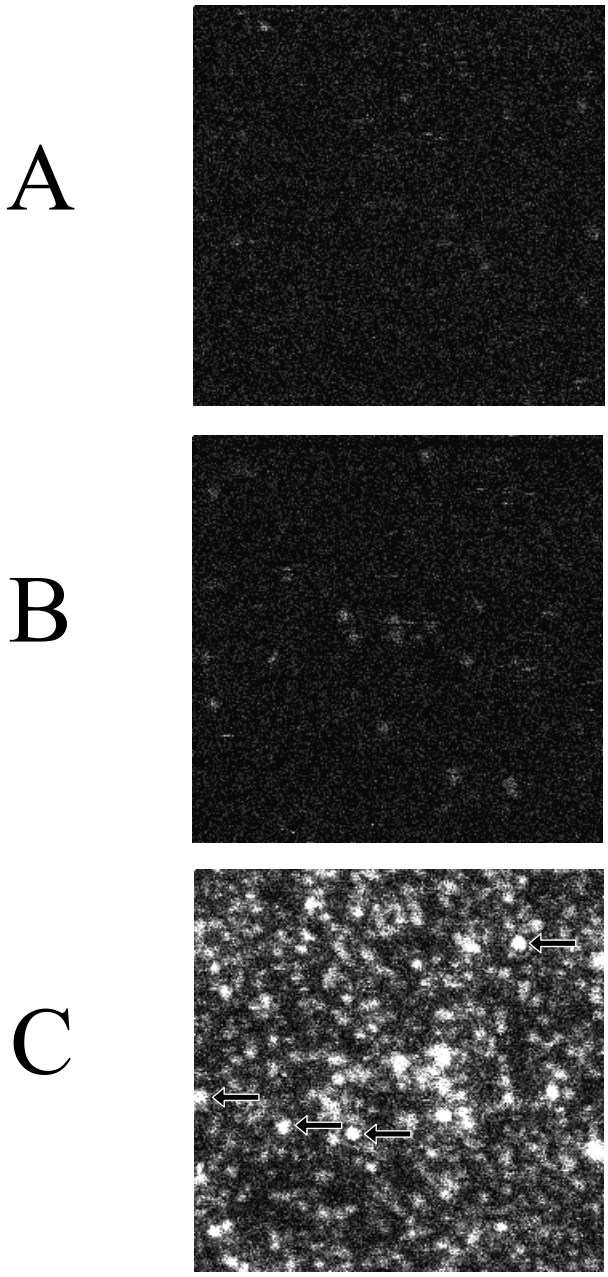

Figure 5.7: Control scans for vesicle immobilization. All scans are 15x15 μm at a scan rate of 1.5 Hz. (A) Lipid bilayer and streptavidin only. (B) Vesicle immobilization in the absence of streptavidin linker. (C) Complete vesicle immobilization procedure with single-molecule examples identified by the arrows.

used is very similar to the time mode autocorrelation discussed previously with one change. In order to better average the correlations between molecules the first point (zero lag time) of the correlations was normalized to one using equation 5.1:

$$\frac{\langle \delta F(t)\delta F(t+\tau)\rangle}{\langle \delta F^2\rangle} = \frac{\langle F(t)\cdot F(t+\tau)\rangle - \langle F(t)\rangle\cdot\langle F(t+\tau)\rangle}{\langle F(t)^2\rangle - \langle F(t)\rangle^2} \tag{5.1}$$

where the left side is a modified form of the autocorrelation given in equation 1.8 and the right side is how the correlation function is calculated programmatically. One advantage to autocorrelating the data is that it is model independent. Any correlated fluctuations in the FRET efficiency will appear in the correlation decay.

To perform the autocorrelation the FRET efficiency was calculated with a bin size of 500 μs and then correlated for each molecule. The length of the correlation for each molecule was set to half the length of the trajectory and the correlations were averaged together. Figure 5.8 shows the resulting correlations for high-Ca^{2+} CaM and apo CaM. The apo CaM correlation fit well to a single exponential of 9.5 ± 2 ms while the high Ca^{2+} CaM required two exponentials with time constants of 1.3 ± 0.8 ms and 18 ± 4 ms with fractions of 0.62 ± 0.11 and 0.38 ± 0.11 respectively. Errors were determined through the use of support plane analysis.

In order to compare the relative amplitudes of dynamics in apo CaM and high Ca^{2+} CaM, unnormalized correlations were calculated by removing the denominator from equation 5.1. Now at $\tau = 0$ the numerator is $\langle \delta F^2\rangle$, which is the total variance of the correlation. The total variance of the correlation is comprised of the variance from the noise plus the variance from the dynamics as shown in equation 5.2.

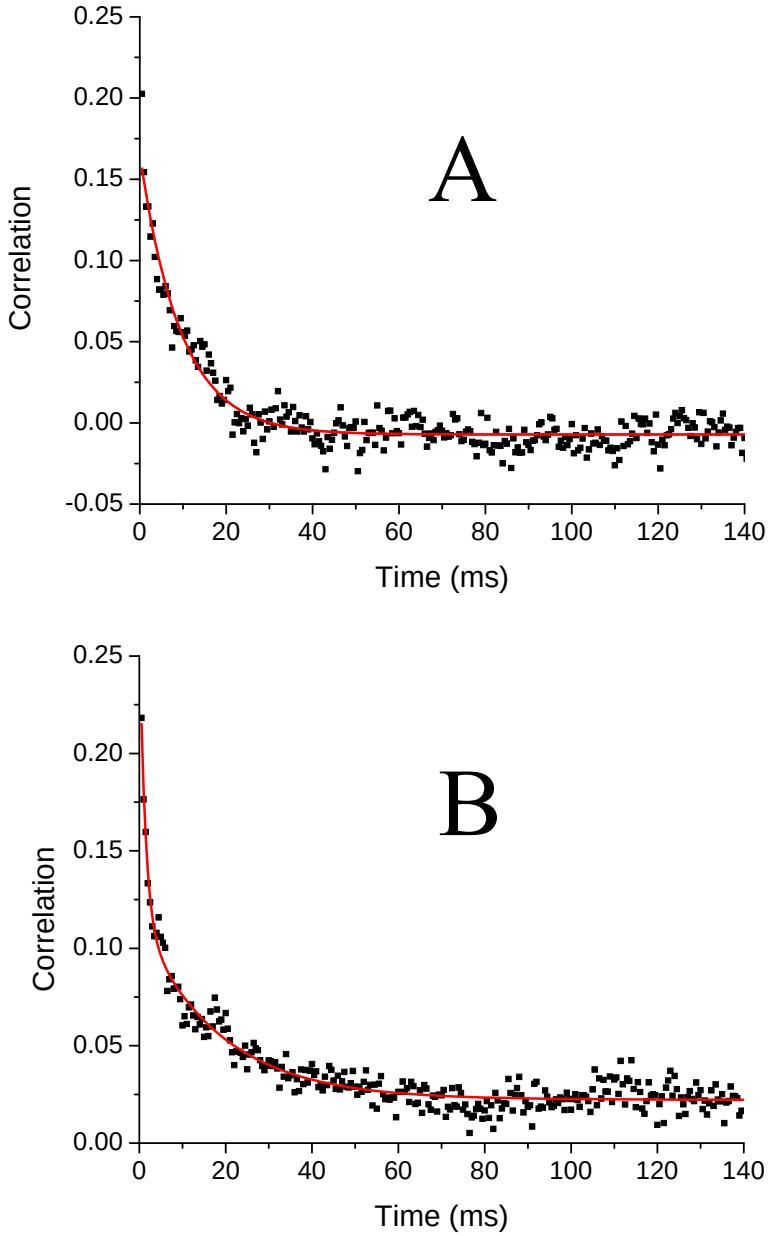

Figure 5.8: Autocorrelation of FRET efficiencies at 500 μs time resolution. (A) Low Ca^{2+} CaM fit to a single exponential with a time constant of 9.5 ± 2 ms. (B) High Ca^{2+} CaM fit to two exponential time constants of 1.3 ± 0.8 ms and 18 ± 4 ms with fractions of 0.62 ± 0.11 and 0.38 ± 0.11 respectively.

$$\left\langle \delta F^2 \right\rangle = \sigma_n^2 + \sigma_d^2 \tag{5.2}$$

Because the variance from noise is uncorrelated, it contributes only to the first point of the correlation ($\tau = 0$). The correlations were fit to a single or double exponential, which by extrapolation to zero give an estimate of σ^2_d for the dynamics. The unnormalized extrapolated initial amplitudes for high Ca^{2+} CaM and apo CaM were 0.0086 and 0.0071 respectively. This result shows that the high Ca^{2+} CaM correlation contains about 20% more dynamics on the timescale spanned by the trajectories, i.e. from 500 μs (the bin width for the autocorrelation) to on the order of 100 ms (a typical trajectory length).

These results demonstrate the presence of both faster conformational dynamics and an increase in the amplitude of dynamics for the Ca^{2+} saturated CaM vs. apo CaM. While the correlations give a good picture of the presence of dynamics at both Ca^{2+} levels, information about what transitions are the source of the dynamics is lost.

In order to learn more about the transitions occurring in the sample the persistence time above and below a preset threshold level was used. In order to perform this analysis the threshold level needed to be decided on, which required some knowledge about the distribution of the FRET states present in the system. The thresholds could then be set between the peaks in the distribution to measure the dynamics of moving from one state to the other. It has been reported previously using CaM 34-110 that there are three states present in the sample with efficiencies centered at 0.94, 0.74, and 0.30.[15] Using this information it was expected that there

would be two threshold settings resulting in the persistence times of three states. In order to determine the appropriate threshold levels for these measurements a two-pronged approach was taken. Firstly, the threshold was swept through a range of FRET efficiencies and each of the resulting persistence state histograms were fit to a two-exponential decay and the rate of state switching was determined. If the threshold was positioned between two states then the rate of interchange would be at a minimum when compared to a threshold value in the middle of a state. Figure 5.9 shows the results from the threshold level study. There are two regions in the plot where the rate drops at threshold levels of about 0.4 and 0.8, which agrees well with the previously measured distributions. The second method of identifying where to set the threshold levels was to measure the fluorescence lifetime distribution of the donor fluorophore (Alexa Fluor 488) in bulk by time-correlated single photon counting. Figure 5.10 shows the maximum entropy fit to the fluorescence lifetime decay. The maximum entropy fit showed four peaks in the lifetime distribution that correspond to FRET efficiencies of 0.98, 0.90, 0.62, and 0.19. In the single-molecule trajectories the 0.98 and 0.90 states would be indistinguishable due to the relatively small numbers measured for the donor and acceptor intensities resulting in three measurable FRET states. As is shown in Figure 5.10 if thresholds are drawn between the lifetime distributions the same two FRET efficiencies are chosen for the threshold settings as with the rate of interchange method.

Conformational exchange timescale (CET) histograms were calculated using the threshold settings decided previously. The histograms were generated by

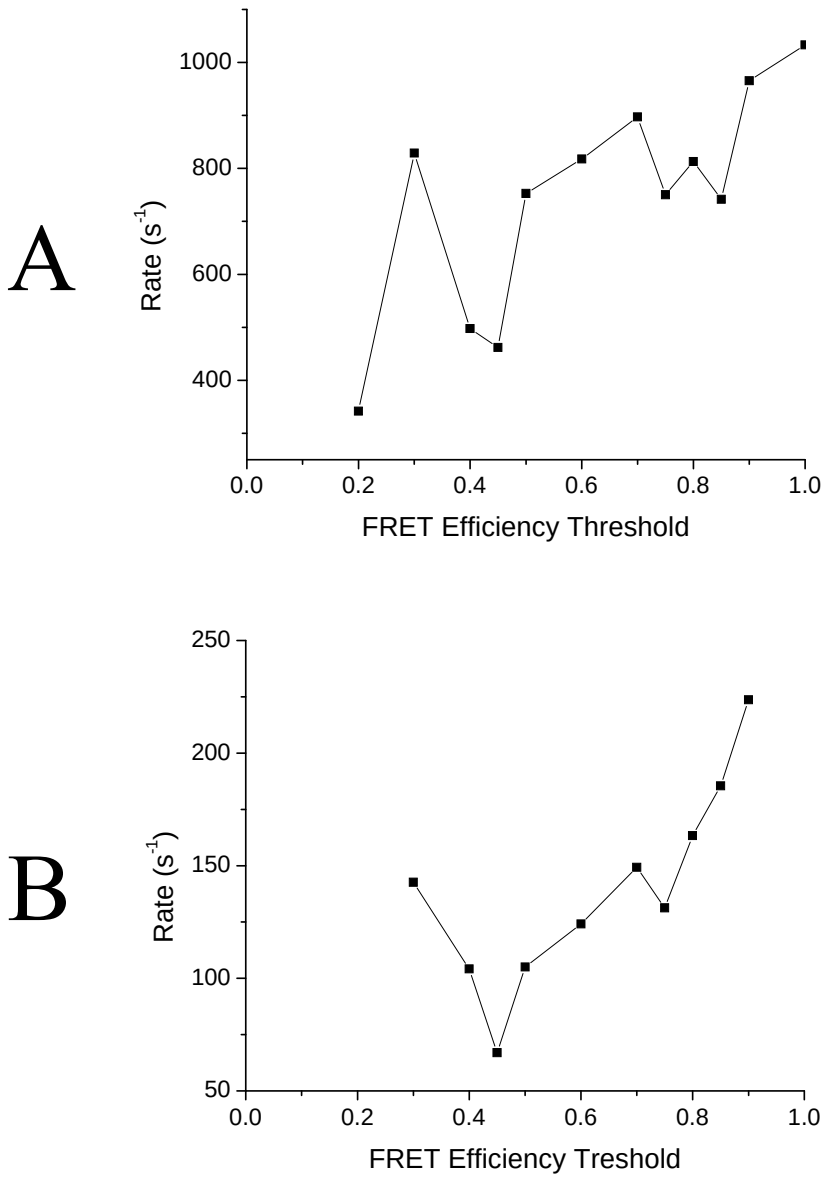

Figure 5.9: Plot of sums of rates for transitions in both directions across the threshold vs. threshold level used. (A) Fast rate constant. (B) Slow rate constant. Note the separation of three states at thresholds of about 0.4 and 0.8 in both A and B.

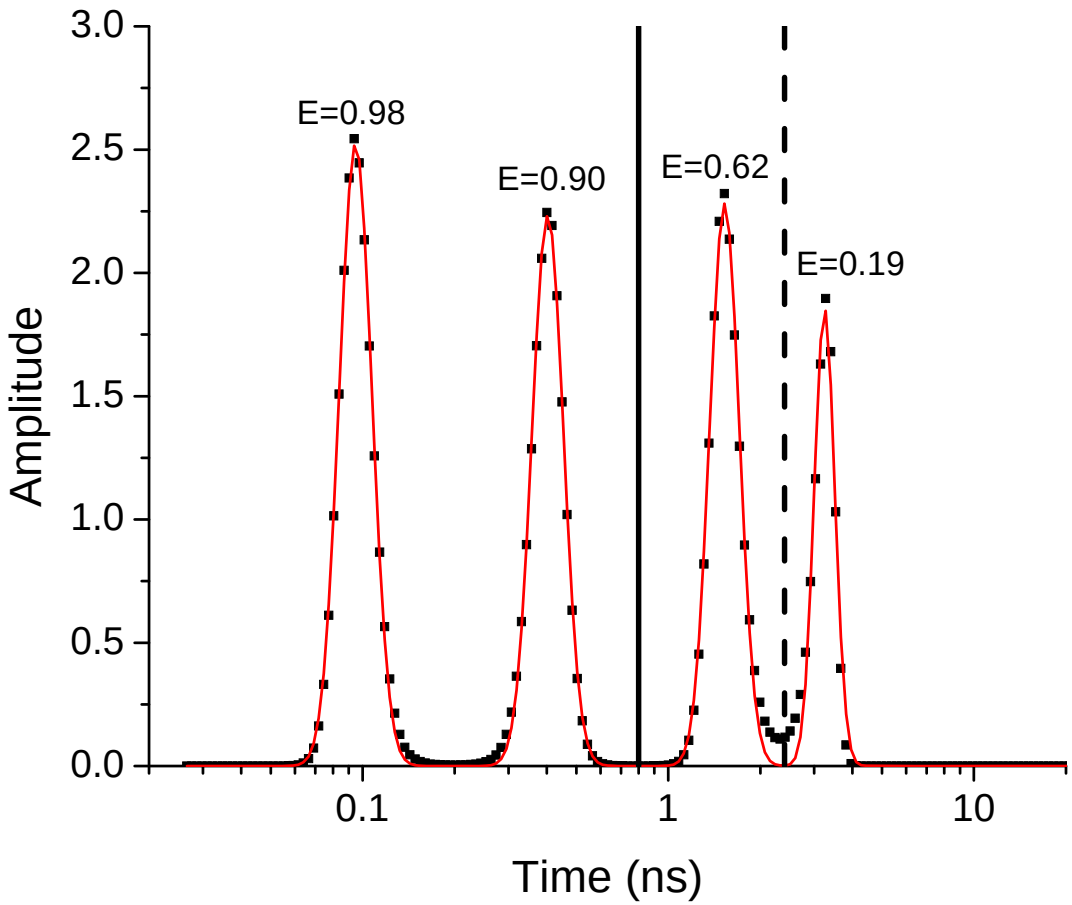

Figure 5.10: Maximum entropy fit for the fluorescence lifetimes of CaM-34-110-AF488-Texas Red in high Ca^{2+} buffer. The corresponding FRET efficiency for each peak is given. The vertical solid (E = 0.8) and dashed (E=0.4) represent the chosen threshold levels.

counting the number of consecutive bins in each state for each trajectory and then histogramming the number of occurrences for each state length. Figure 5.11 contains example FRET efficiency trajectories for four molecules demonstrating the transition from one state to another. The three states have been termed high ($E > 0.8$), mid ($0.4 < E < 0.8$), and low ($E < 0.4$). Three histograms were generated for each buffer condition using 1 ms time bins. Each of the CET histograms were then fit to a single or double exponential decay and the fractional amplitude of each time constant for that state was calculated. The first point in each histogram was not fit due to the large influence of noise causing the FRET efficiency to jump to a different state for only one bin and then return to its previous state. Figure 5.12 shows the results for the histogram fits and Table 5.1 contains the fit parameters for each histogram. The major component for all of the fits is a fast ~1 ms time constant, which could be partly or wholly due to the noise characteristics of the data where the FRET efficiency jumps above or below a threshold level for a few bins as a result of fluctuations due to noise. The fast time constant could also be partly from some unresolved faster timescale fluctuation.

The long time constant, while a smaller fraction of the total decay, showed differences between high Ca^{2+} CaM and apo CaM dynamics consistent with previous studies.[21] The persistence time and amplitude of the mid state is considerably different between the two Ca^{2+} levels. The high Ca^{2+} CaM persistence time is both faster and a larger fraction of the decay signaling a more dynamic system moving to either the high or the low state as it samples the different conformations. The

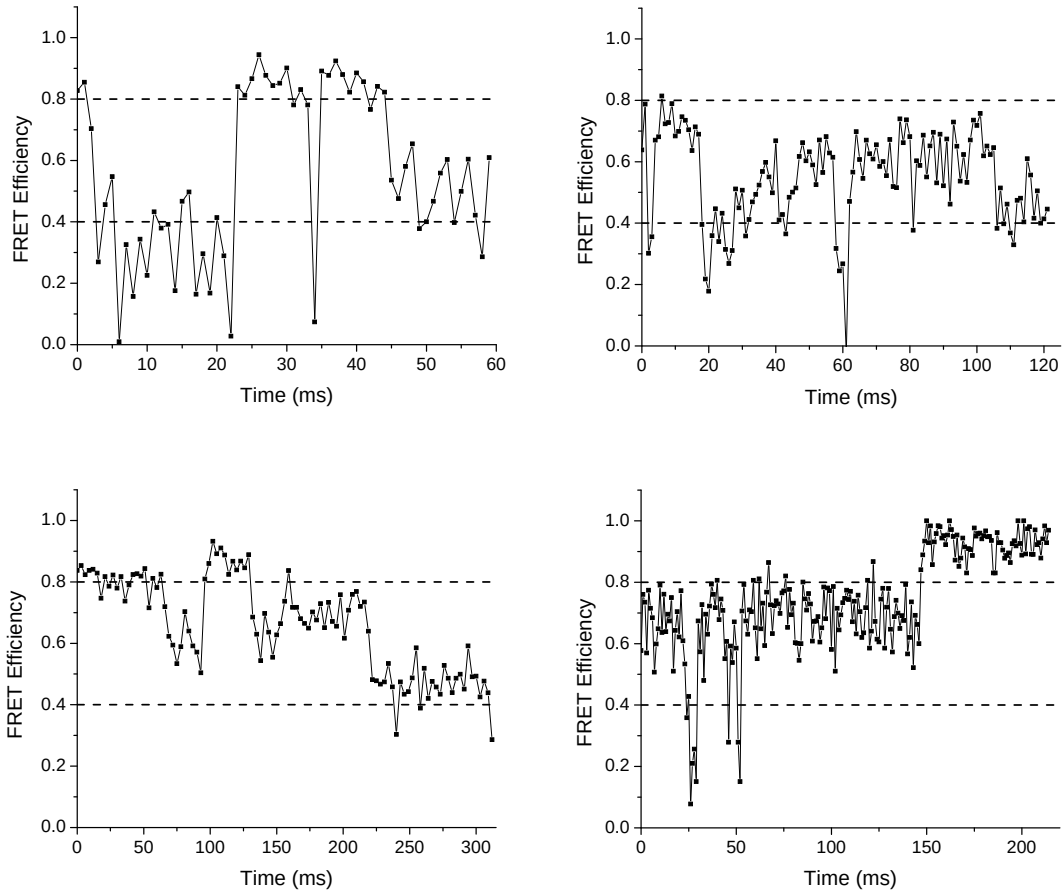

Figure 5.11: Example FRET trajectories for vesicle immobilized CaM. The dashed lines represent the high (>0.8), mid (<0.8 & >0.4), and low (<0.4) state cutoff levels.

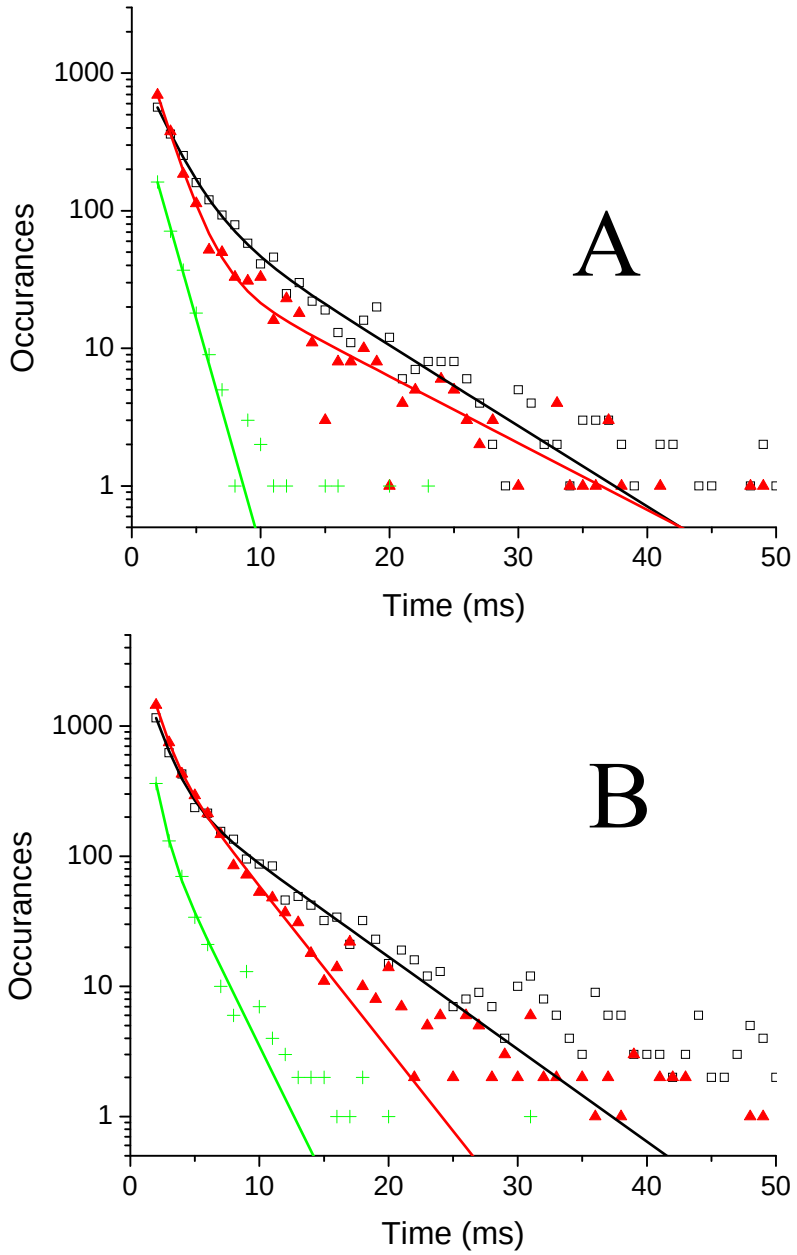

Figure 5.12: CET histogram fits for the three states. (A) apo CaM. (B) High Ca^{2+} CaM. High state data given by open squares (fit black line), mid state given by red triangles (fit red line), and low state given by green plus sign (fit green line).

Table 5.1: CET fitting results for apo and high Ca^{2+} CaM. The total histogram counts for the high, mid, and low states for Apo CaM were 3228, 4073, and 934 respectively. The total histogram counts for the high, mid, and low states for High Ca^{2+} CaM were 6415, 8156, and 2021 respectively.

	Apo CaM		High Ca^{2+} CaM	
	Fast Time Constant			
	Fraction	Time (ms)	Fraction	Time (ms)
High	0.89 ± 0.03	1.9 ± 0.1	0.91 ± 0.02	1.2 ± 0.1
Mid	0.98 ± 0.01	1.41 ± 0.09	0.87 ± 0.03	0.96 ± 0.09
Low	1	1.31 ± 0.05	0.94 ± 0.03	0.61 ± 0.05
	Slow Time Constant			
	Fraction	Time (ms)	Fraction	Time (ms)
High	0.11 ± 0.03	7 ± 1	0.09 ± 0.02	6.1 ± 0.8
Mid	0.02 ± 0.01	9 ± 4	0.13 ± 0.03	3.5 ± 0.5
Low	N/A	N/A	0.06 ± 0.03	2.2 ± 0.4

low-state persistence time for apo CaM did not contain a measureable long time constant while the high Ca^{2+} CaM had a time constant of 2.2 ms. Burst measurements have indicated that the extended conformation is more populated in the apo form than the high Ca^{2+} form.[22] It is possible that the persistence time for apo CaM in the extended conformation (low FRET state) is too long to show up in the trajectories which would be consistent with a higher population of apo CaM in the extended state.

In a three state system such as A ↔ B ↔ C where A is the low FRET state, B is the mid FRET state, and C is the high FRET state there are four rates to be determined. In the CET histogram results shown in Table 5.1 it was not known which direction the mid (B) state transitions were occurring. In order to determine all of the rates the mid state persistence times were split into two histograms, one histogram of persistence times for when the transition out of the mid state goes to the high state and a histogram of persistence times for when the transition out of the mid state goes to the low state. The histograms and fits are shown in Figure 5.13 and the fit values given in Table 5.2.

With this new rate information a picture of the conformational fluctuations of CaM can be constructed. Figure 5.14 shows possible conformations for the three FRET states. This model makes the assumption that there are no transitions that occur between A and C. This assumption is reasonable as only 3% of the transitions that occurred in the high Ca^{2+} CaM or apo CaM trajectories underwent a transition from high to low or low to high. Using the slow time constants from

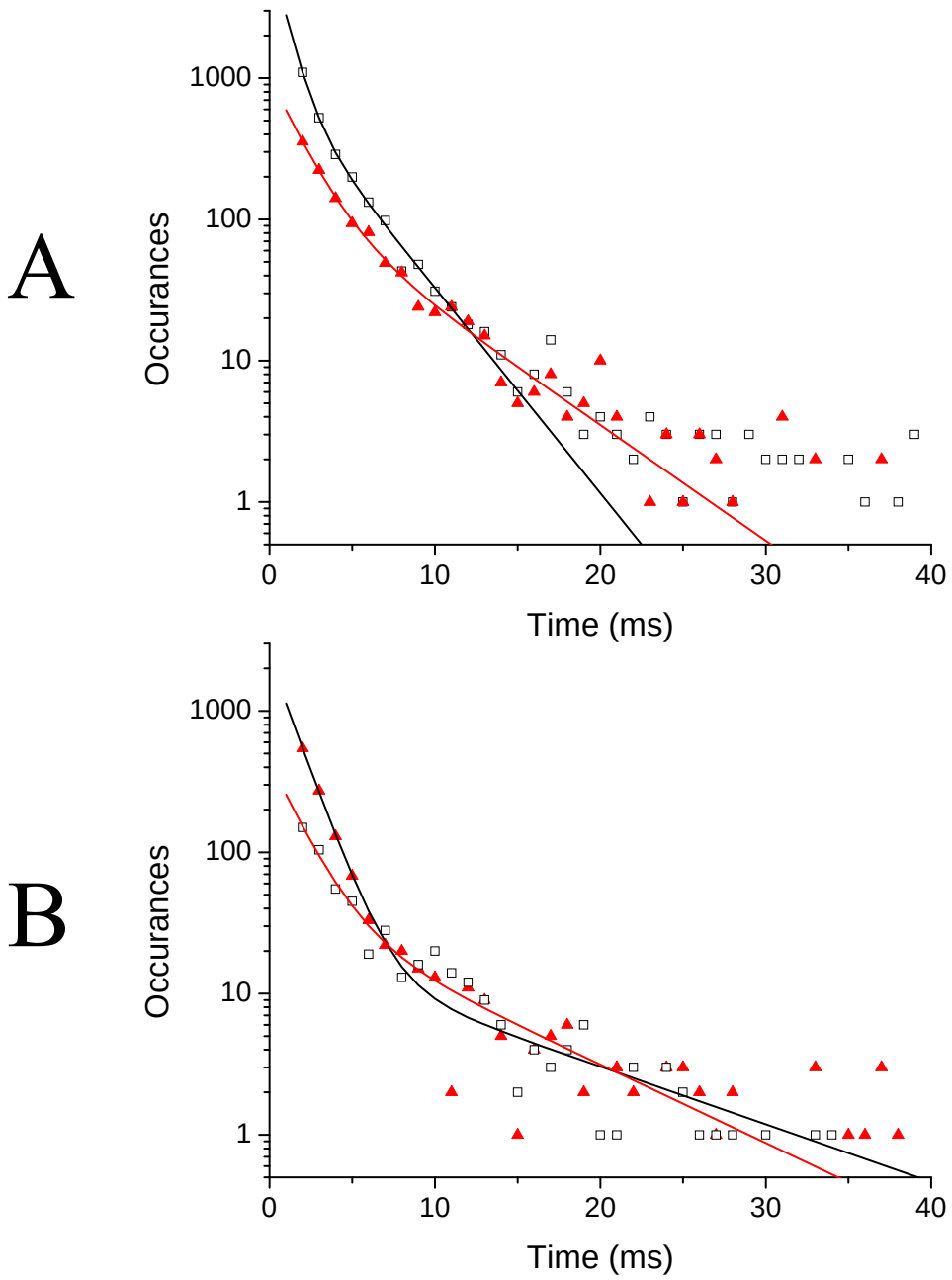

Figure 5.13: Mid state CET histograms for transitioning to high or low states. (A) High Ca^{2+} CaM. (B) apo CaM. The black open squares represent the persistence times when the mid state transitions to the high state and the red triangles represent persistence times when the mid state transitions to the low state.

Table 5.2: Mid state CET times for transitioning to high or low states results. The total histogram counts for high Ca^{2+} CaM mid to high and mid to low were 2615 and 1165. The total histogram counts for apo CaM mid to high and mid to low were 1191 and 528.

	Apo CaM		High Ca^{2+} CaM	
Persistence time of mid state transitioning to high state				
	Fraction	Time (ms)	Fraction	Time (ms)
Fast Tau	0.99 ± 0.01	1.3 ± 0.1	0.89 ± 0.03	0.8 ± 0.1
Slow Tau	0.01 ± 0.01	11 ± 5	0.11 ± 0.03	3.0 ± 0.3

Persistence time of mid state transitioning to low state				
	Fraction	Time (ms)	Fraction	Time (ms)
Fast Tau	0.91 ± 0.08	1.7 ± 0.4	0.85 ± 0.08	1.6 ± 0.3
Slow Tau	0.09 ± 0.08	8 ± 4	0.15 ± 0.08	5 ± 2

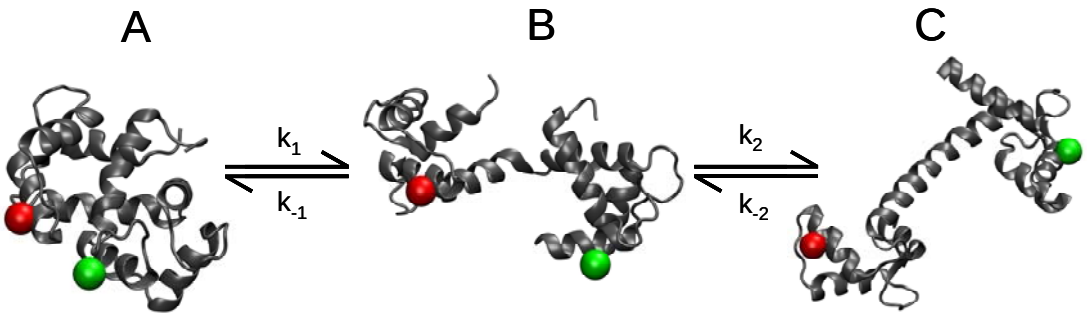

Figure 5.14: Proposed three state system for conformational fluctuations of CaM. Residue 34 represented by green spheres and residue 110 represented by red spheres. State A is represented by pdb 1PRW, State B represented by a modified extended version of 1PRW, and State C represented by pdb 3CLN.

Tables 5.1 and 5.2 the rates of interchange between the states at each Ca^{2+} level were determined with the resulting values shown in Table 5.3. It is interesting that the rate out of the compact state (k_1) is very similar for the high Ca^{2+} CaM and apo CaM but the rate into the compact state is over three times higher for the high Ca^{2+} CaM compared to apo CaM. A common conformation of CaM when bound to a target is a very compact structure.[23] In order for favorable binding interactions to occur, CaM may need to sample those conformations at a higher rate when in its activated (Ca^{2+} loaded) state.

5.5. Conclusion

The work presented in this chapter has demonstrated the ability to immobilize FRET pair labeled calmodulin inside of unilamellar vesicles. Once immobilized, donor/acceptor fluorescence trajectories were collected and the calculated FRET efficiencies were analyzed using several methods. The overall picture of CaM dynamics from this chapter shows that Ca^{2+} saturated CaM generally has a faster rate of interchange between conformations and there is a distinct increase of the rate into the compact conformation when CaM is saturated with Ca^{2+} compared to apo CaM. While apo CaM does show transitions between the FRET efficiency states on the millisecond timescale, the fraction of molecules transitioning is lower than high-Ca^{2+} CaM and the rates of interchange are slower.

A glimpse of the effects of Ca^{2+} on the dynamics of CaM on the microsecond and millisecond timescale has been presented in the last two chapters. Using FCS a

Table 5.3: Rate constants (s^{-1}) for the parameters shown in Figure 5.14 determined from the time constants fit in the persistence time histograms.

Rate	High Ca^{2+} CaM	Apo CaM
k_1 (s^{-1})	160 ± 20	140 ± 20
k_{-1} (s^{-1})	340 ± 40	100 ± 50
k_2 (s^{-1})	200 ± 60	130 ± 70
k_{-2} (s^{-1})	460 ± 80	Not measureable

wobbling motion on the 100 μs timescale in the presence of Ca^{2+} was proposed based on the CaM 34-110 and CaM 17-117 results. For all of the fits for the 34-110 and 17-117 correlations a static FRET component was required to fit the data. The correlations extended out to timescales beyond 10 ms suggesting the corresponding FRET state was static on timescales to at least 10-20 ms. When measuring the dynamics of CaM 34-110 immobilized in vesicles using persistence time analysis, there were a small fraction (~10%) of the molecules that did not show any FRET state transitions for the length of the trajectory. These molecules along with the longer millisecond dynamics measured in the vesicles are likely both contributors to the static FRET states needed in the FCS fits. The CaM 5-44 FCS results showed an increased rigidity of the N-terminal EF-hand loops upon the binding of Ca^{2+} and for apo CaM an increase in the amplitude of the dynamics and the introduction of fast fluctuations on the 2 μs timescale. The vesicle immobilization results have shown an increase in dynamics for the overall protein conformations in the Ca^{2+} saturated state. These faster conformational dynamics might assist CaM in its ability to bind to the wide variety of binding sites and targets that it needs to in order for the cell to function correctly.[24]

In CaM (and many other proteins) there are dynamics occurring on whatever timescale is being measured, whether it be nanosecond fluctuations of the backbone structure of CaM [25,26], microsecond Ca^{2+} binding and unbinding dynamics [21], or longer millisecond dynamics from major conformational changes.[27] All of these timescales are important to aid in a better understanding of protein-target interaction,

and studies like the one discussed in this dissertation help paint a picture of the wide range of dynamics that CaM contains, providing it the biological function that it needs.

5.6. References

1. Allen, M. W., Bieber Urbauer, R. J., and Johnson, C. K., *Single-Molecule Assays of Calmodulin Target Binding Detected with a Calmodulin Energy-Transfer Construct*. Anal. Chem., **2004**. 76(13): p. 3630-3637.

2. Allen, M. W., Urbauer, R. J. B., Zaidi, A., Williams, T. D., Urbauer, J. L., and Johnson, C. K., *Fluorescence Labeling, Purification and Immobilization of a Double Cysteine Mutant Calmodulin Fusion Protein for Single-Molecule Experiments*. Anal. Biochem., **2004**. 325(2): p. 273-284.

3. Dickson, R. M., Cubitt, A. B., Tsien, R. Y., and Moerner, W. E., *On/Off Blinking and Switching Behaviour of Single Molecules of Green Fluorescent Protein*. Nature, **1997**. 388: p. 355-358.

4. Tang, J., Mei, E., Green, C., Kaplan, J., DeGrado, W. F., Smith, A. B., III, and Hochstrasser, R. M., *Probing Structural Dynamics of Individual Calmodulin:Peptide Complexes in Hydrogels by Single-Molecule Confocal Microscopy*. J. Phys. Chem. B, **2004**. 108(40): p. 15910-15918.

5. Kim, H. D., Nienhaus, G. U., Ha, T., Orr, J. W., Williamson, J. R., and Chu, S., *Mg^{2+}-Dependent Conformational Change of RNA Studied by Fluorescence Correlation and FRET on Immobilized Single Molecules*. Proc. Natl. Acad. Sci. U.S.A., **2002**. 99(7): p. 4284-4289.

6. Amirgoulova, E. V., Groll, J., Heyes, C. D., Ameringer, T., Rocker, C., Moller, M., and Nienhaus, G. U., *Biofunctionalized Polymer Surfaces Exhibiting Minimal Interaction Towards Immobilized Proteins*. ChemPhysChem, **2004**. 5(4): p. 552-555.

7. Heyes, C. D., Kobitski, A. Y., Amirgoulova, E. V., and Nienhaus, G. U., *Biocompatible Surfaces for Specific Tethering of Individual Protein Molecules*. J. Phys. Chem. B, **2004**. 108(35): p. 13387-13394.

8. Ha, T., Ting, A. Y., Liang, J., Caldwell, W. B., Deniz, A. A., Chemla, D. S., Schultz, P. G., and Weiss, S., *Single-Molecule Fluorescence Spectroscopy of Enzyme Conformational Dynamics and Cleavage Mechanism*. Proc. Natl. Acad. Sci. U.S.A., **1999**. 96: p. 893-898.

9. Talaga, D. S., Lau, W. L., Roder, H., Tang, J., Jia, Y., DeGrado, W. F., and Hochstrasser, R. M., *Dynamics and Folding of Single Two-Stranded Coiled-Coil Peptides Studied by Fluorescent Energy Transfer Confocal Microscopy*. Proc. Natl. Acad. Sci. U.S.A., **2000**. 97(24): p. 13021-13026.

10. Boukobza, E., Sonnenfeld, A., and Haran, G., *Immobilization in Surface-Tethered Lipid Vesicles as a New Tool for Single Biomolecule Spectroscopy*. J. Phys. Chem. B, **2001**. 105(48): p. 12165-12170.

11. Laitinen, O. H., Hytonen, V. P., Nordlund, H. R., and Kulomaa, M. S., *Genetically Engineered Avidins and Streptavidins*. Cell Mol Life Sci, **2006**. 63(24): p. 2992-3017.

12. Okumus, B., Wilson, T. J., Lilley, D. M. J., and Ha, T., *Vesicle Encapsulation Studies Reveal That Single Molecule Ribozyme Heterogeneities Are Intrinsic*. Biophys. J., **2004**. 87(4): p. 2798-2806.

13. Rhoades, E., Gussakovsky, E., and Haran, G., *Watching Proteins Fold One Molecule at a Time*. Proc. Natl. Acad. Sci. U.S.A., **2003**. 100(6): p. 3197-3202.

14. Brasselet, S., Peterman, E. J. G., Miyawaki, A., and Moerner, W. E., *Single-Molecule Fluorescence Resonant Energy Transfer in Calcium Concentration Dependent Cameleon*. J. Phys. Chem. B, **2000**. 104(15): p. 3676-3682.

15. Slaughter, B. D., Allen, M. W., Unruh, J. R., Urbauer, R. J. B., and Johnson, C. K., *Single-Molecule Resonance Energy Transfer and Fluorescence Correlation Spectroscopy of Calmodulin in Solution.* J. Phys. Chem. B, **2004**. 108(29): p. 10388-10397.

16. Slaughter, B. D., Bieber-Urbauer, R. J., and Johnson, C. K., *Single-Molecule Tracking of Sub-Millisecond Domain Motion in Calmodulin*. J. Phys. Chem. B, **2005**. 109(26): p. 12658-12662.

17. Johnson, J. M., Ha, T., Chu, S., and Boxer, S. G., *Early Steps of Supported Bilayer Formation Probed by Single Vesicle Fluorescence Assays*. Biophys. J., **2002**. 83(6): p. 3371-3379.

18. Colletier, J. P., Chaize, B., Winterhalter, M., and Fournier, D., *Protein Encapsulation in Liposomes: Efficiency Depends on Interactions between Protein and Phospholipid Bilayer*. BMC Biotechnol, **2002**. 2: p. 9.

19. Mayer, L. D., Hope, M. J., and Cullis, P. R., *Vesicles of Variable Sizes Produced by a Rapid Extrusion Procedure*. Biochim. Biophys. Acta, **1986**. 858(1): p. 161-168.

20. Macdonald, R. C., Macdonald, R. I., Menco, B. P. M., Takeshita, K., Subbarao, N. K., and Hu, L. R., *Small-Volume Extrusion Apparatus for Preparation of Large, Unilamellar Vesicles*. Biochim. Biophys. Acta, **1991**. 1061(2): p. 297-303.

21. Evenäs, J., Forsen, S., Malmendal, A., and Akke, M., *Backbone Dynamics and Energetics of a Calmodulin Domain Mutant Exchanging between Closed and Open Conformations*. J. Mol. Biol., **1999**. 289(3): p. 603-617.

22. Slaughter, B. D., Unruh, J. R., Allen, M. W., Urbauer, R. J. B., and Johnson, C. K., *Conformational Substates of Calmodulin Revealed by Single-Pair Fluorescence Resonance Energy Transfer: Influence of Solution Conditions and Oxidative Modification*. Biochemistry, **2005**. 44(10): p. 3694-3707.

23. Vetter, S. W., and Leclerc, E., *Novel Aspects of Calmodulin Target Recognition and Activation*. Eur. J. Biochem., **2003**. 270(3): p. 404-414.

24. Wilson, M. A., and Brunger, A. T., *The 1.0 Å Crystal Structure of Calcium-Bound Calmodulin: An Analysis of Disorder and Implications for Functionally Relevant Plasticity*. J. Mol. Biol., **2000**. 301(5): p. 1237-1256.

25. Chang, S.-L., and Tjandra, N., *Analysis of NMR Relaxation Data of Biomolecules with Slow Domain Motions Using Wobble-in-a-Cone Approximation*. J. Am. Chem. Soc., **2001**. 123(46): p. 11484-11485.

26. Malmendal, A., Evenas, J., Forsen, S., and Akke, M., *Structural Dynamics in the C-Terminal Domain of Calmodulin at Low Calcium Levels*. J. Mol. Biol., **1999**. 293(4): p. 883-899.

27. Ratner, V., Sinev, M., and Haas, E., *Determination of Intramolecular Distance Distribution During Protein Folding on the Millisecond Timescale*. J. Mol. Biol., **2000**. 299(5): p. 1363-1371.